

***A ced-3 caspase – ect-2 RhoGEF axis coordinates functional interactions between the apoptotic pathway and cell size in Caenorhabditis elegans***



Dissertation

Zur Erlangung des Doktorgrades der Naturwissenschaften

(Dr. rer. nat.)

der Fakultät für Biologie

der Ludwig-Maximilians-Universität München

vorgelegt von

**Aditya Rajiv Sethi**

aus **Mumbai, India**

**München, April 2023**

**1. First Reviewer:** Prof. Dr. Barbara Conradt  
**2. Second Reviewer:** Prof. Dr. Wolfgang Enard  
**Date of Submission:** 25<sup>th</sup> April 2023  
**Date of Defense:** 20<sup>th</sup> July 2023

---

## **Eidesstattliche Erklärung**

Ich versichere hiermit an Eides statt, dass die vorgelegte Dissertation von mir selbständig und ohne unerlaubte Hilfe angefertigt ist.

I declare that I have authored this thesis independently and that I have not used other than the declared sources.

München, 25th April 2023

Aditya Rajiv Sethi

## **Erklärung**

Hiermit erkläre ich, dass ich zuvor nicht versucht habe, anderweitig eine Dissertation einzureichen oder mich einer Doktorprüfung zu unterziehen. Die vorliegende Dissertation wurde keiner weiteren Prüfungskommission weder in Teilen noch als Ganzes vorgelegt.

I declare that I have not submitted or defended a dissertation previously without success. The present dissertation has not been presented to another examination board, neither entirely nor in parts.

München, 25th April 2023

Aditya Rajiv Sethi

# ABSTRACT

Programmed cell death via apoptosis is a common cell fate during animal development and its mis-regulation can have serious implications in diseases and disorders. Therefore, it is of high importance to study to apoptosis. The highly conserved central apoptotic pathway was initially discovered in *C. elegans* and consists of four genes acting in a sequence – *egl-1* BH3-only, *ced-9* Bcl-2, *ced-4* Apaf-1 and *ced-3* caspase. The most downstream gene in the pathway, *ced-3*, encodes for a cysteine protease called caspase, and is essential in the execution of apoptosis. A previous study in our lab had uncovered a novel non-apoptotic role of *ced-3* caspase in promoting asymmetric division of *C. elegans* neuroblasts (Mishra et al., 2018). However, the mechanism by which *ced-3* caspase promotes asymmetric division still remained to be elucidated. Thus, in my study, I aimed to decipher the mechanism(s) by which the apoptotic gene, *ced-3* caspase, promotes asymmetric cell division.

To that end, I first demonstrated that CED-3 caspase protein physically and directly interacts with a regulator of actomyosin contractility, called ECT-2 RhoGEF (Rho guanine-nucleotide exchange factor). Furthermore, using the NSM (neurosecretory motor neuron) lineage in *C. elegans*, I found that ECT-2 RhoGEF is asymmetrically enriched in the NSM neuroblast, which is the mother of the apoptotic cell. I also found that the asymmetric enrichment of ECT-2 RhoGEF depends on *ced-3* caspase activity. Next, by analysing the cell size ratios of the daughters of the NSM neuroblast, my colleagues and I found that genetically, *ced-3* caspase acts upstream of *ect-2* RhoGEF to promote the asymmetric division by size of the NSM neuroblast. We refer to this as the *ced-3-ect-2* axis.

Based on these findings, we propose that the *ced-3-ect-2* axis promotes polar actomyosin contractility in the NSM neuroblast, which results in its asymmetric division by size and thereby the formation of its smaller apoptotic daughter cell called the NSMsc (NSM sister cell). Molecularly, we propose that CED-3 de-recruits ECT-2 from the dorsal cortex of the NSM neuroblast before metaphase, and that this de-recruitment of ECT-2 is important for the NSM neuroblast to divide asymmetrically.

Next, my colleagues and I investigated the effect of the size of the smaller daughter cell, the NSMsc, on its apoptotic fate. We found that increasing the size of the NSMsc by reducing *ect-2* activity decreases its probability to undergo apoptosis. Conversely, for the first time, we showed that decreasing the size of the NSMsc by hyperactivation of *ect-2* can increase its probability to undergo apoptosis. Thus, we propose that cell size and apoptosis are inversely correlated – larger cells are more prone to survive and smaller cells are more prone to die.

Taken together, the findings from this study have found reciprocal interactions between the apoptotic pathway and cell size. In the NSM neuroblast, the apoptotic pathway acts upstream of cell size i.e. *ced-3* promotes asymmetric division of the NSM neuroblast and the formation of a smaller NSMsc. Conversely, in the NSMsc, cell size acts upstream of the apoptotic pathway i.e. the small size of the NSMsc promotes the activation/activity of CED-3 and thereby its apoptosis.

## List of common abbreviations

---

*Caenorhabditis elegans*: *C. elegans*

NSM: Neurosecretory motor neuron

NSMnb: NSM neuroblast

NSMsc: NSM sister cell

*ced-3*: Cell death abnormality gene

*ect-2*: Epithelial cell transforming factor 2 gene

*pig-1*: par-1-like gene

*nmy-2*: Non-muscle myosin 2 gene

*ced-9*: Cell death abnormality gene

*ced-4*: Cell death abnormality gene

*egl-1*: Egg-laying defective gene

GEF: Guanine-nucleotide exchange factor

GST: Glutathione-S-transferase

PH: Plekstrin homology

# INDEX



|   |    |
|---|----|
| Abstract  | 4  |
| List of common abbreviations  | 7  |
| <b>1. INTRODUCTION</b>  | 13 |
| <b>1.1 Programmed cell death</b>  | 14 |
| 1.1.1 Programmed cell death via apoptosis   | 14 |
| 1.1.2 The central apoptotic pathway in <i>C. elegans</i>  | 16 |
| 1.1.3 Biochemical and structural pathway of apoptosis in <i>C. elegans</i>                      | 19 |
| 1.1.4 <i>ced-3</i> caspase as an executioner of apoptosis                                       | 22 |
| <b>1.2 The actomyosin network in non-muscle cells</b>   | 23 |
| 1.2.1 Regulators of the actomyosin network and contractility                                    | 26 |
| <b>1.3 Asymmetric cell division</b>   | 29 |
| 1.3.1 Asymmetric cell division during <i>C. elegans</i> development                             | 29 |
| 1.3.2 The role of the actomyosin network in asymmetric cell division by size                    | 34 |
| <b>1.4 The NSM lineage in <i>C. elegans</i> to study apoptosis and asymmetric cell division</b> | 37 |
| 1.4.1 Mechanisms that ensure the apoptotic death of the NSMsc                                   | 38 |
| 1.4.2 Factors promoting asymmetric division by size of the NSMnb                                | 41 |
| 1.4.3 Visualizing the NSM lineage <i>in vivo</i>  | 42 |
| <b>1.5 Background and aim of the study</b>  | 45 |
| <b>2. METHODOLOGY</b>   | 48 |
| <b>2.1 Strains and general maintenance of <i>C. elegans</i></b>                                 | 49 |
| <b>2.2 Plasmid construction</b>   | 51 |
| <b>2.3 Expression of recombinant proteins</b>   | 56 |
| 2.3.1 Expression of recombinant GST-tagged proteins for the pull-down assay                     | 56 |
| 2.3.2 Expression of recombinant FLAG-tagged proteins for the cleavage assay                     | 56 |

|             |  |    |
|-------------|--|----|
| 2.3.3       | Expression of recombinant S-tagged proteins for the pull-down and cleavage assays  | 56 |
| <b>2.4</b>  | <b>GST pull-down assay</b>   | 57 |
| 2.4.1       | Purification of recombinant GST-tagged proteins  | 57 |
| 2.4.2       | The pull-down assay  | 57 |
| <b>2.5</b>  | <b>Cleavage assay</b>  | 59 |
| <b>2.6</b>  | <b>Analysis of GST pull-down and cleavage assay</b>  | 60 |
| <b>2.7</b>  | <b>Calculating NSMsc survival percentage</b>   | 61 |
| <b>2.8</b>  | <b>Confocal and super-resolution microscopy</b>  | 62 |
| <b>2.9</b>  | <b>Determining daughter cell size ratio (NSMsc:NSM)</b>  | 63 |
| 2.9.1       | Mounting embryos and selection the NSM neuroblast  | 63 |
| 2.9.2       | Calculating the NSMsc:NSM daughter cell size ratio   | 63 |
| <b>2.10</b> | <b>Visualization and quantification of ECT-2::GFP, NMY-2::GFP, LifeAct::GFP, CED-3::GFP and mCherry::PH<sup>PLCA</sup> in the NSM neuroblast</b> | 65 |
| 2.10.1      | Visualization of the transgenes using confocal microscopy  | 65 |
| 2.10.2      | Quantification of fluorescence signal to obtain a 'ventral:dorsal fluorescence ratio'  | 66 |
| 2.10.3      | Investigating dynamics of ECT-2::GFP using super-resolution microscopy   | 66 |
| <b>2.11</b> | <b>Calculating metaphase circularity</b>   | 67 |
| <b>2.12</b> | <b>Statistical analyses</b>  | 68 |
| <b>3.</b>   | <b><u>RESULTS</u></b>  | 69 |
| <b>3.1</b>  | <b>CED-3 caspase physically and directly interacts with ECT-2 RhoGEF <i>in vitro</i></b>   | 71 |
| 3.1.1       | A next-generation Yeast two-hybrid screen identified the candidate physical interactors of CED-3   | 71 |

|            |   |            |
|------------|---|------------|
| 3.1.2      | Gene set enrichment analysis of physical interactors of CED-3 gives a hint into how it could promote a smaller daughter cell size | 72         |
| 3.1.3      | CED-3 physically interacts with ECT-2 <i>in vitro</i>   | 74         |
| 3.1.4      | The Plekstrin Homology (PH) domain of ECT-2 is sufficient for its interaction with CED-3  | 77         |
| 3.1.5      | CED-3 does not cleave ECT-2 <i>in vitro</i>   | 79         |
| <b>3.2</b> | <b>A <i>ced-3</i> caspase – <i>ect-2</i> RhoGEF axis promotes asymmetric division of the NSM neuroblast</b>                       | <b>82</b>  |
| 3.2.1      | ECT-2 is ventrally enriched in the NSM neuroblast ~5 minutes before metaphase   | 82         |
| 3.2.2      | Ventral enrichment of ECT-2 in the NSM neuroblast depends on <i>ced-3</i> and its caspase activity                                | 85         |
| 3.2.3      | Asymmetric enrichment of NMY-2 and F-actin in the NSM neuroblast is not <i>ced-3</i> -dependent                                   | 87         |
| 3.2.4      | Total CED-3 protein is uniformly distributed in the NSM neuroblast  | 90         |
| 3.2.5      | <i>ect-2</i> promotes a smaller NSM sister cell size  | 92         |
| 3.2.6      | <i>ced-3</i> might act upstream of <i>ect-2</i> to promote a smaller NSM sister cell size   | 95         |
| 3.2.7      | The <i>ced-3-ect-2</i> axis acts in parallel with the <i>pig-1-nmy-2</i> axis to promote a smaller daughter cell size             | 98         |
| 3.2.8      | <i>nop-1</i> does not act with <i>ect-2</i> to promote a smaller NSM sister cell size   | 100        |
| <b>3.3</b> | <b>A smaller cell size promotes apoptosis</b>   | <b>102</b> |
| 3.3.1      | Larger NSMsc are more prone to survive  | 102        |
| 3.3.2      | Smaller NSMsc are more prone to die   | 104        |
| 3.3.3      | Size-dependent death of the NSMsc depends on the apoptotic pathway  | 105        |
| <b>3.4</b> | <b>Other experiments performed to investigate the <i>ced-3-ect-2</i> axis</b>   | <b>107</b> |
| 3.4.1      | The <i>ced-3-ect-2</i> axis promotes mitotic rounding of the NSM neuroblast   | 107        |

|            |  |     |
|------------|--|-----|
| <b>4.</b>  | <b><u>DISCUSSION</u></b>   | 110 |
| <b>4.1</b> | <b>Reciprocal interactions between the apoptotic pathway and cell size are coordinated by the <i>ced-3-ect-2</i> axis</b>                          | 111 |
| 4.1.1      | CED-3 caspase mediates the clearance of ECT-2 RhoGEF from the dorsal cortex of the NSM neuroblast  | 111 |
| 4.1.2      | The <i>ced-3-ect-2</i> axis acts in parallel with the <i>pig-1-nmy-2</i> axis to promote the formation of a smaller NSMsc below a lethal threshold | 114 |
| 4.1.3      | The small size of the NSMsc promotes its apoptotic death via activation and/or activity of CED-3 caspase   | 118 |
| <b>4.2</b> | <b>Actomyosin-associated substrates of caspases during apoptosis</b>   | 121 |
| <b>4.3</b> | <b>Non-apoptotic roles of caspases</b>   | 122 |
| 4.3.1      | Non-apoptotic roles of the <i>C. elegans ced-3</i> caspase   | 122 |
| 4.3.2      | Non-apoptotic role of caspases in regulation of the cytoskeletal dynamics  | 123 |
| <b>4.4</b> | <b>A small cell size can trigger apoptosis</b>   | 125 |
| <b>4.5</b> | <b>Future directions of the project</b>  | 127 |
| 4.5.1      | Molecular mechanisms that promote the apoptotic death of small cells   | 127 |
| 4.5.2      | RNAi screen to identify genes other than <i>ect-2</i> , which act with <i>ced-3</i> caspase to promote a smaller NSMsc size                        | 128 |
| 4.5.3      | Establishing a NSM lineage specific reporter in developing embryos   | 130 |
| <b>4.6</b> | <b>Concluding remarks</b>  | 133 |
|            | <b>References</b>  | 135 |
|            | <b>Acknowledgements</b>  | 148 |
|            | <b>Curriculum Vitae</b>  | 150 |
|            | <b>List of Publications</b>  | 152 |

**1**

# **INTRODUCTION**

## 1.1 Programmed cell death

---

The adult human body contains about 30 trillion cells – a large proportion of which are being continuously eliminated and at the same time new cells are being generated throughout our lifetime. A fine balance between cell elimination and cell generation is essential to maintain cellular and tissue homeostasis (DeLong, 1998). In fact, the elimination of cells is as crucial a process as cell generation. Failure to eliminate cells can lead to severe consequences such as tumorigenesis and autoimmune diseases (Fuchs & Steller, 2011). Therefore, cell elimination is a tightly regulated process and this controlled process of cell elimination is called programmed cell death. Programmed cell death is a common cell fate during animal development and is subject to multiple levels of regulation to ensure that only the appropriate cells undergo death. There are various types of programmed cell death such as apoptosis, pyroptosis and necroptosis, of which apoptosis will be the focus of this study (Bertheloot et al., 2021).

### 1.1.1 Programmed cell death via apoptosis

Apoptosis has, arguably, been the major focus of scientific research among the different types of programmed cell death. The term apoptosis, which means “falling off” in Greek, was first introduced in 1972 to describe dying cells that showed a characteristic morphology (Kerr et al., 1972). The morphological changes that occur in cells undergoing apoptosis proceeds in two distinct steps: breakdown of the cell to form apoptotic bodies and then its subsequent phagocytosis by neighboring cells (Figure 1.1) (Kerr et al., 1972). The breakdown of the cell begins with the shrinkage of the cytoplasm and the reduction of cell size, followed by chromatin condensation and subsequent plasma membrane blebbing to form apoptotic bodies (Elmore, 2007; Taylor et al., 2008). The apoptotic bodies are then phagocytosed by surrounding cells

and degraded in phagolysosomes. The process of apoptosis, by itself, is non-inflammatory and there is no damage to surrounding tissues. In fact, apoptosis is a highly regulated process and there are multiple mechanisms in place that ensure that only the appropriate cells undergo apoptosis.

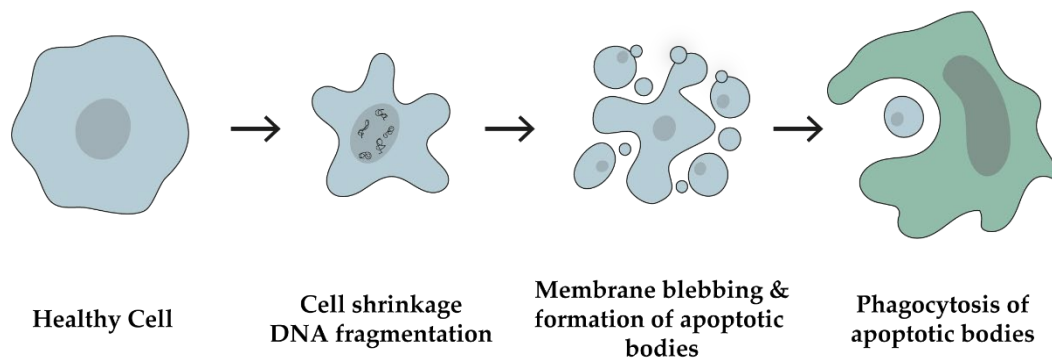


**Figure 1.1 Morphological changes in cells undergoing apoptosis.** When apoptosis is triggered in healthy cells, the cell reduces in size and the DNA undergoes fragmentation. This is followed by membrane blebbing and formation of apoptotic bodies. The apoptotic bodies are finally engulfed via phagocytosis and degraded. Adapted from (Kerr et al., 1972).

Genetically, apoptosis proceeds in three stages – the activation phase, the killing phase and the execution phase (Conradt et al., 2016). The activation phase involves the triggering of the cell to undergo apoptosis. The trigger can either be via intrinsic cues such as DNA damage or via extrinsic signals such as tumor necrosis factor (TNF) or the Fas ligand (Fuchs & Steller, 2015). Both the intrinsic and extrinsic activation pathways subsequently converge to the killing phase, which involves activation of a conserved core killing machinery that leads to the formation of the apoptosome. The execution phase begins with the apoptosome-mediated activation of proteases called caspases that cleave a range of target proteins, which ultimately leads to the characteristic morphological changes observed in apoptotic cells and their subsequent engulfment (Conradt et al., 2016). Although the activation phase of apoptosis has evolved differently in different organisms, the killing phase occurs via a central apoptotic pathway that is highly conserved from *Caenorhabditis elegans* (*C. elegans*) to

humans. In fact, the central apoptotic pathway was first discovered in *C. elegans*, which will be described below.

### **1.1.2 The central apoptotic pathway in *C. elegans***

*C. elegans* is an excellent model organism for developmental biologists because of its essentially invariant cell lineage (Sulston & Horvitz, 1977; Sulston et al., 1983). An invariant cell lineage means that the cell division and migration pattern among individuals remains exactly the same. Furthermore, *C. elegans* is transparent, which enables researchers to view individual cells and their division using differential interference contrast (DIC) microscopy (also called Nomarski Optics) (Figure 1.2, A, B) (Allen et al., 1969; Sulston et al., 1983). These features of *C. elegans* biology enabled John Sulston, H. Robert Horvitz and colleagues to map its entire cell lineage from a single-celled zygote to an adult. They established that during the course of *C. elegans* development, exactly 1090 cells are generated, however, adults contained only 959 somatic nuclei (Sulston & Horvitz, 1977; Sulston et al., 1983). This was because exactly 131 somatic cells were reproducibly eliminated – 113 cells die during embryonic development and 18 somatic cells die during larval development (Sulston & Horvitz, 1977; Sulston et al., 1983). Owing to the invariant lineage, the identities of the 131 dying cells was also determined. Additionally, dying cells could be easily identified using DIC microscopy as they appear more refractile than surrounding cells (Figure 1.2, B) (Roberston & Thomson, 1982). Thus, researchers used *C. elegans* to their advantage to decipher the central apoptotic pathway. The discovery of the central apoptotic pathway was led by a series of seminal genetic studies pioneered by Sydney Brenner, John Sulston and H. Robert Horvitz, which also led them to being awarded the Nobel Prize for Medicine in 2002 for establishing the *C. elegans* cell lineage and discovering the central apoptotic pathway.



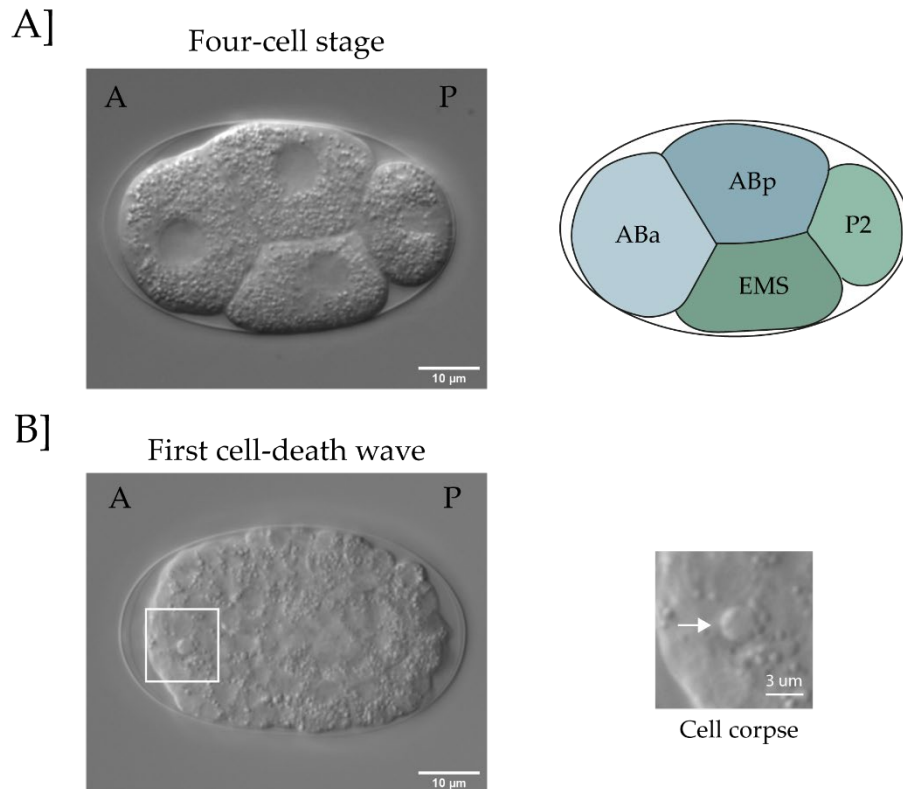


**Figure 1.2 DIC images of *C. elegans* embryos.** A] A DIC image of the four-cell stage embryo. For each of the four cells, the nucleus and the cell body can be seen. The four cells – ABa, ABp, EMS and P2 are labelled. B] A DIC image of the embryo during the first cell-death wave. In the white box, a cell corpse can be identified, which is magnified in the right. A is the anterior side of the embryo and P is the posterior side of the embryo.

Since the identity of the 131 cells programmed to die was known, researchers could study mutations that would lead to either survival of cells that were supposed to die, or death of cells that were supposed to survive. A forward genetics screen approach was used to identify the various genes involved in apoptotic cell death. *ced-1* (cell death abnormal) and *ced-2* were among the first genes to be identified (Hedgecock et al., 1983) – Mutations in these genes blocked the engulfment of apoptotic corpses by neighboring cells leading to the accumulation of cell corpses, which could be easily identified using DIC microscopy. This enabled Ellis H. and colleagues to perform a forward genetic screen in *ced-1* mutant animals. Using this strategy, the first gene to be identified in the central apoptotic pathway was *ced-3* (Ellis & Horvitz, 1986). Ellis H. and colleagues noticed that animals homozygous for complete loss-of-function

mutations of *ced-3* did not accumulate any corpses in a *ced-1* background (Ellis & Horvitz, 1986). This implied that *ced-3* was essential for cell death to occur and therefore was a pro-apoptotic gene. We now know that *ced-3* is the most downstream gene in the central apoptotic pathway (Figure 1.3).

At the same time that *ced-3* was identified, H. Robert Horvitz and colleagues had isolated a mutant defective in egg-laying, called the Egl phenotype (the gene was thus called *egl-1*), where the two hermaphrodite-specific neurons (HSN) responsible for egg-laying were absent (Trent et al., 1983). A loss-of-function mutation of *ced-3* suppressed the Egl phenotype indicating that the HSN neurons were inappropriately undergoing cell death in *egl-1* mutants (Ellis & Horvitz, 1986). This provided a unique opportunity for researchers to identify pro-apoptotic genes similar to *ced-3* by screening for mutations that suppress the Egl phenotype. Using this strategy, another pro-apoptotic gene, *ced-4* was identified. Loss-of-function mutations of *ced-4* did not only block the death of the HSN neurons in *egl-1* animals, but also blocked all apoptotic cell deaths indicating its central role in promoting apoptosis (Ellis & Horvitz, 1986). Additionally, *ced-4* was placed upstream of *ced-3* as it was shown that ectopic cell death caused by overexpression of *ced-4* required *ced-3* activity (Shaham & Horvitz, 1996). The last pro-apoptotic gene in the pathway was identified by Conradt B. and colleagues in a screen for mutants that suppress the *egl-1* Egl phenotype (Conradt & Horvitz, 1998). The inappropriate death of the HSN neurons in *egl-1* mutants was shown to be due to a gain-of-function mutation of *egl-1* (Conradt & Horvitz, 1998; Trent et al., 1983). By screening for mutants that suppressed the Egl phenotype, it was found that a loss-of-function mutation of *egl-1* could suppress the Egl phenotype. Similar to *ced-4*, the loss-of-function mutation of *egl-1* did not only block the death of the HSN neurons, but also blocked all apoptotic cell deaths indicating its central role in promoting apoptosis (Conradt & Horvitz, 1998).

The only anti-apoptotic gene in the pathway, *ced-9*, was identified by studying another neuronal lineage called the neurosecretory motor neuron (NSM) lineage. The mother

of the NSM neuron divides asymmetrically to form a smaller daughter, called the NSM sister cell (NSMsc) and the larger daughter, called the NSM neuron. The NSMsc undergoes apoptotic cell death approximately 20 minutes after being generated and the NSM differentiates to form a serotonergic neuron (Sulston et al., 1983). Hengartner M. and colleagues screened for animals that showed inappropriate survival of the NSMsc and found that a gain-of-function mutation of the gene *ced-9* led to the inappropriate survival of not only the NSMsc, but also of all cells programmed to die via apoptosis (Hengartner et al., 1992). In contrast, loss-of-function of *ced-9* led the inappropriate death of cells causing embryonic lethality indicating its role in inhibiting apoptosis in cells not programmed to die (Hengartner et al., 1992). Furthermore, the embryonic lethality of *ced-9* loss-of-function mutants could be suppressed by the loss of *ced-4* and *ced-3*, but not *egl-1* (Hengartner et al., 1992). This result showed that *ced-4* and *ced-3* act downstream of *ced-9*, whereas *egl-1* acts upstream of *ced-9*. Thus, the four genes that act in a sequence in the central apoptotic pathway were identified (Figure 1.3).

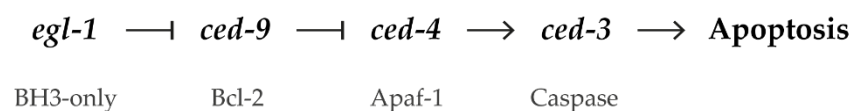


**Figure 1.3 The central apoptotic pathway.** The central apoptotic pathway in *C. elegans* consists of four genes acting in a sequence – *egl-1*, *ced-9*, *ced-4* and *ced-3*. The mammalian homologs of the four genes are mentioned under the genes. Adapted from (Conradt & Xue, 2005).

### 1.1.3 Biochemical and structural pathway of apoptosis in *C. elegans*

The discovery of the genetic pathway of apoptosis in worms fueled studies to decipher how apoptosis was being triggered molecularly. Firstly, CED-3 was shown to be similar to a human protease enzyme called Interleukin-1 $\beta$  converting enzyme (ICE) (Cerretti et al., 1992; Thornberry et al., 1992; Xue et al., 1996). Both, CED-3 and ICE, are caspases i.e. proteases that contain a cysteine residue in their active site and cleave target proteins at aspartic acid residues (Nicholson, 1999). CED-4 was shown to be

similar to the human Apaf-1 (apoptotic protease activating factor), capable of oligomerizing and recruiting caspases to trigger apoptosis (Zou et al., 1997). CED-9 protein is similar to the human proto-oncogene Bcl-2 (B-cell lymphoma), which is a member of the Bcl-2 family of proteins containing one or more Bcl-2 homology (BH) domains (Bakhshi et al., 1985; Cleary et al., 1986; Tsujimoto & Croce, 1986). EGL-1 protein was found to show homology to a subgroup of the Bcl-2 family of proteins called the BH3-only proteins (Conradt & Horvitz, 1998).

In surviving cells, the anti-apoptotic protein CED-9 is localized on the outer mitochondrial membrane and binds to a CED-4 dimer to form the CED-9-CED-4 complex (Figure 1.4) (Chen et al., 2000; Yan et al., 2005). Binding of CED-9 to CED-4 prevents oligomerization of CED-4, which inhibits the formation of the apoptosome and prevents apoptosis (Figure 1.4) (Yan et al., 2004). In most of the 131 cells destined to undergo apoptosis, *egl-1* is expressed, and the EGL-1 protein binds to CED-9 in the CED-9-CED-4 complex (Figure 1.4) (Yan et al., 2004). Binding of EGL-1 to CED-9 leads to a conformational change in CED-9 resulting in the release of the CED-4 dimer from the CED-9-CED-4 complex (Figure 1.4) (Conradt & Horvitz, 1998; del Peso et al., 1998; Parrish et al., 2000; Yan et al., 2004). The released CED-4 dimer oligomerizes to form an octameric apoptosome (Qi et al., 2010). Subsequently, inactive CED-3 zymogens (proCED-3) bind to the caspase-recruitment domains of the CED-4 apoptosome, allowing autocleavage of proCED-3 to form active CED-3 dimers (Figure 1.4) (Seshagiri & Miller, 1997; Zou et al., 1999). Active CED-3 dimers then cleave various target proteins that lead to the characteristic morphological changes and engulfment of the apoptotic cells (Conradt et al., 2016).

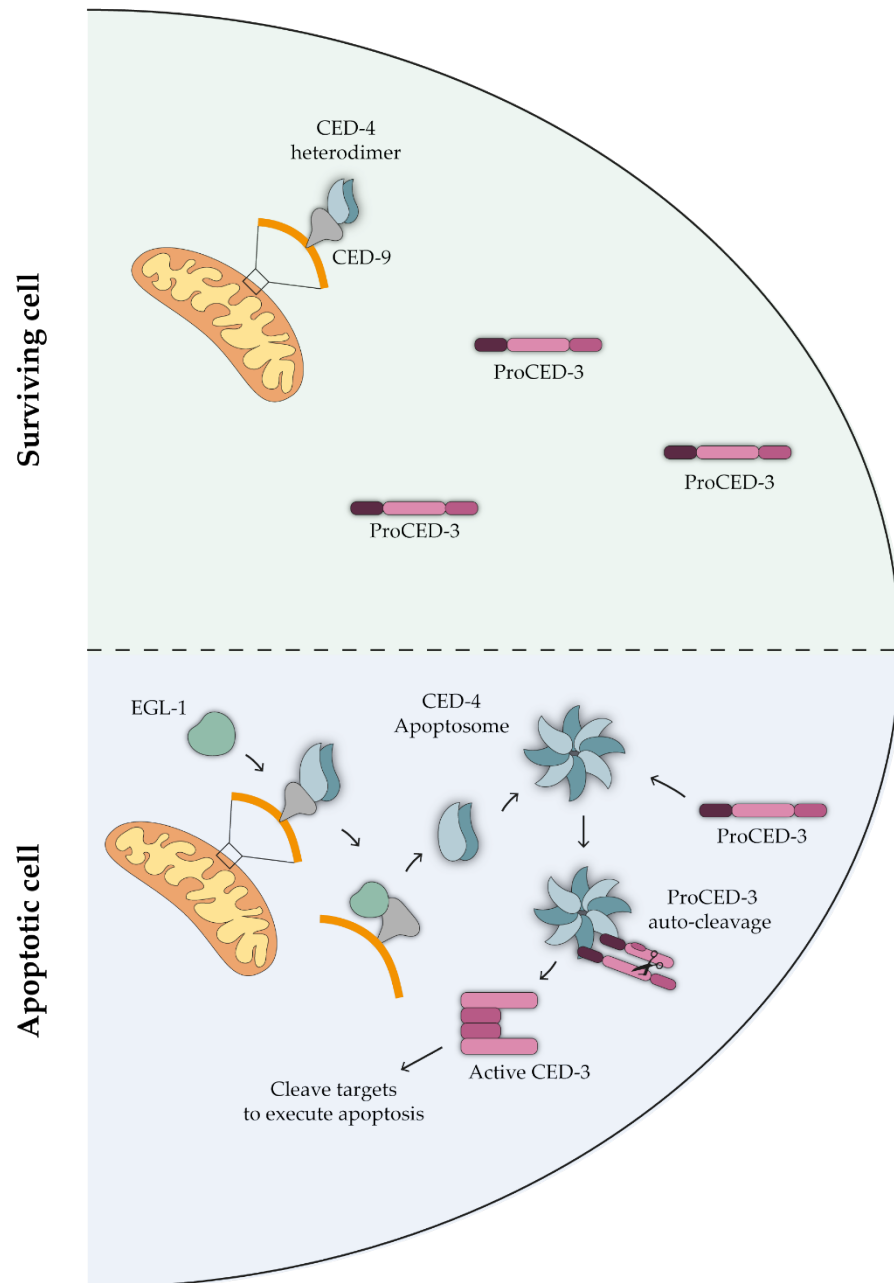


**Figure 1.4 Biochemical pathway of apoptosis in *C. elegans*.** In cells that survive, CED-9 on the outer mitochondrial membrane binds to CED-4 dimer and sequesters it. As a result, proCED-3 zymogen is inactive. In apoptotic cells, EGL-1 binds to CED-9, leading to the release of CED-4 dimer and apoptosome formation. As a result, proCED-3 zymogens can bind to the apoptosome, leading to auto-cleavage and dimerization to form active CED-3 dimers that execute apoptosis. Adapted from (Conradt & Xue, 2005).

#### 1.1.4 *ced-3* caspase acts as an executioner of apoptosis

The most downstream gene in the central apoptotic pathway in *C. elegans*, *ced-3* (cell death abnormal), codes for a member of the Interleukin-1 converting enzyme (ICE) family of proteases called caspases (Alnemri et al., 1996; Yuan et al., 1993). Caspases contain a cysteine residue in their active site and can cleave target proteins at aspartic acid residues (Nicholson, 1999). CED-3 protein is synthesized as an inactive zymogen (proCED-3) that contains a CARD (caspase activation an recruitment domain) domain called the Pro-domain, a 17 kDa domain (p17) and a 15 kDa domain (p15) (Xue et al., 1996). In order for CED-3 to become fully active, two proCED-3 zymogens have to be recruited to the CED-4 apoptosome, enabling proximity-mediated auto-cleavage of the CARD domain and subsequent homodimerization of the p17 and p15 domains (Figure 1.4) (Huang et al., 2013). The active CED-3 dimer then acts as an effector caspase that cleaves various target proteins that ultimately leads to the breakdown of the cell and its subsequent engulfment (Conradt et al., 2016). The execution of apoptosis is a highly regulated disassembly process, which includes nuclear DNA fragmentation, shrinkage of the cytoplasm and exposure of the 'eat-me' signal on the cell surface for subsequent engulfment (Conradt et al., 2016). The targets of CED-3 cleavage that execute apoptosis include DCR-1 (involved in nuclear DNA fragmentation), CED-8 (involved in exposure of the 'eat-me' signal), CED-9 and CNT-1 (Conradt et al., 2016). *In vitro* studies have also identified multiple other targets of CED-3 cleavage, including cytoskeletal proteins such as actin, myosin light chain, tubulin as well as proteins involved in ATP synthesis and cellular metabolism (Taylor et al., 2007).

## 1.2 The actomyosin network in non-muscle cells

---

The cytoplasm of animal cells contains an organized network of protein filaments, collectively called the cytoskeleton. The spatial and mechanical functions of the cell, such as cell migration, cell division, cytokinesis and cell shape changes, depend on the cytoskeleton (Jaeken, 2007). The cytoskeleton consists of three families of protein filaments – actin filaments, microtubules and intermediate filaments (Fletcher & Mullins, 2010). For this thesis, I will focus only on actin filaments, specifically the actomyosin network. The actomyosin network is a contractile complex within the cytoskeleton consisting of cross-linked actin filaments and myosin motor proteins (Niederman & Pollard, 1975). These actomyosin contractile fibers are an essential part of skeletal muscle function, where they are organized as highly ordered and polarized arrays to bring about uniform contraction or uniform relaxation of muscles (Huxley, 2000). Apart from skeletal muscles, the actomyosin network also plays essential and diverse functions in non-muscle cells such as cell adhesion, cell migration, cell polarity, cell division and cytokinesis (Jaeken, 2007). All of the functions performed by the actomyosin network in non-muscle cells is based on its ability to be contractile. But how is this contractile force generated?

In non-muscle cells, actin filaments are cross-linked with a specific family of myosin motor proteins called non-muscle myosin II (referred to as myosin II) (Huxley, 2000). Myosin II consists of two heavy chains, two regulatory light chains and two essential light chains (Figure 1.5, A) (McMillan & Scarff, 2022; Yang et al., 2020). Each heavy chain has a globular head that attaches to the actin filaments (Figure 1.5, A, C). The two types of light chains are bound close to the globular head of the heavy chains (Figure 1.5, A). Phosphorylation of the regulatory light chains in myosin II triggers the formation of bipolar filaments of myosin II consisting of 15-20 molecules (Figure 1.5, B) (Niederman & Pollard, 1975). These bipolar myosin II filaments cross-link with actin filaments in a randomly organised manner without any particular orientation,

resulting in random local densities of actomyosin fibres in non-muscle cells (Figure 1.5, D) (Kane, 1983; Pollard & Korn, 1973; Stossel, 1984). Contractility of the actomyosin fibres is ATP-dependent, where myosin II heads can bind to ATP, leading to its hydrolysis. The energy of ATP hydrolysis is coupled to the movement of the myosin II heads towards the plus-end of the cross-linked actin filament (Vale & Milligan, 2000). The collective movement of the myosin II heads towards the plus-end of actin filaments leads to a shortening of the actomyosin fibres by as much as 25%, and thereby causing contractility (Figure 1.5, C) (Kreis & Birchmeier, 1980). Since the actomyosin fibres in non-muscle cells are randomly organised, contractility is usually non-uniform, where only local densities of actomyosin fibres undergo contractions and relaxations (Figure 1.5, D) (Cowan & Hyman, 2007).



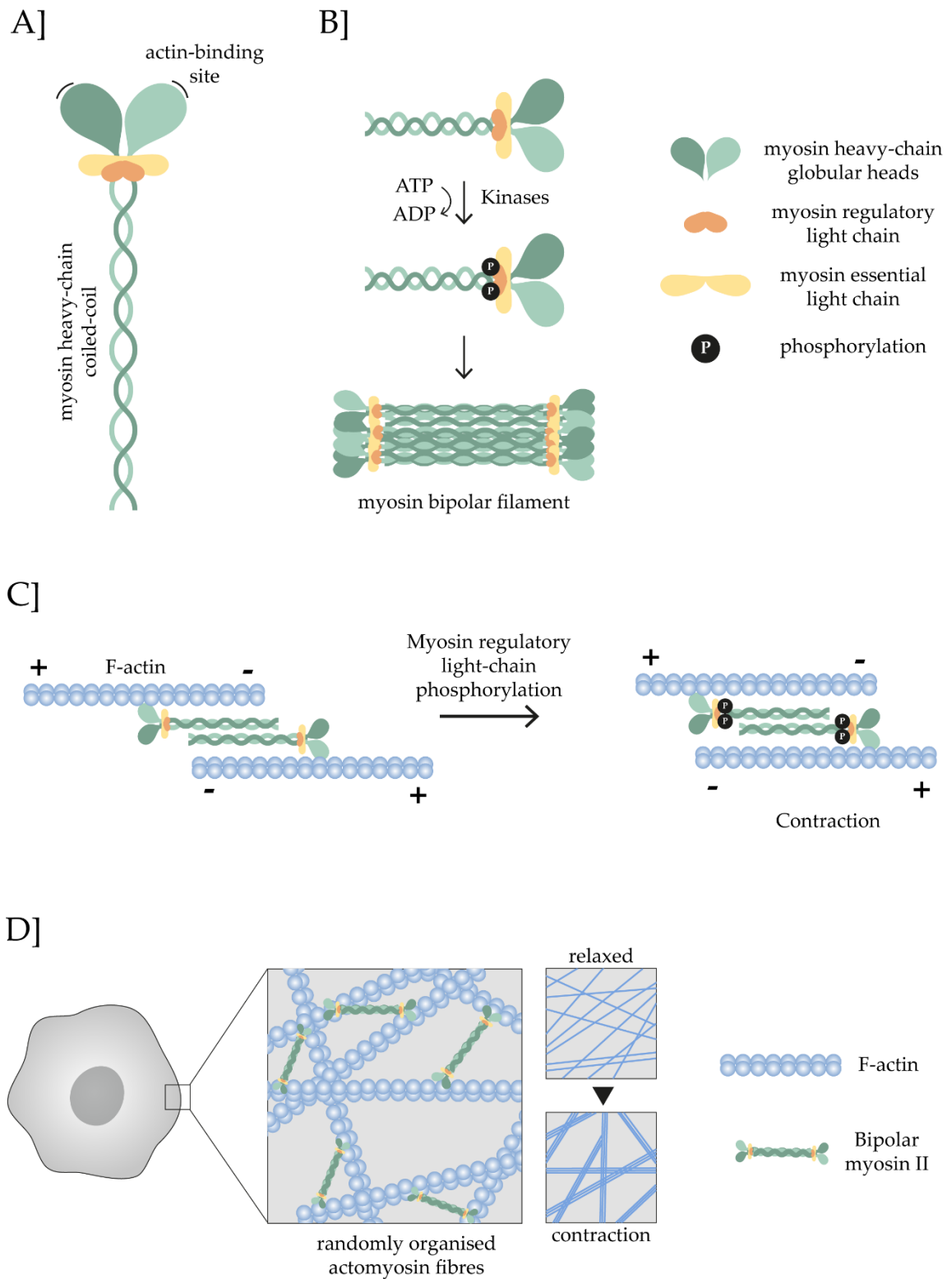


**Figure 1.5 The actomyosin network in non-muscle cells.** A] Structure of non-muscle Myosin II, which consists of two heavy chains, two regulatory light chains and two essential light chains. B] Phosphorylation of the regulatory light chains in Myosin II by kinases leads to the

formation of bipolar filaments. C] Myosin II filaments cross-link with actin filaments via their globular heads on the heavy chains. Phosphorylation of the regulatory light chains leads to movement of the myosin II molecules towards the plus ends of the actin filament, resulting in contraction of the filaments (F-actin is filamentous actin). D] The cortex of non-muscle cells contains randomly organized actomyosin fibers, where only local densities of filaments undergo contractions. Figure adapted from (Cowan & Hyman, 2007).

### **1.2.1 Regulators of the actomyosin network and contractility**

In non-muscle cells, the actomyosin network regulates a variety of functions such as maintaining cellular architecture, cell shape changes, cell migration and cytokinesis. To facilitate these functions, the actomyosin network must be assembled and must generate contractility at the correct time and correct location. Such spatio-temporal regulation of actomyosin contractility requires the involvement of various regulatory proteins and co-factors (Agarwal & Zaidel-Bar, 2019). Data mining of literature and protein databases identified a network of more than 100 proteins that regulate actomyosin contractility, and these regulatory proteins were collectively referred to as the “contractome” (Zaidel-Bar et al., 2015). In brief, spatio-temporal regulation of the actomyosin network is achieved via two processes – actin polymerization and myosin activation (Agarwal & Zaidel-Bar, 2019). The first process, actin polymerization, is mediated by a variety of factors that promote nucleation of globular actin (G-actin) to filamentous actin (F-actin) (Chesarone & Goode, 2009). The most important and well-studied of these nucleation factors include Arp2/3 complex, which promotes formation of branched actin filaments, and Formins, which promote formation of linear parallel actin filaments (Pollard, 2007). The second process, myosin activation in non-muscle cells, is achieved by phosphorylation of the regulatory light chain in the myosin II molecule (Matsumura, 2005). Various kinases can phosphorylate the myosin regulatory light chain, such as Rho-associated coiled-coil containing protein kinase (ROCK) and myotonic dystrophy kinase-related Cdc42-binding-kinase (MRCK) (Arnold et al., 2017).

Although the contractome consists of 100 or more proteins, one particular family of proteins have been shown to play an essential role in regulating actomyosin contractility – it is the members of the Rho family of GTPases (collectively referred to as “Rho” from here on) (Agarwal & Zaidel-Bar, 2019; Mosaddeghzadeh & Ahmadian, 2021). Rho is inactive when bound to GDP and active when bound to GTP (Figure 1.6). RhoGEFs (guanine nucleotide exchange factors) facilitate the exchange of GDP to GTP, thereby activating Rho (Figure 1.6) (Cherfils & Zeghouf, 2013). One particular RhoGEF, called Ect2 (epithelial cell-transforming factor 2), has been very well-studied and shown to activate Rho to regulate cytokinesis (Basant & Glotzer, 2017; Schneid et al., 2021). In contrast, RhoGAPs (GTPase activating proteins) promote inactivation of Rho by stimulating the GTPase activity of Rho, such that GTP is hydrolyzed to GDP (Figure 1.6) (Cherfils & Zeghouf, 2013). Active GTP-bound Rho triggers a signaling cascade that leads to actin polymerization and myosin activation, thereby promoting actomyosin contractility (Agarwal & Zaidel-Bar, 2019). The most extensively studied function of Rho-mediated actomyosin contractility is during cytokinesis (Glotzer, 2005; Piekny et al., 2005). Briefly, active Rho binds to Formin, relieving it of its auto-inhibition (Alberts, 2001). Activated Formins then act as actin-polymerizing machines leading to formation of parallel actin filaments (Figure 1.6) (Pollard, 2007). Apart from actin polymerization, active Rho also triggers phosphorylation of the regulatory myosin light chain (rMLC) in non-muscle myosin II (Figure 1.6) (Piekny et al., 2005). Rho can activate ROCK, which subsequently phosphorylates rMLC on Serine 19 (Ser19) (Matsumura, 2005). Phosphorylation of rMLC leads to activation of myosin II, which then promotes contractility of the contractile ring during cytokinesis (Glotzer, 2005). In summary, actomyosin contractility is regulated via actin polymerization and myosin activation, which can be achieved via various regulators depending on the function.

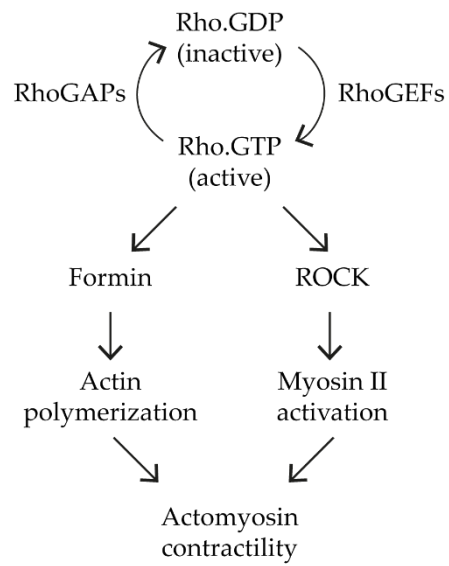


**Figure 1.6 Rho-mediated regulation of actomyosin contractility.** RhoGEFs promote the formation of active Rho.GTP molecules that subsequently activate formins and ROCK, which collectively lead to contractility of the actomyosin network. Adapted from (Piekny et al., 2005).

### 1.3 Asymmetric cell division

---

Animals do not only contain trillions of cells, but also a wide variety of cell-types – for example, humans have at least 400 different cell-types (Liu & Zhang, 2022). How a single-celled zygote achieves such diversity is truly remarkable. One of the key processes establishing this cellular diversity is asymmetric cell division. Asymmetric cell division is an evolutionarily conserved mechanism by which two daughter cells acquire distinct cell fates. In many cases, the unequal cell fate of the daughters is also accompanied by an unequal cell size, where the daughter cells are of different sizes. The daughter cells can acquire distinct fates either via extrinsic cues provided by the neighboring niche, or via asymmetric inheritance of intrinsic cell fate determinants such as proteins and/or organelles (Sunchu & Cabernard, 2020). A lot of the knowledge gained about asymmetric cell division has been obtained from studies in stem cells, *Drosophila melanogaster* and *Caenorhabditis elegans*. In the following section, I will describe asymmetric cell division during *C. elegans* development.

#### 1.3.1 Asymmetric cell division during *C. elegans* development

The very first cell division event of the fertilized *C. elegans* zygote is asymmetric by fate and size, which leads to the formation of the larger anterior cell called AB and the smaller posterior cell called P<sub>1</sub> (Figure 1.7) (Sulston et al., 1983). The subsequent five divisions are also asymmetric by fate and size, which lead to the formation of six founder cells – AB, MS, E, C, D and P<sub>4</sub> (Figure 1.7) (Sulston et al., 1983). The descendants of these founder cells will ultimately give rise to the specific cell types in adult worms (Figure 1.7) (Sulston & Horvitz, 1977; Sulston et al., 1983).

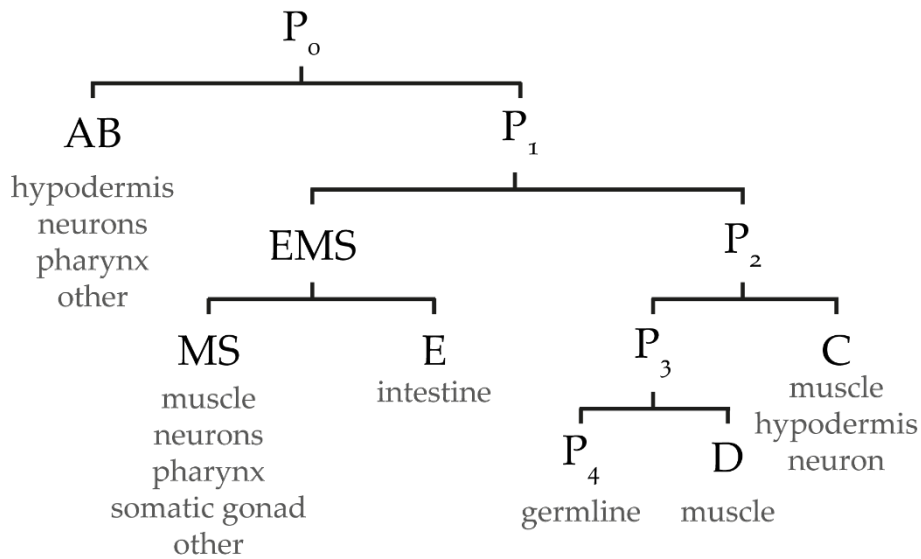


**Figure 1.7 Early divisions during *C. elegans* development.** The first five divisions during *C. elegans* development lead to the formation of the 6 founder cells - AB, MS, E, C, D and P<sub>4</sub>, which ultimately gives rise to all tissues in adult worms.

The asymmetry of the first cleavage of the one-cell zygote has been studied extensively and various mechanisms that establish this asymmetry have been discovered. In order to divide asymmetrically, the one-cell zygote first needs to gain polarity. To that end, a series of events leads to the one-cell zygote establishing anterior to posterior polarity (AP polarity). These events can be divided into three steps – symmetry breaking, establishment of AP polarity and maintenance of polarity (Rose & Gonczy, 2014). Symmetry breaking of the one-cell zygote is mediated entirely by centrosomes. Prior to symmetry breaking, the entire cortex of the one-cell embryo is uniformly contractile (Munro & Bowerman, 2009; Munro et al., 2004). Contractility of the cortex involves components of the actomyosin network such as RHO-1 (small GTPase of the Rho family), NMY-2 (non-muscle myosin II) and ECT-2 (Rho guanine nucleotide exchange factor) (Motegi & Sugimoto, 2006; Schonegg & Hyman, 2006). Symmetry breaking is triggered when the sperm-derived posterior centrosome promotes cessation of local contractility of the posterior cortex, most likely by inactivating RHO-1 (Figure 1.8) (Cowan & Hyman, 2004b; Motegi & Sugimoto, 2006; Schonegg & Hyman, 2006). The loss of contractility then spreads towards the anterior of the embryo, until it reaches

half of the zygote length (Figure 1.8) (Hird & White, 1993). Thus an anterior contractile domain and a posterior non-contractile domain is formed (Figure 1.8). The establishment of this anterior-posterior contractile polarity is accompanied by an asymmetric distribution of PAR proteins, encoded by *par* (partitioning defective) genes (Rose & Gonczy, 2014). The anterior cortical domain contains PAR-3, PAR-6 and PKC-3, together referred to as the “anterior PAR complex” (Figure 1.8) (Goldstein & Macara, 2007; Munro et al., 2004). The posterior cortical domain contains PAR-2, PAR-1 and LGL-1 (Munro et al., 2004). Subsequently, mutual inhibition of the anterior and posterior cortex proteins is responsible for maintaining this AP polarity (Rose & Gonczy, 2014). The anterior and posterior cortical PAR domains allow the formation of cytoplasmic gradients of various cell fate regulators such as PIE-1, MEX-5, MEX-6, POP-1, PAL-1, APX-1 and more, which ultimately leads to cell fate specification of the subsequent daughter cells during early embryogenesis (Rose & Gonczy, 2014). Once AP polarity has been established in the one-cell zygote, this polarity is translated into asymmetric spindle positioning, which ensures the asymmetric cleavage of the one-cell zygote to generate daughter cells of different sizes (Figure 1.8) (Galli & van den Heuvel, 2008; McNally, 2013). In animal cells, the cleavage furrow bisects the mitotic spindle during anaphase. Therefore, for the one-cell zygote to divide asymmetrically by size, the mitotic spindle needs to be positioned asymmetrically. To that end, a ternary complex comprising of GPR-1/2 and LIN-5 exerts pulling forces on astral microtubules that ensure the correct positioning of the mitotic spindle biased towards the posterior (Cowan & Hyman, 2004a). The cleavage furrow subsequently bisects the posteriorly biased mitotic spindle to form a larger anterior daughter AB and a smaller posterior daughter called P<sub>1</sub> (Figure 1.8). The AP polarity ensures that the two daughters inherit distinct cell fate determinants. In summary, the asymmetric division of the one-cell *C. elegans* embryo is very well-studied. In fact, *C. elegans* is an excellent model organism to study asymmetric cell division in general, as it can be observed by looking at the invariant cell lineage that almost all somatic divisions might be asymmetric by fate (Sulston & Horvitz, 1977; Sulston et al., 1983).

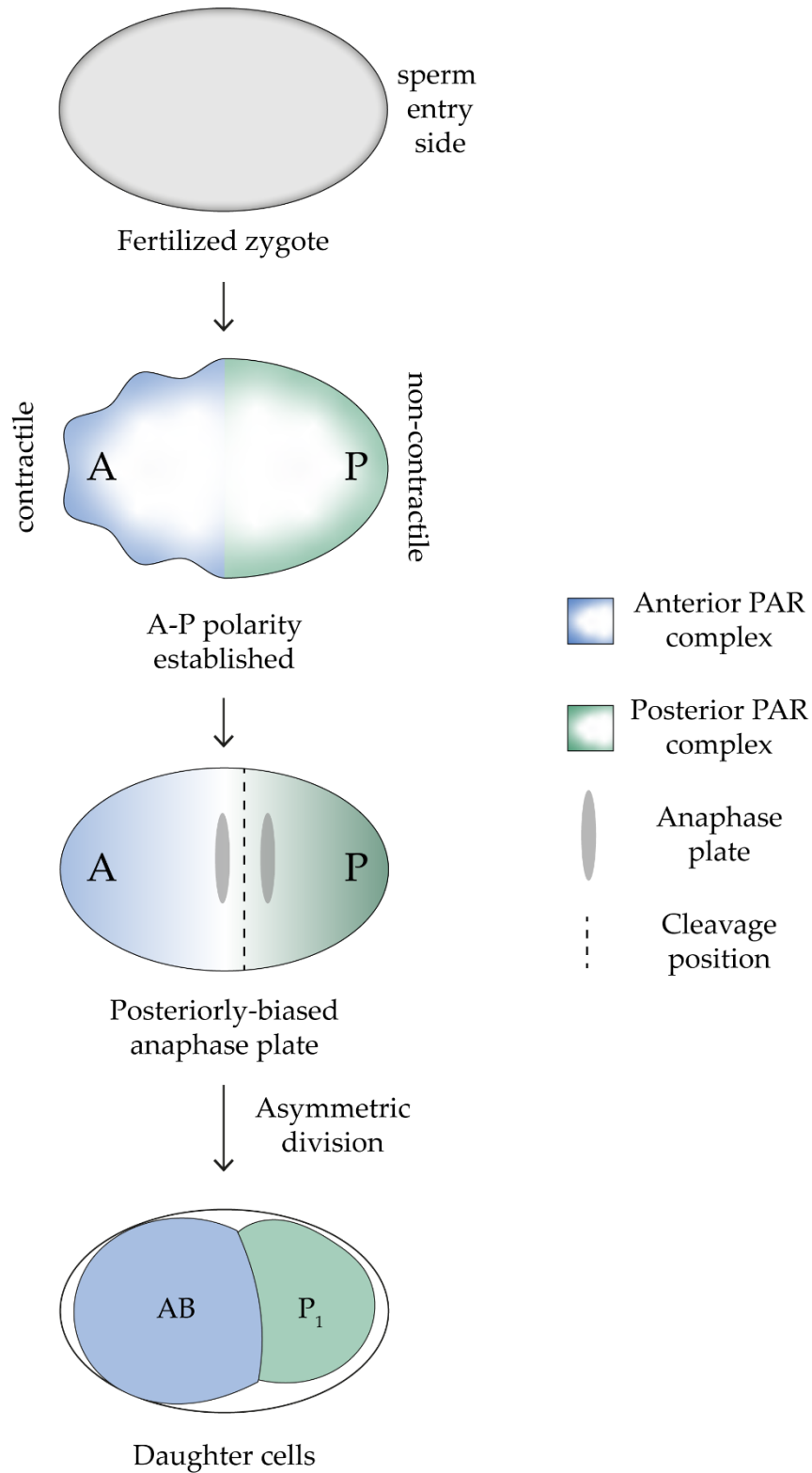


**Figure 1.8 Asymmetric division of the one-cell *C. elegans* zygote.** The sperm entry side of the one-celled zygote forms the posterior end of the zygote. The anterior (A) side of the embryo is contractile, whereas the posterior (P) side is non-contractile. A-P polarity is translated into a posteriorly-biased anaphase plate, which leads to asymmetric division of the



one-cell zygote, thereby forming a larger AB cell and a smaller P1 cell. Adapted from (Rose & Gonczy, 2014).

Although many studies have focused on asymmetric cell division by fate, the knowledge about asymmetric cell division by size during *C. elegans* development is still limited. Asymmetric cell division by size has only been investigated in the first few cell divisions as well as in some neuronal lineages, where the neuroblast divides asymmetrically by size (Hatzold & Conradt, 2008; Mishra et al., 2018). For example, the NSM (neurosecretory motor neuron) neuroblast divides asymmetrically by size to generate a smaller daughter that undergoes apoptosis and a larger daughter that differentiates to form a neuron (Hatzold & Conradt, 2008). However, a thorough investigation of all asymmetric cell divisions by size during *C. elegans* development has not been done, at least to the best of my knowledge. The only study that investigated general size asymmetry was performed by Fickentscher and Weiss in 2017, where they showed that about 40% of all cell divisions until gastrulation of the *C. elegans* embryo are asymmetric by size (Fickentscher & Weiss, 2017). In this study, I will mostly focus on asymmetric cell division by size and its mechanisms.

What are the mechanisms that lead to asymmetric cell division by size? Studies in *Drosophila melanogaster*, *Saccharomyces cerevisiae* and *C. elegans* have shown that asymmetric cell division by size can be achieved via two mechanisms (Sunchu & Cabernard, 2020). The first, is a spindle-dependent mechanism, where an asymmetric spindle position dictates where the cleavage furrow will bisect (like the one-cell *C. elegans* zygote). The second, is a spindle-independent mechanism, where the spatiotemporal dynamics of the actomyosin network leads to an unequal cortical expansion resulting in daughter cells of different sizes. In the next section, I will describe the spindle-independent mechanism of generating cell size asymmetry.

### 1.3.2 The role of the actomyosin network in asymmetric cell division by size

Although asymmetric spindle position has been established as the primary determinant of asymmetric cell division by size, recent studies in *Drosophila melanogaster* and *C. elegans* neuroblasts have found a spindle-independent, actomyosin-dependent mechanism of asymmetric cell division by size (Cabernard et al., 2010; Connell et al., 2011; Ou et al., 2010; Tsankova et al., 2017; Wei et al., 2020). The most well-studied example is in *Drosophila* neural stem cells called neuroblasts. *Drosophila* neuroblasts have an apical-basal polarity and divide asymmetrically to generate a smaller basal daughter cell that will differentiate to form a ganglion mother cell (GMC) and a larger apical daughter cell that forms a self-renewed neuroblast (Doe, 2008). The asymmetric division by size of these neuroblasts is mediated by the spatiotemporal dynamics of Non-muscle myosin II (Myosin II) localization and activity (Figure 1.9) (Tsankova et al., 2017). Before nuclear envelope breakdown (NEB), Myosin II is uniformly localized to the cortex in the neuroblast. However, during NEB, Myosin II becomes enriched on the apical cortex. Subsequently, at anaphase onset, Myosin II is cleared from the apical cortex via cortical flows and re-localizes to the cleavage furrow (Figure 1.9). The clearing of Myosin II from the apical cortex enables the expansion of the apical cortex before cleavage, thereby leading to the formation of a larger apical daughter cell (Figure 1.9). The re-localization dynamics of Myosin is mediated by Pins (Partner of Inscuteable or LGN/AGS3 in vertebrates), Rok (Rho kinase or ROCK1/2 in vertebrates), Pkn (Protein Kinase N or Pkn1-3 in vertebrates) and probably other polarity cues (Tsankova et al., 2017). The correct timing of Myosin II dynamics is essential for the physical asymmetry of this neuroblast division. For example, *pkn* mutant neuroblasts fail to clear Myosin II from the apical cortex at anaphase onset, thereby resulting in defects in asymmetric cell division by size (Tsankova et al., 2017). Biophysical studies also revealed that Myosin II re-localization is accompanied by changes in hydrostatic pressure within the *Drosophila* neuroblasts, which establishes the size asymmetry in the daughter cells (Pham et al., 2019). Clearing the apical cortex of Myosin II-mediated tension during the onset of anaphase

allows for pressure-driven expansion of the apical cortex (Pham et al., 2019). Taken together, studies in *Drosophila* neuroblasts show that Myosin II re-localization coupled with changes in hydrostatic pressure drive spindle-independent asymmetric cell division by size. Furthermore, studies in two different *C. elegans* neuroblasts (QR.a and NSM neuroblast) also showed that Myosin II localization is important for their asymmetric cell division by size (Ou et al., 2010; Wei et al., 2020). For example, in NSM neuroblasts, Myosin II is localized to the side of the cortex that forms the larger daughter cell (Wei et al., 2020). Mutants where Myosin II is, instead, uniformly localized in NSM neuroblast cortex leads to symmetric division of the neuroblast (Wei et al., 2020). Overall, new studies are emerging, which show spindle-independent but actomyosin-dependent mechanisms of regulating asymmetric cell division by size. However, further elucidation into the molecular mechanisms is required.

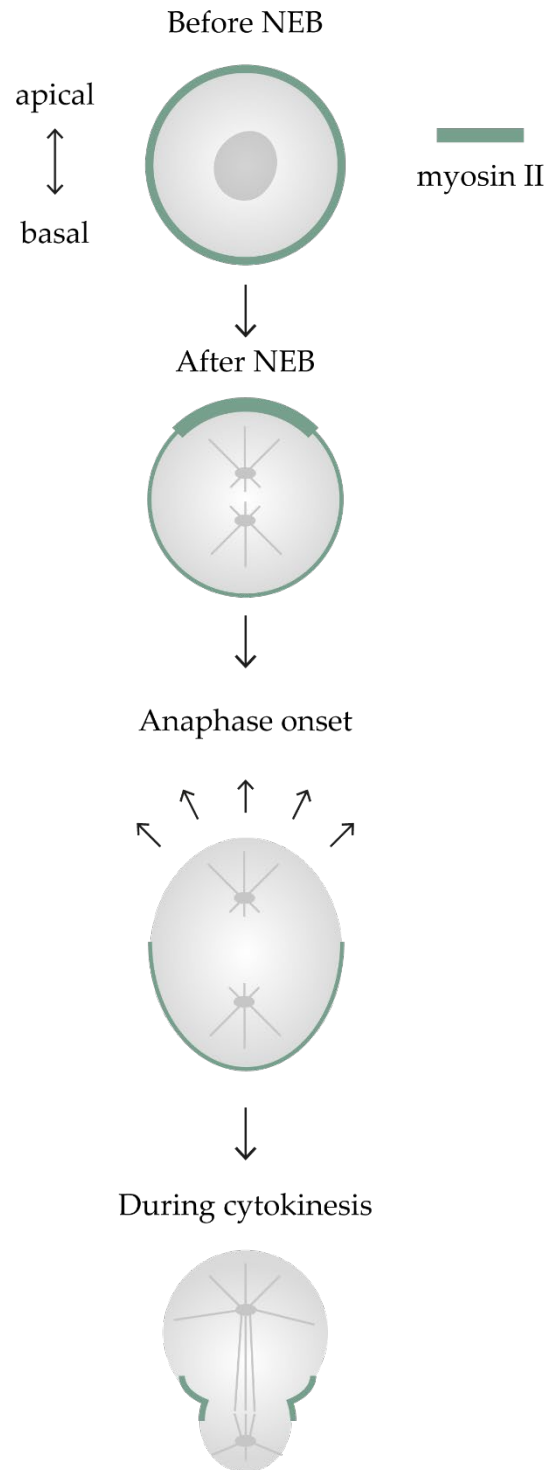


**Figure 1.9 Asymmetric division of *Drosophila* neuroblasts is regulated by Myosin II dynamics.** Before nuclear envelope breakdown (NEB), myosin II is uniformly distributed in the cortex. After NEB, myosin II enriches to the apical cortex and at anaphase onset, myosin II is cleared from the apical cortex, which leads to expansion of the apical side. During cytokinesis, myosin II is enriched at the cleavage furrow. Adapted from (Tsankova et al., 2017).

## 1.4 The NSM lineage in *C. elegans* to study apoptosis and asymmetric cell division

---

The major aim of my thesis involved studying apoptosis and asymmetric cell division in *C. elegans*. The neurosecretory motor neuron (NSM) lineage provided an excellent opportunity to study these phenomena *in vivo*. The NSM neuron is a serotonergic motor neuron with a possible neurohumoral function involved in sensing the presence of food (Riddle et al., 1997). There are two bilaterally symmetric NSM neurons, the NSM left and the NSM right, which are identical functionally and genetically (Axang et al., 2008; Sulston et al., 1983). The mother of the NSM neuron, called the NSM neuroblast (NSMnb), is generated approximately 230 minutes post-fertilization of the *C. elegans* oocyte (Figure 1.10). Around 180 minutes later, which is 410 minutes post-fertilization, the NSMnb undergoes an asymmetric cell division event to form two daughter cells that are unequal in size and fate (Figure 1.10). The smaller daughter cell is called the NSM sister cell (NSMsc) and the larger daughter cell is the NSM neuron. The NSMsc undergoes apoptotic cell death and forms a corpse approximately 20 minutes after being generated (Figure 1.10). The NSM differentiates to form a serotonergic motor neuron (Sulston & Horvitz, 1977; Sulston et al., 1983). The unequal size of the two daughter cells and the apoptotic death of the NSMsc make the NSM lineage an ideal system to study the interplay between cell size and apoptosis.

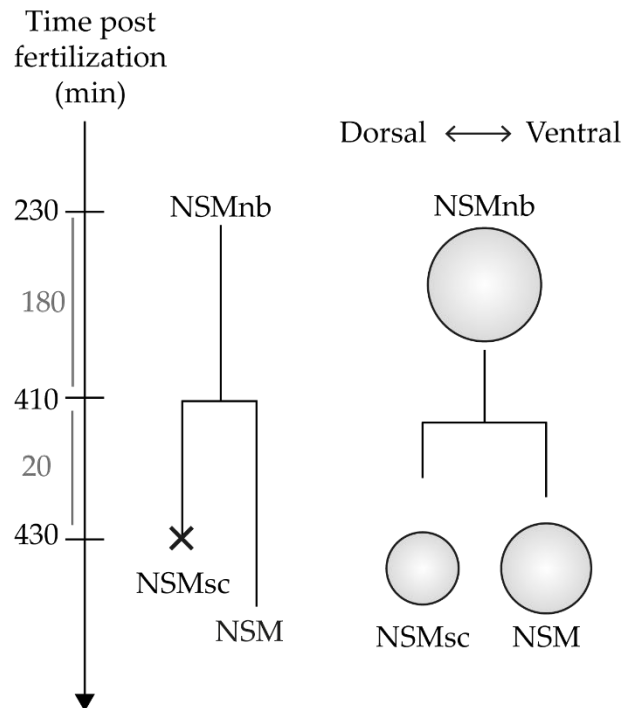


**Figure 1.10 Schematic of the NSM lineage in *C. elegans*.** The NSM neuroblast (NSMnb) is generated 230 minutes post-fertilization. 180 minutes later, the NSMnb divides asymmetrically to generate a smaller dorsal daughter called the NSM sister cell (NSMsc) and a larger ventral daughter cell called the NSM. The NSMsc undergoes apoptosis (marked by an X) in 20 minutes after being generated.

#### 1.4.1 Mechanisms that ensure the apoptotic death of the NSMsc

Multiple studies identified the various mechanisms that ensure that only the NSMsc undergoes programmed cell death via apoptosis. Similar to most apoptotic deaths in *C. elegans*, the apoptotic death of the NSMsc is dictated by the up-regulation of the pro-apoptotic *egl-1* gene and thereby activation of the central apoptotic pathway (Hatzold & Conradt, 2008; Thellmann et al., 2003; Wei et al., 2020). Loss-of-function mutations of the pro-apoptotic genes (*ced-3*, *ced-4* and *egl-1*) or gain-of-function mutations of the anti-apoptotic gene (*ced-9*), lead to the inappropriate survival of the NSMsc. But, how is *egl-1* expression regulated in the NSM lineage and how is its expression limited specifically to the NSMsc?

The *egl-1* locus has been shown to have four binding sites for Snail family transcription factors (Thellmann et al., 2003). These Snail-binding sites are collectively located in a regulatory region of the *egl-1* locus called "Region B". In the NSMsc that is

programmed to undergo apoptosis, a heterodimer of two basic helix-loop-helix (HLH) proteins, HLH-2 and HLH-3, binds to Region B, thereby most-likely inducing the expression of *egl-1* in the NSMsc and leading to its apoptotic fate (Figure 1.11) (Thellmann et al., 2003). Knockdown by RNA interference (RNAi) of either *hlh-2* or *hlh-3* leads to inappropriate survival of the NSMsc (Thellmann et al., 2003). In contrast, in the surviving NSM cell, HLH-2/3 binding to *egl-1* Region B is antagonized by the Snail-like transcription factor CES-1 (cell-death specification) (Figure 1.11) (Ellis & Horvitz, 1991; Hatzold & Conradt, 2008; Metzstein & Horvitz, 1999; Thellmann et al., 2003). There are higher levels of CES-1 protein in the NSM compared to the NSMsc (Figure 1.11) (Hatzold & Conradt, 2008; Wei et al., 2020). It has been suggested that the high levels of CES-1 in the NSM outcompetes HLH-2/3 binding to Region B, thereby repressing the expression of *egl-1* leading to the survival of the NSM (Thellmann et al., 2003). Overall, the fate of the NSMsc and NSM is determined by the levels of CES-1 – the NSM has higher levels of CES-1 leading to repression of *egl-1*, whereas, NSMsc has low levels of CES-1, thereby allowing *egl-1* expression via HLH-2/3 binding to Region B.

There have also been studies on how the asymmetric segregation of CES-1 to the NSMsc and NSM is regulated. Wei et al., 2020 showed that a ventral to dorsal gradient of CES-1 protein is formed in the NSMnb resulting in the NSM inheriting more CES-1 protein (Figure 1.11) (Wei et al., 2020). Furthermore, this gradient of CES-1 in the NSMnb depends on *pig-1* (par-1 like gene), which encodes for a MELK-like kinase (maternal embrionic leucine zipper kinase) (Ganguly et al., 2015; Wei et al., 2020). Overexpression of *ces-1* using extra-chromosomal arrays also leads to survival of the NSMsc, most likely because it inherits a high level of CES-1, which antagonizes the binding of HLH-2/3 to the *egl-1* Region B (Metzstein & Horvitz, 1999). Two more genes were also identified to act upstream of *ces-1* in the NSMnb – *ces-2* and *dnj-11*. *ces-2* codes for a bZIP (basic leucine-zipper) transcription factor (Metzstein et al., 1996), whereas, *dnj-11* encodes a DnaJ domain containing MIDA1 (mouse Id associated 1) chaperone protein (Hatzold & Conradt, 2008). Loss-of-function mutations in either

*ces-2* or *dnj-11* lead to inappropriate survival of the NSMsc (Hatzold & Conradt, 2008). Furthermore, it was shown that both *dnj-11* and *ces-2* cooperate to negatively regulate *ces-1* expression in the NSMnb, such that the NSMsc has low levels of CES-1 protein, leading to its death (Hatzold & Conradt, 2008). Overall, multiple mechanisms ensure the apoptotic death of the NSMsc and survival of the NSM.

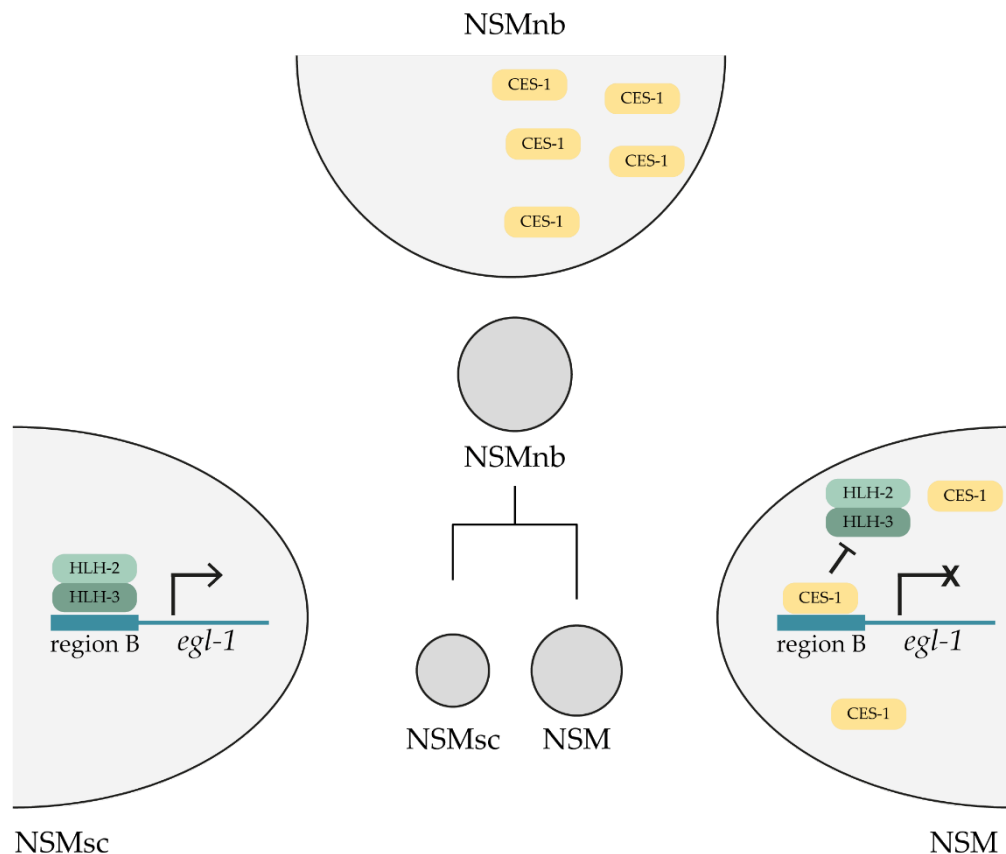


**Figure 1.11 Mechanisms that ensure the apoptotic death of the NSMsc and survival of the NSM.** There is more CES-1 protein in the ventral side of the NSMnb, leading to the ventral daughter (NSM) inheriting higher levels of CES-1. Thereby, in the NSM, binding of CES-1 to region B of *egl-1* locus outcompetes the binding of HLH-2/3 transcription factor. As a result, *egl-1* is not expressed in the NSM and it survives. Conversely, in the NSMsc, binding of HLH-2/3 to region B induces the expression of *egl-1*, thereby leading to its apoptosis. Adapted from (Hatzold & Conradt, 2008).



### 1.4.2 Factors promoting asymmetric division by size of the NSMnb

The NSMnb divides asymmetrically by size to form a smaller NSMsc and a larger NSM. The NSMsc is approximately 0.6 times smaller than the NSM. Previous studies identified various factors that regulate the asymmetric division of the NSMnb and thus, the unequal sizes of the daughter cells. The gene *pig-1* (par-1 like gene), which encodes a MELK (maternal embryonic leucine zipper kinase), was shown to play an essential role in the asymmetric division of the NSMnb (Wei et al., 2020). Complete loss-of-function mutations of *pig-1* resulted in the symmetric division of the NSMnb and thereby, equally sized NSMsc and NSM (Wei et al., 2020; Wei et al., 2017). In the study by Wei et al., 2020, other factors that act in the same pathway as *pig-1* to promote asymmetric division of the NSMnb were identified. It was shown that *pig-1*-dependent phosphorylation of non-muscle myosin II (NMY-2) is required for the asymmetric enrichment of NMY-2 in the NSM neuroblast and that this asymmetric enrichment of NMY-2 is required for the formation of unequally sized NSMsc and NSM (Figure 1.12) (Wei et al., 2020). Disruption of this asymmetric enrichment of NMY-2 by either loss-of-function of *pig-1* or by partial temperature-sensitive loss of *nmy-2* results in equally sized NSMsc and NSM. Furthermore, *par-4* LKB1, *strd-1* STRAD $\alpha$  and *mop25.1/2* MO25 $\alpha$  were shown to act upstream of *pig-1* to promote the asymmetric division of the NSMnb (Figure 1.12). Overall, Wei et al., 2020, identified a linear pathway, which will be referred to as the “*pig-1-nmy-2* axis”, that promotes the asymmetric division of the NSMnb and unequal sizes of the daughters, the NSMsc and the NSM.

Apart from the *pig-1-nmy-2* axis, other factors that promote asymmetric division of the NSMnb have also been identified. For example, in the study conducted by Hatzold and Conradt 2008, *dnj-11* MIDAI and *ces-2* HLF were shown to promote asymmetric division of the NSMnb (Hatzold & Conradt, 2008). Loss-of-function mutations in *dnj-11* or *ces-2* led to equally sized NSM and NSMsc. Conversely, a gain-of-function mutation in *ces-1* also prevented asymmetric NSMnb division and led to equally sized daughter cells, indicating its antagonistic role in asymmetric division (Hatzold & Conradt, 2008).

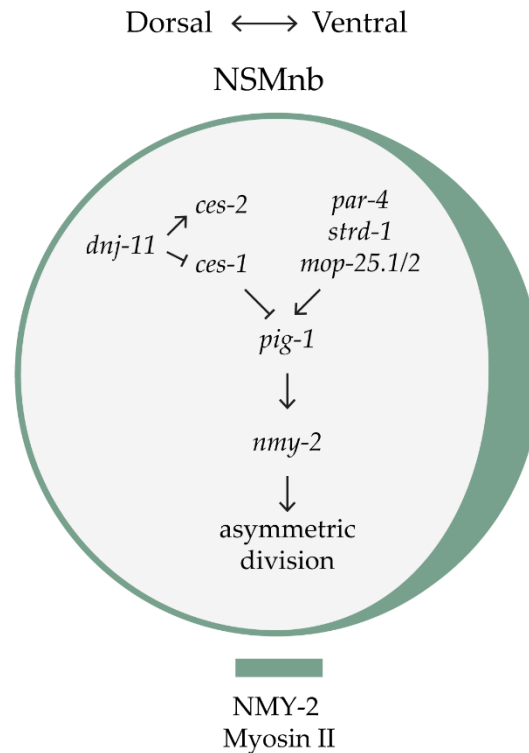


**Figure 1.12 The *pig-1-nmy-2* axis promotes the asymmetric division of the NSMnb.** In the NSMnb, NMY-2 myosin II is enriched on the ventral side, which is required for the NSMnb to divide asymmetrically. Genetically, there exists a *pig-1-nmy-2* axis that promotes the asymmetric division of the NSMnb. Adapted from (Wei et al., 2020).

### 1.4.3 Visualizing the NSM lineage *in vivo*

One of the reasons I chose the NSM lineage to study apoptosis and asymmetric division is because of the tools available to study this lineage *in vivo*. The NSM lineage can be visualized in developing *C. elegans* embryos using a plasma membrane marker  $P_{pie-1}mCherry::ph^{plc\delta}$ , which labels the boundaries of all cells in the embryo (Figure 1.13, A). In comma and 1.5 fold-stage embryos, the NSMnb cell can be identified based on its position and the pattern of the neighboring cells (Figure 1.13, A). Live imaging of the embryos allows tracking the division of the NSMnb into its two daughter cells – NSMsc and NSM. The NSMnb divides along the dorsal-medial to the ventral-lateral axis, such that the NSMsc is positioned dorsally and the NSM is positioned ventrally (Figure 1.13, A) (Wei et al., 2017). The *in vivo* tracking of NSMnb division allows us to

investigate its division asymmetry as well as distribution of various macromolecules in the lineage. Furthermore, the NSM neuron can be visualized in larvae and adults using the serotonergic neuron reporter *Ptph-1::his-24::gfp* (*bcIs66* or *bcIs65*) (Figure 1.13, B) (Yan et al., 2013). This reporter labels the nuclei of serotonergic neurons and NSM neuron can be identified in the lower half of the anterior pharynx of L3/L4 larvae (Figure 1.13, B). In various cell death mutants, the NSMsc survives and an extra 'NSM' like neuron can also be seen in the anterior pharynx (Figure 1.13, B). Overall, the NSM lineage can be studied in developing embryos as well as in larvae and adults, thereby making it a great system to study cell death and cell size.

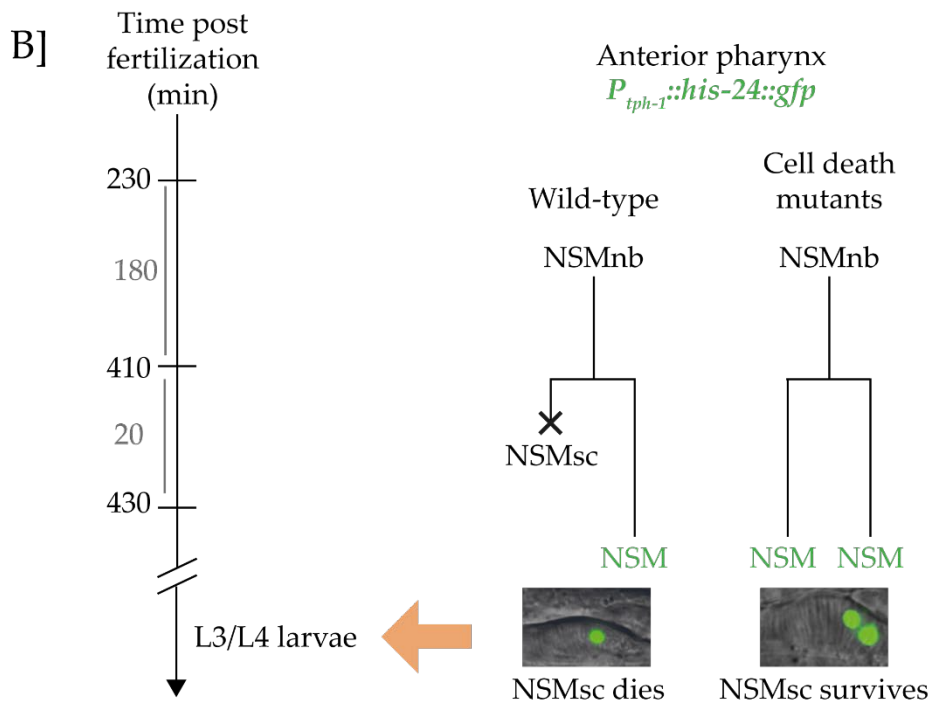
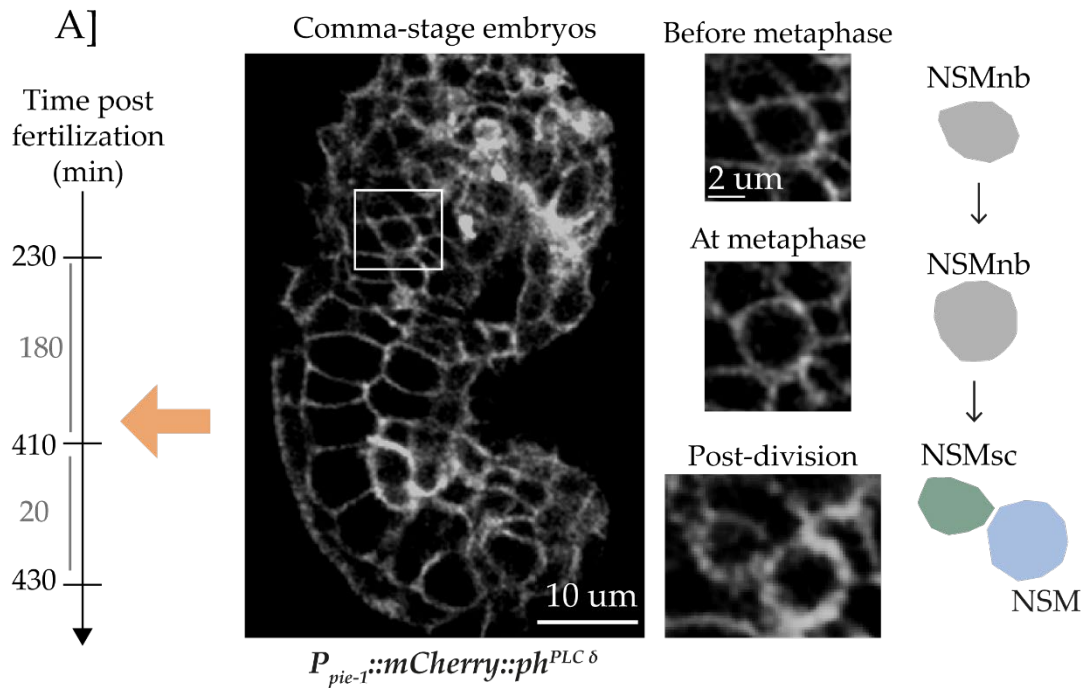


**Figure 1.13** There are two methods to visualize the NSM lineage *in vivo*. A] In developing comma-stage embryos, the NSMnb can be identified using a cell boundary marker *P<sub>pie-1</sub>::mCherry::ph<sup>PLC $\delta$</sup>* . The white box highlights the NSMnb before metaphase. Subsequently, the division of the NSMnb can be tracked and the two daughter cells, the NSMsc and NSM, can also be identified. B] In L3/L4 larvae, the NSM neuron can be identified in the anterior pharynx using a serotonergic neuron reporter *P<sub>tph-1</sub>::his-24::gfp*. In certain cell death mutants, the NSMsc survives to form a NSM-like neuron.

## 1.5 Background and aim of the study

---

The gene *ced-3* has a very well-established role in the execution of apoptosis in cells programmed to die. However, recently it was shown that also the mothers of cells programmed to die show CED-3 caspase activity (Chakraborty et al., 2015; Mishra et al., 2018). Specifically, it was shown that in the NSM neuroblast, a dorsal to ventral gradient of CED-3 caspase activity is generated before its division (Figure 1.14, A) (Chakraborty et al., 2015). The dorsal part of the NSM neuroblast, which has higher CED-3 caspase activity, forms the smaller daughter cell, which undergoes apoptotic cell death (Chakraborty et al., 2015). In corroboration to these results, it was also shown that a CED-3 caspase activity gradient is formed in another neuroblast, called the QL.p neuroblast, which divides asymmetrically to form a smaller apoptotic daughter cell (Mishra et al., 2018). Taken together, these results show that CED-3 caspase is not only active in cells programmed to die, but also in their mothers. However, what is the role of active CED-3 in the mother cells, if not apoptosis?

To that end, the study by Mishra et al., 2018, found that *ced-3* is required for the mother cells to divide asymmetrically (Mishra et al., 2018). Specifically, they found that loss-of-function mutations in the pro-apoptotic genes *egl-1*, *ced-4* or *ced-3* led to the QL.p neuroblast dividing less asymmetrically than its wild-type counterpart. Furthermore, they also found that *ced-3* caspase activity is required for the asymmetric division of the QL.p neuroblast - a *ced-3* mutation, *n2433*, that disrupts the active site of CED-3 led to the QL.p neuroblast dividing less asymmetrically than wild-type animals (Mishra et al., 2018). In contrast to the QL.p neuroblast, loss-of-function of *ced-3* does not significantly affect the asymmetric division of the NSM neuroblast (NSMnb) (Figure 1.14, B) (Mishra et al., 2018). As mentioned previously, a linear pathway that we refer to as the *pig-1-nmy-2* axis, was shown to regulate the asymmetric division of the NSMnb (Wei et al., 2020). In *pig-1* loss-of-function animals, the NSMnb divides symmetrically to produce equally sized NSMsc and NSM daughter cells (Figure 1.14,

B) (Wei et al., 2020). Interestingly, animals homozygous for loss-of-function mutations of both, *pig-1* and *ced-3*, showed a reversed size asymmetry of the daughter cells, where the NSMsc was now larger than the NSM (Figure 1.14, B) (Mishra et al., 2018). These results suggest that *ced-3* is required to restrain the size of the NSMsc, when *pig-1* is absent. Taken together, *ced-3* has been shown to play a role in the asymmetric division of two mother cells. Specifically, in the NSMnb, *ced-3* acts together with the *pig-1-nmy-2* axis to promote asymmetric cell division. However, the mechanism by which *ced-3* regulates the asymmetric division of the NSM neuroblast and thereby a smaller size of the NSMsc remains unexplored.

The aim of this study was, therefore, to explore how *ced-3* promotes the formation of a smaller sized NSMsc that undergoes apoptotic cell death. Firstly, I provide biochemical evidence that CED-3 caspase physically interacts with actomyosin regulator ECT-2 RhoGEF *in vitro*. Subsequently, we used the NSM lineage to show that *ced-3* acts upstream of *ect-2* to promote the asymmetric division of the NSMnb and thereby a smaller NSMsc size. I also showed that ECT-2 is ventrally enriched in the NSM neuroblast, and this enrichment was *ced-3* caspase activity-dependent. Lastly, we showed that cell size and apoptosis are linked, where smaller cells are more prone to undergo apoptosis, whereas larger cells are more prone to survive.

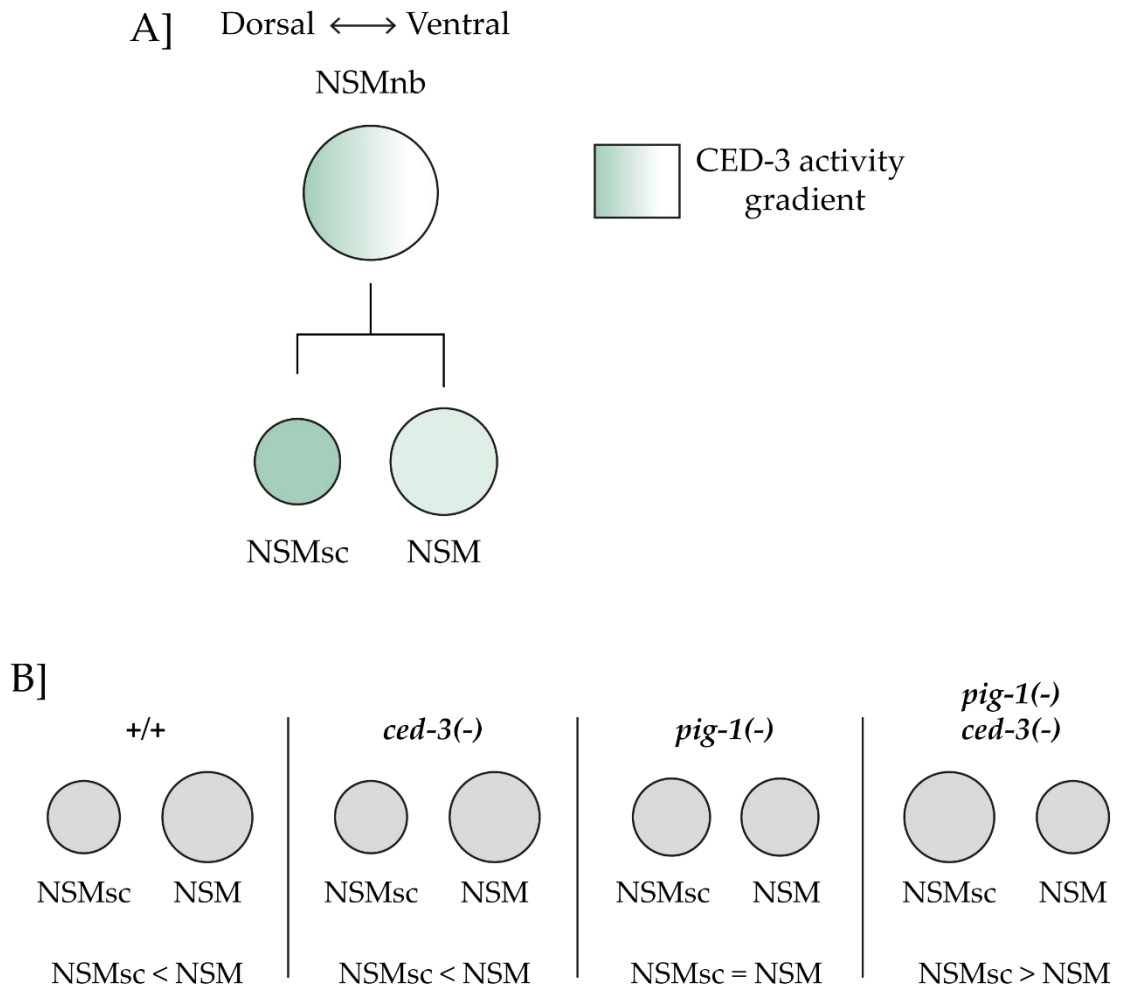


**Figure 1.14 Background of the study.** A] There is a dorsal to ventral CED-3 activity gradient in the NSMnb, where it has been shown that there is more CED-3 activity on the dorsal side of the NSMnb, which forms the smaller apoptotic daughter, the NSMsc. B] In wild-type ( $+/+$ ) and *ced-3* loss-of-function (*ced-3(-)*) animals, the NSMsc is smaller than the NSM. In *pig-1* loss-of-function (*pig-1(-)*) animals, the NSMsc and NSM are of similar sizes. In animals homozygous for both, *ced-3(-)* and *pig-1(-)*, the NSMsc is larger than the NSM.

2

# METHODOLOGY



## 2.1 Strains and general maintenance of *C. elegans*

All strains were maintained at 20°C in Nematode Growth Medium (NGM) plates as previously described, unless noted otherwise (Brenner, 1974). Animals carrying the *ced-4* mutation, *n3312*, were maintained at 15°C as it showed a cold-sensitive phenotype. All strains were fed with *E. coli* OP50 bacteria. Bristol N2 was used as the wild-type strain. The alleles (Table 1) and transgenes (Table 2) used in this study are given below:

**Table 1: Alleles used in this study**

| Allele        | Gene affected | Chromosome | Reference                  |
|---------------|---------------|------------|----------------------------|
| <i>cp13</i>   | <i>nmy-2</i>  | I          | (Wernike et al., 2016)     |
| <i>ax751</i>  | <i>ect-2</i>  | II         | (Zonies et al., 2010)      |
| <i>zh8</i>    | <i>ect-2</i>  | II         | (Canevascini et al., 2005) |
| <i>xs111</i>  | <i>ect-2</i>  | II         | (Zhang & Glotzer, 2015)    |
| <i>xs129</i>  | <i>ect-2</i>  | II         | (Zhang & Glotzer, 2015)    |
| <i>zh135</i>  | <i>ect-2</i>  | II         | Unpublished                |
| <i>e120</i>   | <i>unc-4</i>  | II         | (Brenner, 1974)            |
| <i>ok2283</i> | <i>strd-1</i> | III        | (Consortium, 2012)         |
| <i>it142</i>  | <i>nop-1</i>  | III        | (Tse et al., 2012)         |
| <i>n3312</i>  | <i>ced-4</i>  | III        | (Reddien et al., 2001)     |
| <i>n1162</i>  | <i>ced-4</i>  | III        | (Yuan & Horvitz, 1992)     |
| <i>n2427</i>  | <i>ced-3</i>  | IV         | (Shaham et al., 1999)      |
| <i>n2346</i>  | <i>ced-3</i>  | IV         | (Shaham et al., 1999)      |
| <i>n717</i>   | <i>ced-3</i>  | IV         | (Ellis & Horvitz, 1986)    |
| <i>n2433</i>  | <i>ced-3</i>  | IV         | (Shaham et al., 1999)      |
| <i>gm344</i>  | <i>pig-1</i>  | IV         | (Cordes et al., 2006)      |
| <i>n3331</i>  | <i>egl-1</i>  | V          | (Galvin et al., 2011)      |
| <i>n3330</i>  | <i>egl-1</i>  | V          | (Sherrard et al., 2017)    |

**Table 2: Transgenes used in this study**

| Transgene      | Sequence                           | Chromosome | Reference                  |
|----------------|------------------------------------|------------|----------------------------|
| <i>bcIs66</i>  | $P_{tph-1his-24}::gfp$             | III        | (Yan et al., 2013)         |
| <i>ltIs44</i>  | $P_{pie-1mCherry}::PH^{PLC\Delta}$ | V          | (Audhya et al., 2005)      |
| <i>bcIs65</i>  | $P_{tph-1his-24}::gfp$             | X          | (Yan et al., 2013)         |
| <i>bcIs109</i> | $P_{ced-3}::ced-3::gfp$            | Unknown    | (Chakraborty et al., 2015) |
| <i>ddIs86</i>  | $P_{pie-1}::LifeAct::gfp, unc-119$ | Unknown    | (Redemann et al., 2010)    |

## 2.2 Plasmid construction

---

### **pBC1922 (GST::proCED-3)**

This plasmid was generated using Gibson Assembly (Gibson et al., 2009). *ced-3* coding sequence was amplified from the plasmid pBC1819 (made by Hai Wei), and the primers were designed such that they contained overlapping sequences with the insert vector pGEX-4T1. The primer sequences used were:

5'-tggttccgcgtggatccccgATGCGTCAAGATAGAAGG -3' (overlap in lowercase)

5'-tcgagtcgaccgggaattcTTAGACGGCAGAGTTTCG-3' (overlap in lowercase)

The vector pGEX-4T1 was linearized using the following primer sequences:

5'-GAATTCCTCCGGGTCGACTC-3'

5'-CGGGGATCCACGCGGAAC-3'

The amplified insert and vector were assembled using Gibson Assembly Master Mix (New England Biolabs, E2611).

### **pBC1923 (GST::proCED-3(C358S))**

This plasmid was generated using Gibson Assembly (Gibson et al., 2009). *ced-3* coding sequence harbouring the G1073C mutation was amplified from the plasmid pBC1820 (made by H. Wei), and the primers were designed such that they contained overlapping sequences with the insert vector pGEX-4T1. The primer sequences used were:

5'-tggttccgcgtggatccccgATGCGTCAAGATAGAAGG -3' (overlap in lowercase)

5'-tcgagtcgaccgggaattcTTAGACGGCAGAGTTTCG-3' (overlap in lowercase)

The vector pGEX-4T1 was linearized using the following primer sequences:

5'-GAATTCCTCCGGGTCGACTC-3'

5'-CGGGGATCCACGCGGAAC-3'

The amplified insert and vector were assembled using Gibson Assembly Master Mix (New England Biolabs, E2611).

### **pBC1924 (GST::CED-3)**

The *ced-3* cDNA without the Pro-domain (CED-3) was amplified from a cDNA library of the N2 Bristol strain and cloned into the EcoRV site of pBluescript KS II(+) vector to generate the plasmid pBC1925. The sequence of the primers used to amplify CED-3 was as follows:

5'-GAATTCGTCGATGCACCAACCATAAG-3'

5'-CCCGGGTTAGACGGCAGAGTTTCGTG-3'

Subsequently, the CED-3 fragment was digested with EcoRI and subcloned into the pGEX-4T1 vector between the EcoRI site to generate the plasmid pBC1924.

### **pBC1926 (S::ECT-2)**

First, *ect-2* cDNA was amplified from a cDNA library of the N2 Bristol strain and cloned into the EcoRV site of pBluescript KS II(+) vector to generate the plasmid ECT-2::pBS. The sequence of the primers used to amplify *ect-2* cDNA (harbouring NcoI and AvaI sites) was as follows:

5'-ccatggACGTCTCAATGTTGC-3' (NcoI site in lowercase)

5'-ctcgagTCAGATATCGGTGACACG-3' (AvaI site in lowercase)

Subsequently, the *ect-2* cDNA fragment from ECT-2::pBS was digested using NcoI and AvaI and sub-cloned between the NcoI-AvaI site in the vector pCITE-4a(+) to generate the plasmid pBC1926.

### **pBC1951 (S::ECT-2::ΔBRCT)**

The fragment of the *ect-2* cDNA that lacked the BRCT domains was amplified from the plasmid containing full-length *ect-2* cDNA (pBC1926) (this study) using the following primer sequences:

5'-GTTTTCTGTGAAGTTTGCCAGTTGGTGGTTCGGGCAGCTCGCAACGTC-3'

5'-CCAACTGGCAAACCTTCACAGAAAACCAC-3'

The amplicon was subsequently transformed in chemically-competent bacteria, which enabled the ligation of the amplicon to produce the plasmid.

#### **pBC1952 (S::ECT-2::ΔDH)**

The fragment of the *ect-2* cDNA that lacked the DH domain was amplified from pBC1926 using the following primer sequences:

5'-TGAAGTTGTCATTCTTTTCACGCGATGGTTGACGTGGCGATTTGCAC-3'

5'-CGTGAAAAGAATGACAACCTTCATTTCCC-3'

The amplicon was subsequently transformed in chemically-competent bacteria, which enabled the ligation of the amplicon to produce the plasmid.

#### **pBC1953 (S::ECT-2::ΔPH)**

The fragment of the *ect-2* cDNA that lacked the PH domain was amplified from pBC1926 using the following primer sequences:

5'-AGAAGAATCTCCCACAATCACTGGAAATGAAGTTGTCATTCTTTTCA-3'

5'-AGTGATTGTGGGAGATTCTTCTACT-3'

The amplicon was subsequently transformed in chemically-competent bacteria, which enabled the ligation of the amplicon to produce the plasmid.

#### **pBC1964 (S::BRCT)**

This plasmid was generated using Gibson Assembly (Gibson et al., 2009). The fragment of the *ect-2* cDNA encoding the BRCT domain of ECT-2 (339bp-879bp) was amplified from pBC1926 and contained overlapping sequences with the vector pCITE-4a(+). The primer sequences used for the BRCT fragment were as follows:

5'-catggacagcTCCGTGTTGAAAAATAAGCTAC-3' (overlap in lowercase)

5'-tttttgagcgACTGCTTTCCAGTGGTTTTTC-3' (overlap in lowercase)

The vector pCITE-4a(+) was also amplified such that it contained overlapping sequences with BRCT fragment. The primer sequences were as follows:

5'-ggaaagcagTCGCTCAAAAACATCTTCATATCGTGTC-3' (overlap in lowercase)

5'-tcaacacggaGCTGTCCATGTGCTGGCG-3' (overlap in lowercase)

The amplified insert and vector were assembled using Gibson Assembly Master Mix (New England Biolabs, E2611).

### **pBC1965 (S::DH)**

This plasmid was generated using Gibson Assembly (Gibson et al., 2009). The fragment of the *ect-2* cDNA encoding the DH domain of ECT-2 (1086bp-1683bp) was amplified from pBC1926 and contained overlapping sequences with the vector pCITE-4a(+). The primer sequences used for the DH fragment were as follows:

5'-catggacagcGGACCAACTTCGTTGAAC-3' (overlap in lowercase)

5'-tttttgagcgcGTCATTCTTTTCACGAGTTTTG-3' (overlap in lowercase)

The vector pCITE-4a(+) was also amplified such that it contained overlapping sequences with DH fragment. The primer sequences were as follows:

5'-aaagaatgacCGCTCAAAAACATCTTCATATCGTGTC-3' (overlap in lowercase)

5'-aagttggtccGCTGTCCATGTGCTGGCG-3' (overlap in lowercase)

The amplified insert and vector were assembled using Gibson Assembly Master Mix (New England Biolabs, E2611).

### **pBC1966 (S::PH)**

This plasmid was generated using Gibson Assembly (Gibson et al., 2009). The fragment of the *ect-2* cDNA encoding the PH domain of ECT-2 (1710bp-2202bp) was amplified from pBC1926 and contained overlapping sequences with the vector pCITE-4a(+). The primer sequences used for the PH fragment were as follows:

5'-catggacagCAACTTCATTTCCCATCTG-3' (overlap in lowercase)

5'-tttttgagcgcCATCGCATCGTTGATCTC-3' (overlap in lowercase)

The vector pCITE-4a(+) was also amplified such that it contained overlapping sequences with PH fragment. The primer sequences were as follows:

5'-cgatgcatgCGCTCAAAAACATCTTCATATCGTGTC-3' (overlap in lowercase)

5'-aatgaagttGCTGTCCATGTGCTGGCG-3' (overlap in lowercase)

The amplified insert and vector were assembled using Gibson Assembly Master Mix (New England Biolabs, E2611).

**pBC1819 (proCED-3)** was constructed by H. Wei. Briefly, full-length *ced-3* cDNA was amplified from a cDNA library of the N2 Bristol strain and cloned into the *Sma*I site of the pBluescript II KS+ vector.

**pBC1820 (proCED-3(C358S))** was constructed by H. Wei. Briefly, the G1073C point mutation was introduced into the *ced-3* cDNA through one-site mutagenesis using plasmid pBC1819 as a template.

**pBC577 (S::CED-9)** was constructed by Stephane Rolland. Full-length *ced-9* cDNA was cloned into the pCITE-4a(+) vector between the *Nco*I and *Eco*RI site (Rolland et al., 2009).

**pET-CED-3 (proCED-3::FLAG)** was obtained as a gift from the lab of H.R. Horvitz, Massachusetts of Technology (Xue et al., 1996).

## 2.3 Expression of recombinant proteins

---

### 2.3.1 Expression of recombinant GST-tagged proteins for the pull-down assay

Protease-deficient BL21 (DE3) bacteria were transformed using standard heat-shock protocol with the GST-only pGEX-4T1 plasmid or the GST-tagged recombinant *ced-3* plasmids - pBC1922, pBC1923 and pBC1924. The transformed bacteria were cultured at 37°C in LB medium containing 100µg/ml carbenicillin until the OD<sub>600</sub> had reached 0.6. Subsequently, protein expression was induced with 0.5 mM IPTG for 4 hours at 37°C. Next, 25ml of cells were pelleted by centrifugation and the supernatant was discarded. Pellets were stored at -80°C for later use.

### 2.3.2 Expression of recombinant FLAG-tagged proteins for the cleavage assay

Protease-deficient BL21 (DE3) bacteria were transformed using standard heat-shock protocol with pET-CED-3 (proCED-3::FLAG) or pET-3a plasmids. The transformed bacteria were grown at 37°C in LB medium containing 100µg/ml carbenicillin until the OD<sub>600</sub> had reached 0.6. Subsequently, protein expression was induced with 1 mM IPTG for 2 hours at 25°C. Next, 50ml of cells were pelleted by centrifugation and the supernatant was discarded. The pellets were stored at -80°C for later use.

### 2.3.3 Expression of recombinant S-tagged proteins for the pull-down and cleavage assays

Protein expression of pBC577, pBC1926, pBC1951, pBC1952, pBC1953, pBC1964, pBC1965 and pBC1966 plasmids was performed in the presence of <sup>35</sup>S-methionine using the TNT T7 Quick Coupled Transcription/Translation System (Promega) according to the manufacturer's instructions (Cat. No. L1170) (total volume of 50µl). The reaction mixture containing the expressed proteins was used immediately for the pull-down assay or cleavage assay.



## 2.4 GST pull-down assay

---

### 2.4.1 Purification of recombinant GST-tagged proteins

The frozen protein pellets (GST-only, GST::proCED-3, GST::proCED-3(C358S) and GST::CED-3) were allowed to thaw on ice for 30 minutes and were then re-suspended in 2ml of CED-3 extraction buffer (50mM Tris-HCl pH 8.0, 0.5mM sucrose and 5% glycerol, cocktail of protease inhibitors). The mixture was sonicated (6 pulses of 10 seconds each with a 30 second interval at 20% amplitude using QSonica Q700) to lyse the bacterial cells and release the recombinant proteins. The bacterial debris was collected by centrifugation at 15,000g for 15 minutes at 4°C. The released GST-tagged proteins in the supernatant were purified using Glutathione-Sepharose beads (GE Healthcare) as described next. 1 mL of supernatant was incubated with 0.1 mL beads for 90 minutes at 4°C while continuously rotating on a bench-top tube rotator. Next, the mixture was centrifuged at 500g for 3 minutes at 4°C to pellet the beads. The supernatant was discarded. Next, the beads containing the bound GST-tagged proteins were washed with 1 mL CED-3 extraction buffer to remove unbound proteins. The wash was repeated thrice to ensure thorough removal of unbound proteins. The resultant bead mixture (0.1 mL) contained purified GST-tagged proteins. 0.1mL of binding buffer (30mM Tris-HCl pH 7.5, 0.5% Triton X-100, 100mM NaCl, 2mM MgCl<sub>2</sub>, 1mM DTT, 0.5% BSA and a cocktail of protease inhibitors) was added to the purified bead mixture to make a "1:1 slurry", which was used for the pull-down assay.

### 2.4.2 The pull-down assay

50µl of 1:1 slurry mixture was incubated with 10µl of *in vitro* transcribed-translated S-tagged proteins in the presence of 500µl of binding buffer (30mM Tris-HCl pH 7.5, 0.5% Triton X-100, 100mM NaCl, 2mM MgCl<sub>2</sub>, 1mM DTT, 0.5% BSA and a cocktail of protease inhibitors) for 90 minutes at 4°C while continuously shaking. The mixture

was washed with 1mL of BSA-free binding buffer (30mM Tris-HCl pH 7.5, 0.5% Triton X-100, 100mM NaCl, 2mM MgCl<sub>2</sub>, 1mM DTT and a cocktail of protease inhibitors) to remove unbound protein and centrifuged for 10-15 seconds on a bench-top centrifuge. The supernatant was discarded. The wash was repeated thrice. Finally, the reaction was stopped by adding 50µl of 2x LDS sample buffer (containing 5% β-mercaptoethanol) and heated to 70°C for 10 minutes. All experiments were performed at least in triplicates.

## 2.5 Cleavage assay

---

The frozen proCED-3::FLAG pellet was thawed on ice for 30 minutes and then re-suspended in 0.4ml of CED-3 extraction buffer (50mM Tris-HCl pH 8.0, 0.5mM sucrose and 5% glycerol). The mixture was sonicated (3 pulses of 5 seconds each with a 15 second interval at 20% amplitude using QSonica Q700) to lyse the bacterial cells and release the recombinant proteins. The bacterial debris was collected by centrifugation at 13,000g for 10 minutes at 4°C and the resulting supernatant was used as 'CED-3 lysate' for the *in vitro* cleavage assays. 3µl of CED-3 lysate was incubated with 3µl of *in vitro* transcribed-translated proteins and 4µl of CED-3 extraction buffer (total reaction volume of 10µl) at 30°C for 90 minutes. The pET-3a lysate was used as a negative control. The reaction was stopped by adding 10µl of 2x LDS sample buffer (containing 5% β-mercaptoethanol) and heated to 70°C for 10 minutes. All experiments were performed at least in triplicates.

## 2.6 Analysis of GST pull-down and cleavage assay

---

Post-termination of the assay reactions using sample buffer, the reaction mixtures were run on a 10% Bis-TRIS gel (NuPAGE™) using MOPS running buffer containing 0.1% SDS. The gels with the pull-down assay mixtures were stained with Coomassie staining solution (20% methanol, 10% acetic acid and 0.1% Coomassie Brilliant Blue) followed by de-staining with de-staining solution (50% methanol and 10% acetic acid) until distinct bands were visible. The gels with the cleavage assay mixtures were not Coomassie stained. Subsequently, all gels were fixed using fixative (50% ethanol, 10% acetic acid), dried on a slab gel dryer at 80°C and exposed on either a photostimulable phosphor (PSP) plate or an X-ray film for detection of the <sup>35</sup>S-labelled proteins. Exposed films were developed using a phosphor imager or X-ray film developer (PROTEC) to visualize radioactively-labelled proteins.

## 2.7 Calculating NSMsc survival percentage

---

To determine the percentage of surviving NSMsc, the  $P_{tph-1his-24}::gfp$  (*bcIs66* or *bcIs65*) transgene was used, which labels serotonergic neurons (Yan et al., 2013). L3 or L4 larvae were mounted on 2% agarose pads containing ~20 $\mu$ l of 25mM sodium azide in M9 buffer on a standard microscopy slide. The number of GFP-positive cells were counted in the lower half of the anterior pharynx using a Leica Imager.M2 or Zeiss Axioscope 2 in a 63x oil immersion objective. Wild-type worms contain two GFP-positive cells representing the two NSM neurons in the anterior pharynx. Up to two extra GFP-positive cells can be seen in mutants, representing inappropriately surviving NSMsc. The NSMsc survival percentage represents the number of NSMsc that inappropriately survived divided by the maximum number of NSMsc that could have survived.

## 2.8 Confocal and super-resolution microscopy

---

Confocal imaging was performed using a Leica TCS SP5 or SP8 microscope. The samples were imaged using a 63x oil immersion objective. For red fluorescent proteins, the excitation wavelength was set at 561nm and the emitted light was collected between 567-662nm using a HyD detector. For green fluorescent proteins, the excitation wavelength was set at 476nm or 488nm and the emitted light was collected between 500-550nm using a PMT detector. The excitation laser power varied between different fluorescent proteins but was kept constant throughout the experiments.

Super-resolution imaging was performed using a Zeiss LSM 980 with AiryScan2 detector. The samples were imaged using a 63x oil immersion objective. For red fluorescent proteins, the excitation wavelength was set at 561nm. For green fluorescent proteins, the excitation wavelength was set at 488nm.

## 2.9 Determining daughter cell size ratio (NSMsc:NSM)

---

### 2.9.1 Mounting embryos and selecting the NSM neuroblast

To mount embryos for microscopy, 10-20 gravid adults were dissected in deionized water to release mixed-stage embryos. The embryos were transferred to a 2% agarose pad on a standard microscopy slide using a mouth pipette with deionized water. Next, an 18mm x 18mm #1.5 coverslip (~0.17mm thickness) was gently placed on top of the embryos in water in the 2% agarose pad. The coverslip was sealed with white petroleum jelly to prevent drying-out of the embryos. The microscopy slide was incubated at 25°C until some of the embryos reached comma-stage (~2-3 hours). At the confocal microscope, comma-stage embryos were identified on the agarose pad using transmitted light. Once an appropriate embryo was selected, the NSM neuroblast was identified using the cell boundary marker  $P_{pie-1mCherry::PH^{PLC\Delta}}$  (*ItIs44*) based on its shape and position. Furthermore, a NSM neuroblast that was at metaphase was chosen for imaging (metaphase neuroblasts appear completely spherical). A 5-10 minute time-series Z-stack (0.5µm step size) recording of the metaphase NSM neuroblast from top to bottom was set-up. Excitation wavelength of 561 nm at 14% laser power was used and the emitted light was collected between 567-662 nm using a HyD detector. The NSM neuroblast at metaphase undergoes cytokinesis in ~1 minute to generate the two unequally sized daughter cells (NSMsc and NSM).

### 2.9.2 Calculating the NSMsc:NSM daughter cell size ratio

The cell sizes of the NSMsc and NSM were calculated using the cell boundary marker  $P_{pie-1mCherry::PH^{PLC\Delta}}$  (*ItIs44*). Since the NSM neuroblast and its division was recorded, the time-point immediately post-division was chosen to calculate the sizes of the two daughter cells. Fiji (ImageJ) software was used for analysis. For both daughter cells, a region of interest (ROI) was drawn around the boundary of the cell at each Z-slice.

The area of the ROI at each Z-slice was determined using the “measure” function on Fiji. Subsequently, the size (volume) of the daughter cell was estimated by summing up the area of each Z-slice. Finally, the size of the NSMsc was divided by the size of the NSM to obtain the “daughter cell size ratio”.



## 2.10 Visualization and quantification of ECT-2::GFP, NMY-2::GFP, LifeAct::GFP, CED-3::GFP and mCherry::PH<sup>PLCA</sup> in the NSM neuroblast

---

### 2.10.1 Visualization of the transgenes using confocal microscopy

The CRISPR knock-in allele *zh135* (*ect-2::gfp*) generated in the Hajnal lab (unpublished) was used to visualize ECT-2. The CRISPR knock-in allele *cp13* (*nmy-2::gfp+LoxP*) was used to visualize NMY-2. The transgene *ddl86* (*Ppie-1::LifeAct::gfp, unc-119*) was used to visualize F-actin. The transgene *bcl86* (*Pced-3::ced-3::gfp*) was used to visualize total CED-3. The transgene *lts44* (*Ppie-1mCherry::PH<sup>PLCA</sup>*) was used to label cell boundaries to identify the NSM neuroblast. All strains analysed were homozygous for the transgenes. The visualization of the transgenes was performed using confocal microscopy. The excitation wavelength and laser power used for the different transgenes is summarized below (table 3).

**Table 3: Confocal laser power for the various transgenes**

| Transgene reporter                          | Excitation wavelength | Laser power |
|---|-----------------------|-------------|
| <i>zh135</i> (ECT-2::GFP)                   | 476nm                 | 60%         |
| <i>cp13</i> (NMY-2::GFP)                    | 488nm                 | 20%         |
| <i>ddl86</i> (LifeAct::GFP)                 | 488nm                 | 20%         |
| <i>bcl86</i> (CED-3::GFP)                   | 488nm                 | 20%         |
| <i>lts44</i> (mCherry::PH <sup>PLCA</sup> ) | 561nm                 | 14%         |

The mounting and selection of embryos was performed similar to Section 2.9.1. Instead of selecting perfectly spherical NSM neuroblasts, slight elliptical shaped NSM neuroblasts were selected because we wanted to visualize protein localization ~5 minutes before metaphase. A 10-15 minutes time-series Z-stack (0.5µm step size) recording of the NSM neuroblast from top to bottom was set-up.

### **2.10.2 Quantification of fluorescence signal to obtain a 'ventral:dorsal fluorescence ratio'**

Using the cell boundary marker, the central Z-slice of the NSM neuroblast was identified. All quantifications were performed on the central Z-slice. For quantification, the NSM neuroblast was divided into dorsal and ventral halves by drawing a vertical line in the centre of the neuroblast and a region of interest (ROI) for the two halves was saved on Fiji (ImageJ). Next, the mean grey value of the two saved ROI halves was measured in the GFP channel (*zh135* or *cp13* or *ddl86*) or mCherry channel (*lIs44*) on Fiji (ImageJ). The 'ventral/dorsal fluorescence ratio' was determined by dividing the ventral mean grey value by the dorsal mean grey value. This was repeated for the two different timepoints, which were 5 minutes before metaphase ( $t_{-5min}$ ) and at metaphase ( $t_{0min}$ ). The metaphase timepoint ( $t_{0min}$ ) was defined as the timepoint just before the NSM neuroblast undergoes cell division as the division was tracked live. Background subtraction was performed by drawing a 20x20 pixel ROI square in a random background area of the embryo, measuring the mean grey value of this square and subsequently subtracting this mean grey value from the central Z-slice used for quantification.

### **2.10.3 Investigating dynamics of ECT-2::GFP using super-resolution microscopy**

As mentioned in the previous section, ECT-2::GFP fluorescence was quantified at two time-points - 5 minutes before metaphase ( $t_{-5min}$ ) and at metaphase ( $t_{0min}$ ). The metaphase timepoint ( $t_{0min}$ ). However, we also wanted to analyse the ECT-2::GFP localization 10 minutes before metaphase ( $t_{-10min}$ ). As confocal microscopy showed bleaching issues for longer time-series recordings, we switched to super-resolution microscopy using LSM 980 with AiryScan 2. Embryos were mounted and selected similar to Section 2.10.1. The only difference was that the time-series recording was set-up for 20-30 minutes. 488 nm was used as the excitation wavelength, with 1% laser power. Quantification of fluorescence signal and calculation of ventral:dorsal fluorescence ratio was performed similar to section 2.10.2.

## 2.11 Calculating metaphase circularity

---

The circularity of the NSM neuroblast at metaphase was calculated using the cell boundary marker  $P_{pie-1mCherry::PH^{PLC\Delta}}$  (*ltIs44*). The mounting and selection of embryos was performed similar to Section 2.9.1. The metaphase timepoint was defined as the timepoint just before the NSM neuroblast undergoes cell division as the division was tracked live. A region of interest was drawn on the boundary of the central Z-slice of the cell. The area (A) and perimeter (P) of the cell was determined using ImageJ (Fiji) and the circularity of the cell was calculated using the formula  $4\pi(A/P^2)$ .

## 2.12 Statistical analyses

---

Statistical analyses were performed using Prism by GraphPad. Normal distribution of the data was tested using the D'Agostino and Pearson test. If the data showed normal distribution, a two sample t-test was performed to compare two independent groups (Welch's t-test). For comparison of multiple groups showing normal distribution, a one-way ANOVA was used with multiple comparison correction using Dunnett's T3 multiple comparison test. For the NSMsc survival percentages, statistical analyses was performed as a 2x2 contingency table using Fisher's exact test.

**3**

# **RESULTS**

## **Preface**

The results presented in section 3.1.1 (Yeast two-hybrid screen) were the combined effort of H. Wei and N. Mishra, in collaboration with Next Interactions Inc. (<https://nextinteractions.com/>).

The results presented in section 3.2 and 3.3 were the combined efforts of H. Wei and me.

The results presented below have been published on 06<sup>th</sup> October 2022 as:

Sethi A, Wei H, Mishra N, Segos I, Lambie EJ, Zanin E, Conradt B. A caspase-RhoGEF axis contributes to the cell size threshold for apoptotic death in developing *Caenorhabditis elegans*. PLoS Biol. 2022 Oct 6;20(10):e3001786. doi: 10.1371/journal.pbio.3001786. PMID: 36201522; PMCID: PMC9536578.

### 3.1 CED-3 caspase physically and directly interacts with ECT-2 RhoGEF *in vitro*

---

#### 3.1.1 A next-generation Yeast two-hybrid screen identified the candidate physical interactors of CED-3

The major aim of the project was to uncover the mechanism by which the proapoptotic gene *ced-3* caspase promotes the asymmetric division of the NSM neuroblast, and thereby a smaller NSMsc size. Therefore, a Yeast two-hybrid screen based on next generation sequencing was performed in collaboration with Next Interactions Inc. (<https://nextinteractions.com/>) to identify the candidate physical interactors of CED-3 protein. Two constructs of *ced-3* were used as the bait for the screen. The first construct was a wild-type full-length fragment of the *ced-3* cDNA, which is expected to lead to the production of a fully active CED-3 protein (proCED-3) (Figure 3.1). The proCED-3 construct is expected to fully mature into active CED-3 by auto-cleavage. The second construct was a full-length fragment of the *ced-3* cDNA that contained a missense point mutation, which would lead to the production of a catalytically inactive form of CED-3 protein (proCED-3(C358S)) (Figure 3.1). The proCED-3(C358S) construct is expected to remain as an inactive zymogen. The prey for the screen was a cDNA library generated from mRNA isolated from eight different stages of *C. elegans* development – 0 hour embryos, 4 hour embryos, 9 hour embryos, L1 larvae, L2 larvae, L3 larvae, L4 larvae and mixed-stage adults (Figure 3.1). Out of the 20094 annotated genes at that time, 12891 genes were selected as the prey by Next Interactions Inc. based on detectable transcripts found in the isolated mRNA. To identify the differentially enriched genes as candidate interactors of CED-3, the enrichment of the prey cDNA samples obtained from the Yeast two-hybrid screen were compared to two negative controls – a cDNA library control and an empty bait-vector control. Only the genes that showed a two-fold enrichment against both the controls were chosen as the true candidate interactors of CED-3. Using this

enrichment, 186 interactors of proCED-3 and 448 interactors of proCED-3(C358S) were identified.

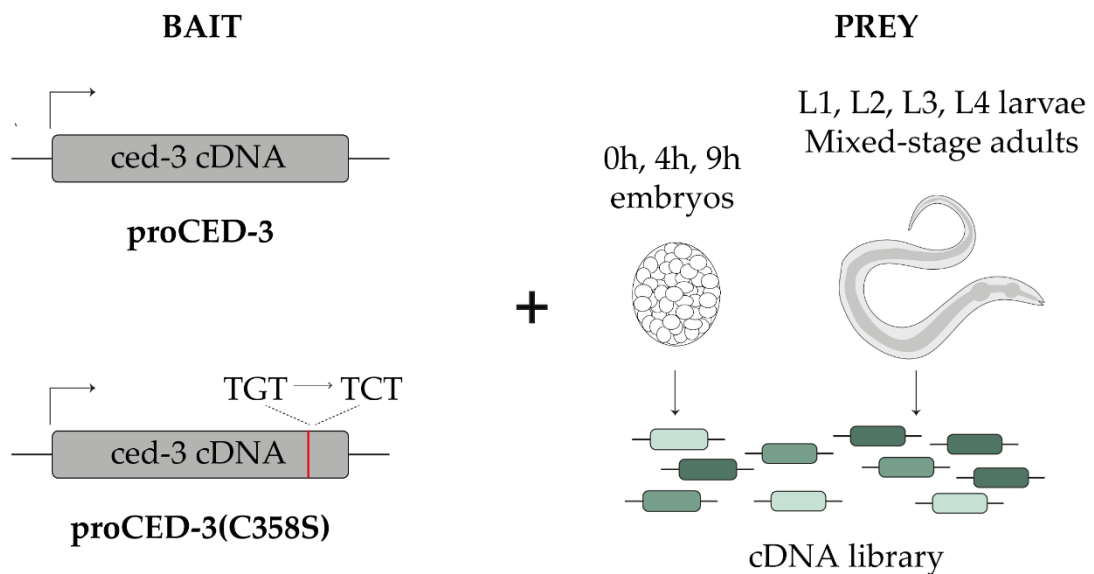


**Figure 3.1** The baits (left) and prey (right) used for the Yeast two-hybrid screen to identify candidate interactors of CED-3 caspase. Two baits were used for the screen – a full-length proCED-3 and a full-length proCED-3 harboring a point-mutation (G to C) that leads to the production of inactive proCED-3, where the cysteine in position 358 has been changed to serine. The prey for the screen was cDNA isolated from 0 hour, 4 hour, 9 hour embryos and L1, L2, L3, L4 larvae and mixed-stage adults.

### 3.1.2 Gene set enrichment analysis of physical interactors of CED-3 gives a hint into how CED-3 could promote a smaller daughter cell size

I aimed to investigate whether any gene category was over-represented in the list of candidate interactors of CED-3 obtained from the Yeast two-hybrid screen. This would give us insight into how *ced-3* could promote asymmetric division and smaller daughter cell size. To that end, I performed a gene set enrichment analysis of the list of interactors. The online WormCat tool was used to perform the gene set enrichment analysis (<http://www.wormcat.com/>) as it has been reported to use a better and near-complete annotation of the *C. elegans* genome as compared to other non-model organism specific gene ontology enrichment tools (Holdorf et al., 2020). The gene set enrichment analysis revealed that the interactors belonged to various groups of



biological processes (Figure 3.2). ‘Transcription factors’ and ‘metabolism’ were the over-represented gene groups for both, the interactors of proCED-3 as well as proCED-3(C358S). However, this did not give much insight into how *ced-3* could promote asymmetric division. The most interesting over-represented gene group was ‘cytoskeleton’ for the list of proCED-3(C358S) interactors (Figure 3.2). We found it interesting because it has been shown previously in *C. elegans* neuroblasts that asymmetric enrichment of myosin II, a component of the cytoskeletal actomyosin network, is required for its unequal division by size and thereby a smaller daughter cell (Figure 1.12) (Wei et al., 2020). Furthermore, in *Drosophila melanogaster* neuroblasts as well, temporal dynamics of myosin II is required for its unequal division by size (Figure 1.9) (Tsankova et al., 2017). Therefore, we hypothesized that *ced-3* could promote a smaller daughter cell size by acting via components of the actomyosin network and manually examined the list of interactors of proCED-3(C358S) for regulators and/or components of the actomyosin network.

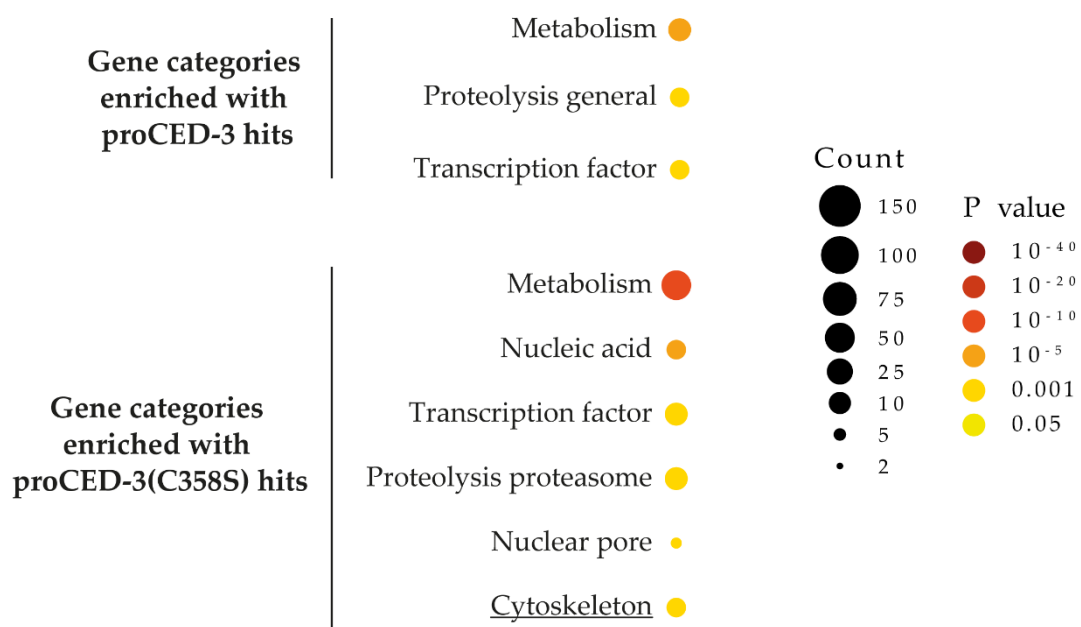


**Figure 3.2 Gene set enrichment analysis of interactors of proCED-3 and proCED-3(C358S) obtained from the Yeast two-hybrid screen.** The most interesting over-represented gene group was ‘cytoskeleton’ (underlined) for the list of proCED-3(C358S) interactors. Adapted from (Holdorf et al., 2020).

### 3.1.3 CED-3 physically interacts with ECT-2 *in vitro*

After manual examination of the list of 448 proCED-3(C358S) interactors obtained from the Yeast two-hybrid screen, we found *ect-2* to be the most promising interactor. *ect-2* is a Rho guanine-nucleotide exchange factor (RhoGEF) that can activate the kinase RHO-1 by exchanging the bound GDP with GTP. Activation of the RHO-1 pathway promotes the contractility of the actomyosin network (Figure 1.6) (Glotzer, 2005; Piekny et al., 2005). From previous studies in our lab, we know that the actomyosin network plays a role in promoting asymmetric division of the NSM neuroblast and smaller daughter NSMsc size (Wei et al., 2020). Therefore, we hypothesized that *ced-3* acts via *ect-2* and thereby the actomyosin network to promote asymmetric division of the NSM neuroblast.

Therefore, I aimed to confirm the physical interaction between CED-3 and ECT-2 obtained from the Yeast two-hybrid screen. To that end, I employed an *in vitro* Glutathione S-transferase (GST) pull-down assay. I constructed three baits of CED-3 protein tagged to GST on the N-terminus: a full-length wild-type construct (GST::proCED-3), a full-length construct that contained a missense point mutation, which would lead to the production of its catalytically inactive form (GST::proCED-3(C358S)) and a construct that contained only the large and small subunit i.e. p17 and p15 respectively (GST::CED-3) (Figure 3.3). These bait constructs were expressed in protease-deficient *E. coli* and the GST-tag enabled the purification of the recombinant proteins using glutathione coated Sepharose beads. Full-length ECT-2 was used as the prey, which was synthesized using an *in vitro* transcription/translation kit in the presence of <sup>35</sup>S-methionine and an S-tag at the N-terminus (S::ECT-2) (Figure 3.3). This enabled us to detect S::ECT-2 using autoradiography. From the pull-down assay, I observed that S::ECT-2 co-purifies with all three recombinant forms of CED-3 i.e. GST::proCED-3, GST::proCED-3(C358S) and GST::CED-3 (Figure 3.4, A). Furthermore, S::ECT-2 did not co-purify with the GST-only negative control. As another control, I also checked whether *in vitro* synthesized Luciferase co-purifies with

GST::proCED-3 and did not find co-purification of Luciferase (Figure 3.4, B). These results demonstrate that CED-3 physically and directly interacts with ECT-2 *in vitro*. Furthermore, these results also show that the Pro-domain of CED-3 is not necessary for its interaction with ECT-2 as ECT-2 also co-purified with the construct lacking the Pro-domain (GST::CED-3).

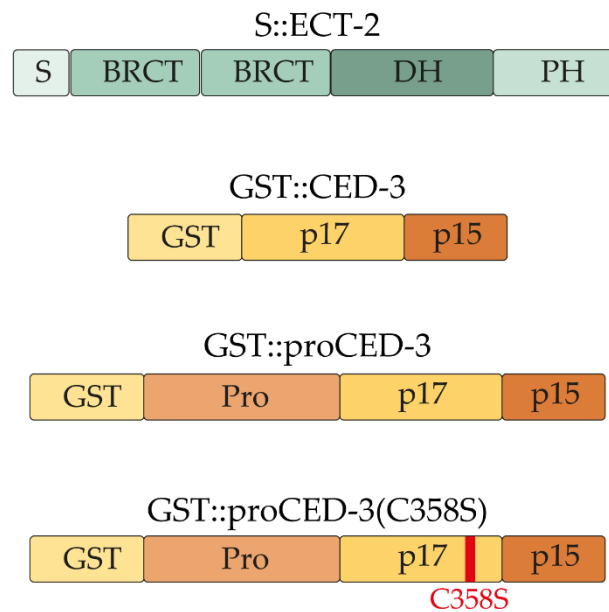


**Figure 3.3 Schematic of the constructs used for the pull-down assay.** ECT-2, which has four domains (2 BRCT domains, DH domain and PH domain) was tagged with a S-tag at the N-terminus. CED-3, proCED-3 and proCED-3(C358S) was tagged to GST at the N-terminus.

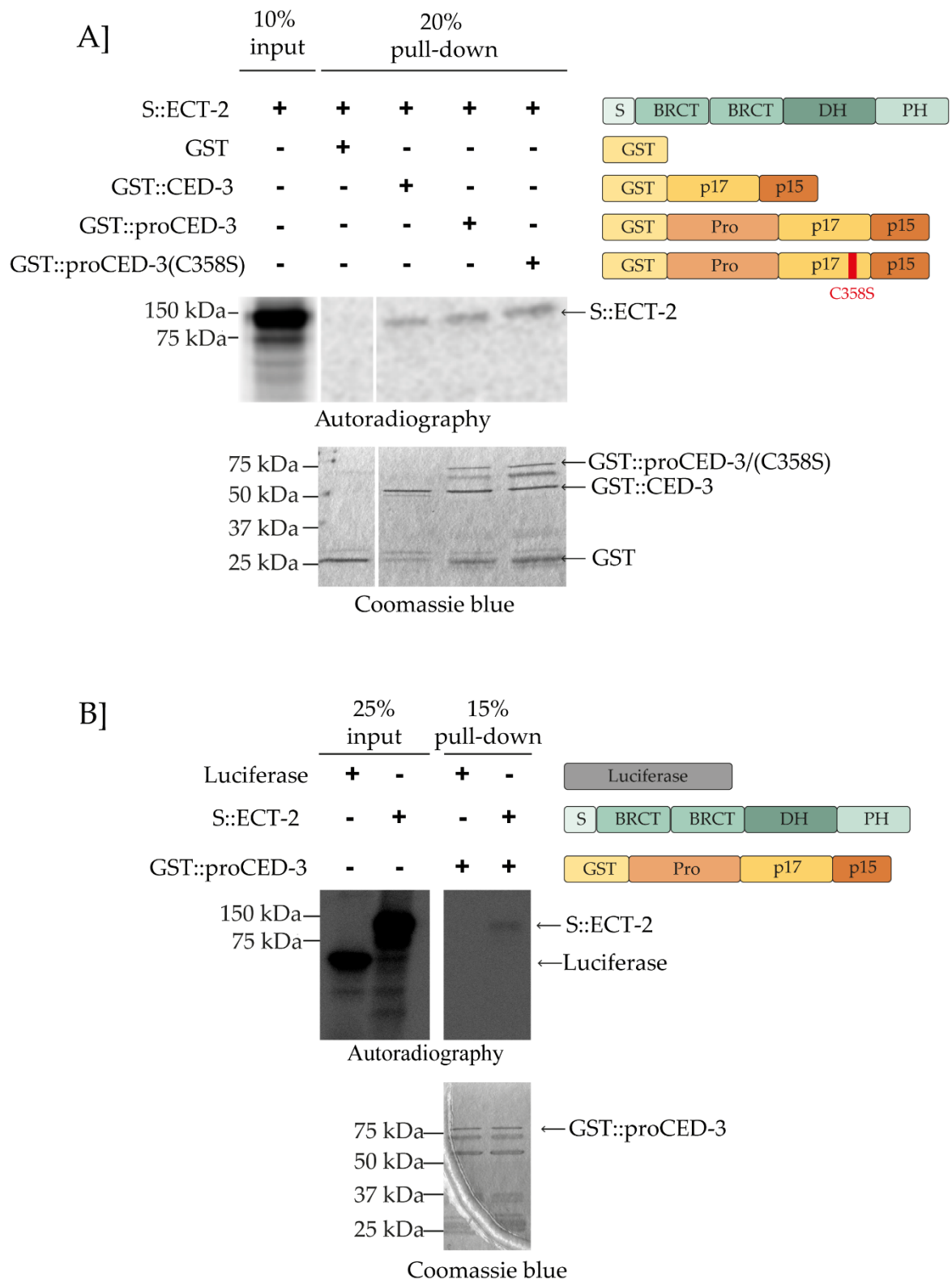


**Figure 3.4 Physical interaction between CED-3 and ECT-2 *in vitro*.** A, B] Autoradiographs and Coomassie blue-stained gels of representative GST pull-down experiments. The different lanes shown in the figure are from the same gel.

### 3.1.4 The Plekstrin Homology (PH) domain of ECT-2 is sufficient for its interaction with CED-3

To gain further insight into the relevance of the physical interaction between CED-3 and ECT-2, I aimed to determine which domain of ECT-2 interacts with CED-3 using the same pull-down strategy. ECT-2 protein has three functional domains (<http://www.uniprot.org/uniprot/Q9U364>) (Figure 3.3) – Two tandem N-terminal BRCA1-like domains (BRCT) most likely involved in its auto-inhibition (Schneid et al., 2021), a central Dbl-like homology (DH) domain responsible for its catalytic GEF activity and a C-terminal Plekstrin homology (PH) domain involved in its autoinhibition and localization to the lipid bilayer (Chan & Nance, 2013; Chen et al., 2020). Firstly, to uncover which of these domains is necessary for its interaction with CED-3, three deletion fragments of ECT-2 were constructed lacking either of the three domains – **S::ECT-2::ΔBRCT**, **S::ECT-2::ΔDH** and **S::ECT-2::ΔPH**. For the bait construct, the full-length wild-type fragment of CED-3 (**GST::proCED-3**) was used. I found that all three deletion constructs of ECT-2 co-purified with **GST::proCED-3** (Figure 3.5, A). I imagined that this could be due to the fact that more than one domain of ECT-2 is necessary for its interaction with CED-3. Subsequently, to find out which domain of ECT-2 is sufficient for its interaction with CED-3, I used each domain fragment as a prey (**S::BRCT**, **S::DH**, **S::PH**) and performed the pull-down assay with **GST::proCED-3**. I found that only the PH domain of ECT-2 (**S::PH**) co-purified with **GST::proCED-3** (Figure 3.5, B). This result suggests that CED-3 interacts with ECT-2 via its PH domain. The PH domain is known to bind to phosphatidylinositol lipids in the plasma membrane (Wang & Shaw, 1995). Additionally, recent structural studies of mammalian Ect2 revealed that the PH domain is also involved in Ect2 auto-inhibition (Chen et al., 2020). Therefore, we proposed that binding of CED-3 to the PH domain of ECT-2 could either alter ECT-2's ability to bind to the plasma membrane or relieve it of its auto-inhibition.

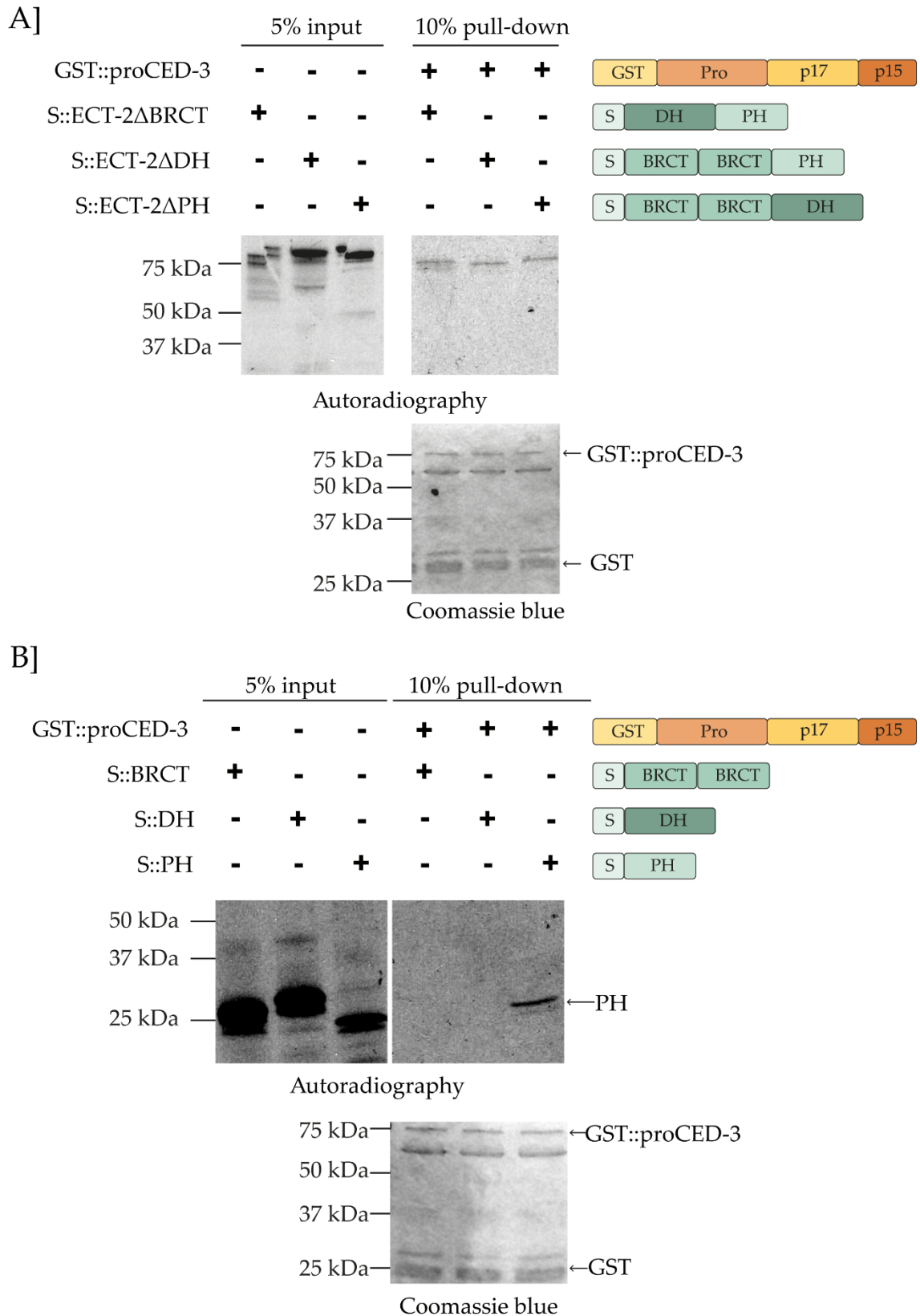


**Figure 3.5 Physical interaction between CED-3 and the PH domain *in vitro*.** A, B] Autoradiographs and Coomassie blue-stained gels of representative GST pull-down experiments. The different lanes shown in the figure are from the same gel.

### 3.1.5 CED-3 does not cleave ECT-2 *in vitro*

CED-3 is a caspase, which is a protease that can cleave its target proteins at aspartic acid residues (Nicholson, 1999). Since CED-3 physically interacts with ECT-2, I wanted to test whether CED-3 can also cleave ECT-2 *in vitro*. I examined the primary amino acid sequence of ECT-2 and found six potential caspase cleavage sites based on the CED-3 caspase consensus sequence DXXD (Figure 3.6, A) (Xue et al., 1996). I synthesized a full-length wild-type form of CED-3 tagged to a FLAG-tag at the C-terminus (**proCED-3::FLAG**) in protease-deficient *E. coli*. I tested whether the bacterial lysate containing proCED-3::FLAG (**CED-3 lysate**) could cleave ECT-2 *in vitro*. I used a bacterial lysate containing the empty vector pET3a as a negative control. We also used S-tagged CED-9 (**S::CED-9**) as a positive control for the cleavage assay as CED-3 has previously been shown to cleave CED-9 *in vitro* (Weaver et al., 2014). From the cleavage assay, I did not observe any noticeable difference in the cleavage pattern of S::ECT-2 when incubated with CED-3 lysate as compared to the empty vector lysate (Figure 3.6, C). Alternatively, S::CED-9 was found to be effectively cleaved by the CED-3 lysate (Figure 3.6, B). One of the caspase cleavage sites within the PH domain of ECT-2 was found to be fully conserved within the *Caenorhabditis* species (Figure 3.6, A). From the pull-down assay, we knew that the PH domain of ECT-2 physically interacts with CED-3. Therefore, I also employed the cleavage assay to test whether CED-3 lysate could cleave the PH domain (**S::PH**). However, I found no evidence of cleavage of the PH domain either (Figure 3.6, D). These results suggest that CED-3 does not cleave ECT-2 *in vitro*.

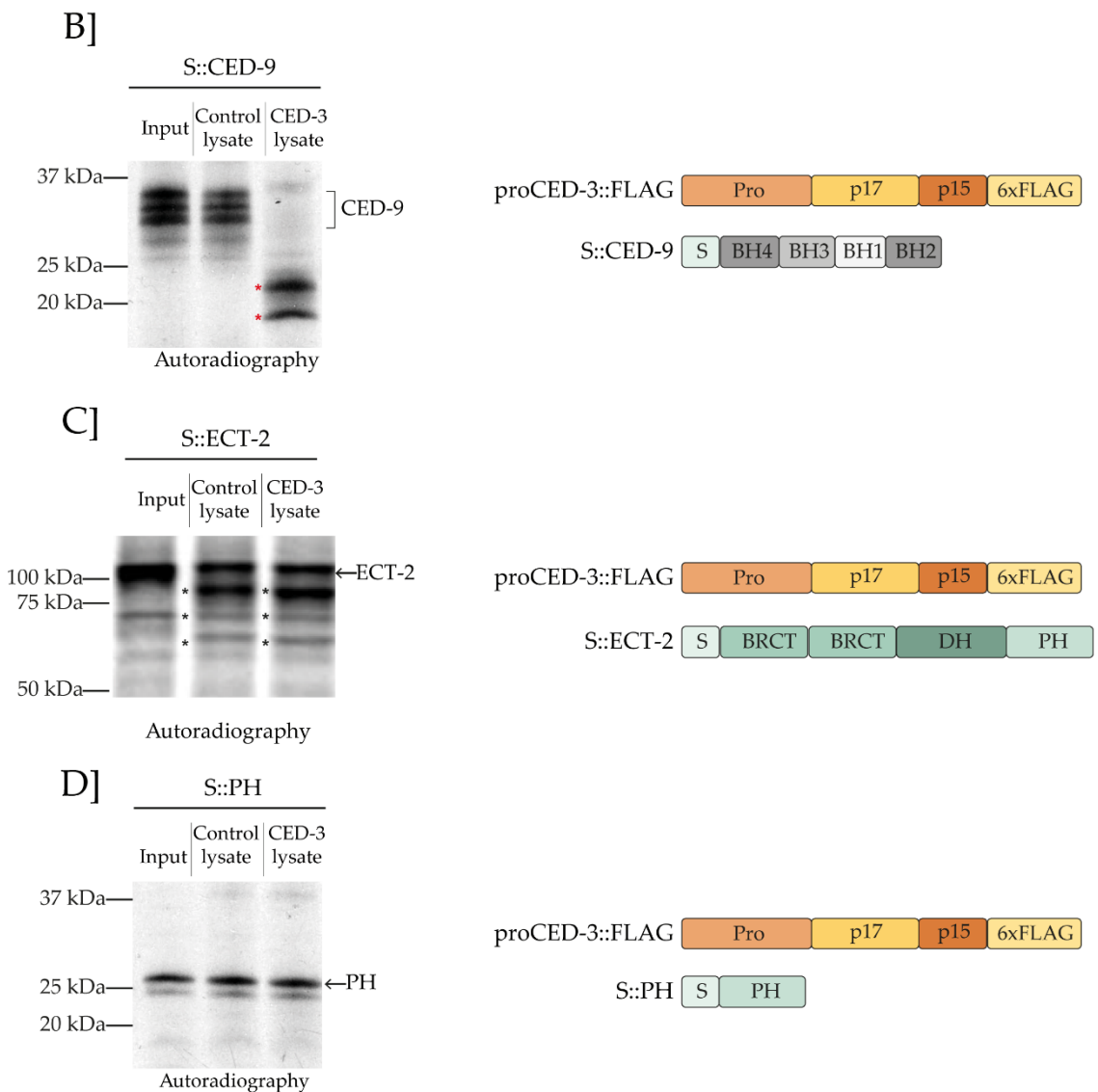
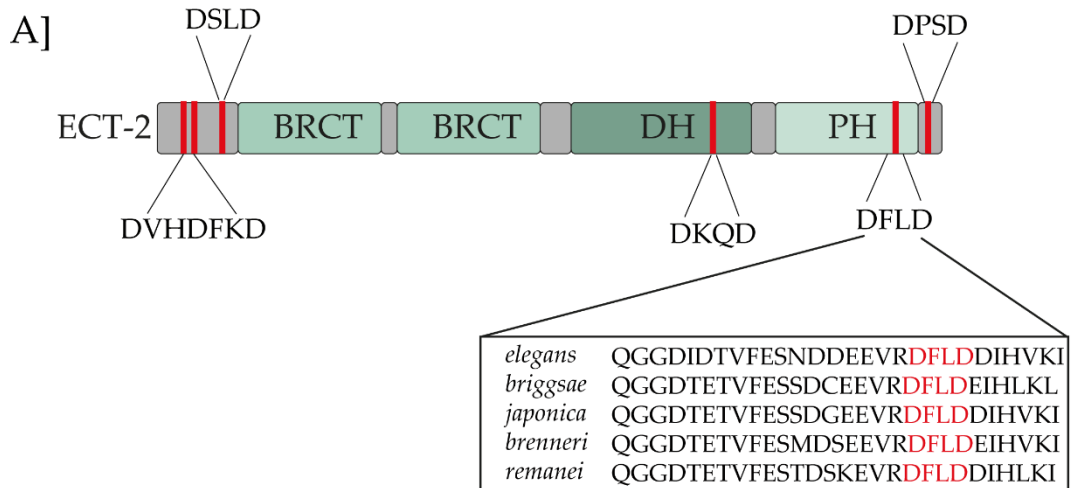




**Figure 3.6 Cleavage assay gels.** A] Schematic representation of ECT-2 and the predicted caspase cleavage sites (DxxD) shown using vertical red lines. The amino acid sequence of the cleavage site in the PH domain (DFLD) is conserved among the different *Caenorhabditis* species. B, C, D] Autoradiographs of representative cleavage assay gels between proCED-3::FLAG and S::CED-9, S::ECT-2 and S::PH respectively. The red asterisks in B indicate S::CED-9 cleavage products arising from incubation with CED-3 lysate. The black asterisks in in C indicate S::ECT-2 cleavage products arising from incubation with the bacterial lysate.

Overall, in result section 3.1, I utilized a biochemical approach to show that CED-3 physically interacts with the actomyosin regulator ECT-2 *in vitro*, specifically with its plasma membrane binding PH domain. Additionally, I also found that CED-3 does not cleave ECT-2 *in vitro*.

## 3.2 A *ced-3* caspase – *ect-2* RhoGEF axis promotes asymmetric division of the NSM neuroblast

---

In this section, we investigated the *in vivo* interaction between *ced-3* caspase and *ect-2* RhoGEF using the NSM lineage as a model. Specifically, I analyzed the localization of ECT-2, NMY-2 and F-actin in the NSM neuroblast in wild-type and *ced-3* mutant animals. Next, H. Wei and I dissected the genetic pathway, which we call the *ced-3-ect-2* axis, that promotes the asymmetric division of the NSM neuroblast and thereby the formation of a smaller NSMsc.

### 3.2.1 ECT-2 is ventrally enriched in the NSM neuroblast ~5 minutes before metaphase

Previous studies from our lab had proposed that asymmetric actomyosin contractility of the NSM neuroblast cortex is important for its unequal division by size, and thereby a smaller NSM sister cell (NSMsc) (Wei et al., 2020). Specifically, it was shown that non-muscle myosin II (NMY-2) is asymmetrically enriched in the ventral cortex of the NSM neuroblast ~5 minutes before metaphase. This asymmetric enrichment is required to generate a smaller NSM sister cell as elimination of NMY-2 asymmetry led to the formation of two-equally sized daughter cells. *ect-2* is also known to promote actomyosin contractility in single-celled *C. elegans* embryos (Cowan & Hyman, 2007) and from our biochemical studies, we hypothesized that *ced-3* acts via *ect-2* and thereby via the actomyosin network to promote asymmetric division of the NSM neuroblast. Therefore, I visualized the localization of ECT-2 in the NSM neuroblast. To that end, I utilized an endogenously-labelled C-terminal GFP fusion of *ect-2* generated using CRISPR-Cas9 (*zh135*) (ECT-2::GFP) (A. Hajnal, unpublished). I divided the central Z-slice of the NSM neuroblast into ventral and dorsal halves using the cell boundary marker  $P_{pie-1}mCherry::PH^{PLCA}$ . Next, I measured ECT-2::GFP

fluorescence in the ventral and dorsal halves of the NSM neuroblast to obtain a ventral:dorsal fluorescence ratio (V:D ratio) (Figure 3.7, A). I examined this at two time-points - ~5 minutes before metaphase ( $t_{-5\text{min}}$ ) and metaphase ( $t_{0\text{min}}$ ). I found that the mean V:D ratio of ECT-2::GFP at  $t_{-5\text{min}}$  in the NSM neuroblast is 1.11 (Figure 3.7, B and C). This indicates that ECT-2 is ventrally enriched in the NSM neuroblast at  $t_{-5\text{min}}$ . Furthermore, similar to NMY-2, ECT-2 is cortically localized (Figure 3.7, B). Ventral enrichment of ECT-2::GFP was not observed at  $t_{0\text{min}}$  and the mean V:D ratio was 1.05, which is significantly different than the mean V:D ratio at  $t_{-5\text{min}}$ . As a control, I also analyzed the V:D ratios for the cell boundary marker and found that there is no ventral enrichment at  $t_{-5\text{min}}$  and at  $t_{0\text{min}}$  (Figure 3.7, D). These results suggest that there is a transient ventral enrichment of ECT-2 in the NSM neuroblast ~5 minutes before metaphase.

To further address whether the ventral enrichment of ECT-2 is transient and dynamic, I wanted to visualize ECT-2 in the NSM neuroblast at three time-points: ~10 minutes before metaphase ( $t_{-10\text{min}}$ ), ~5 minutes before metaphase ( $t_{-5\text{min}}$ ) and at metaphase ( $t_{0\text{min}}$ ). This was not possible using confocal microscopy used for the previous experiments due to bleaching issues. Therefore, I switched to super-resolution microscopy using a Zeiss LSM 980 with AiryScan2 detector as it uses very low laser power for GFP excitation that prevents excessive bleaching. Using this system, I found that ECT-2::GFP is ventrally enriched in the NSM neuroblast only at ~5 minutes before metaphase, and that there is no asymmetric enrichment at ~10 minutes before metaphase and at metaphase (Figure 3.7, E). The V:D ratio at  $t_{-10\text{min}}$ ,  $t_{-5\text{min}}$  and  $t_{0\text{min}}$  was 1.14, 1.24 and 1.05 respectively. This suggests that some unknown mechanism is driving the dynamic and transient enrichment of ECT-2 in the ventral half of the NSM neuroblast at ~5 minutes before metaphase. We believe that *ced-3* might be orchestrating these temporal dynamics of ECT-2.

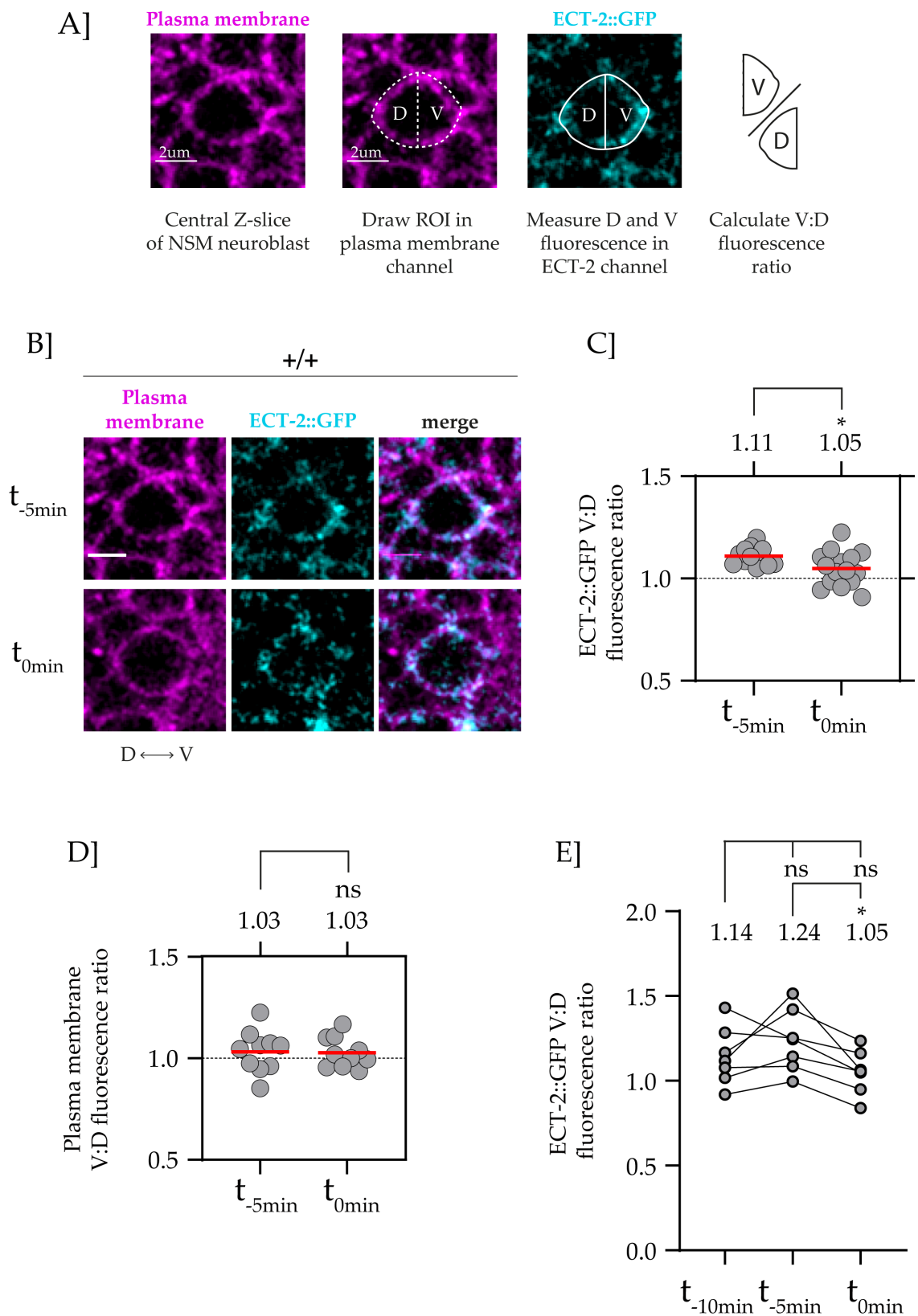


**Figure 3.7 Localization of ECT-2::GFP in the NSM neuroblast** A] Schematic representation of the methodology used to quantify ventral:dorsal fluorescence ratio of ECT-2::GFP using the plasma membrane marker. Scale bar: 2  $\mu$ m B] Representative images of the central Z-slice of

the NSM neuroblast expressing the transgene *ltIs44* ( $P_{pie-1}::mCherry::PH^{PLCA}$ ) (magenta) and CRISPR allele *zh135* (*ect-2::zf-1::gfp*) (cyan) at two timepoints – 5 minutes before metaphase ( $t_{-5min}$ ) and at metaphase ( $t_{0min}$ ). D indicates the dorsal side and V the ventral side of the NSMnb. Scale bar: 2  $\mu$ m. C, D] Ventral/dorsal (V:D) ratios of mean fluorescence intensities in the NSM neuroblast carrying the CRISPR allele *zh135* (*ect-2::zf-1::gfp*) (C) or the transgene *ltIs44* ( $P_{pie-1}::mCherry::PH^{PLCA}$ ) (D). Each gray dot represents the ventral/dorsal fluorescence intensity ratio of 1 NSM neuroblast ( $n = 10-15$ ). The mean values are indicated by the horizontal red lines and are also given on top. The horizontal black dotted line represents a fluorescence intensity ratio of 1, which indicates no asymmetry in fluorescence intensity between the ventral and dorsal side of the NSM neuroblast. Statistical significance is indicated on top.  $t_{-5min}$  is 5 minutes before metaphase and  $t_{0min}$  is at metaphase. Statistical significance was determined using the Welch's 2 sample t test (\* =  $P < 0.05$ , ns = not significant). E] Ventral/dorsal (V:D) ratios of mean fluorescence intensities in the NSM neuroblast carrying the CRISPR allele *zh135* (*ect-2::zf-1::gfp*) using super-resolution microscopy. Each gray dot represents the ventral/dorsal fluorescence intensity ratio of 1 NSM neuroblast ( $n = 8$ ). Statistical significance is indicated on top.  $t_{-10min}$  is 10 minutes before metaphase,  $t_{-5min}$  is 5 minutes before metaphase and  $t_{0min}$  is at metaphase. Statistical significance was determined using the Welch's 2 sample t test (\* =  $P < 0.05$ , ns =  $P > 0.05$ ).

### 3.2.2 Ventral enrichment of ECT-2 in the NSM neuroblast depends on *ced-3* and its caspase activity

Since we hypothesized that *ced-3* orchestrates the temporal ventral enrichment of ECT-2 in the NSM neuroblast, I analyzed the localization of ECT-2 in the NSM neuroblast in *ced-3* mutant animals. First, animals homozygous for the putative *ced-3* null allele *n717* were analyzed. I found that the ventral enrichment of ECT-2::GFP at ~5 minutes before metaphase ( $t_{-5min}$ ) was lost in *ced-3(n717)* animals. The mean V:D ratio of *ced-3(n717)* animals at  $t_{-5min}$  was 1.03, which is significantly different from the mean ratio of 1.11 in wild-type animals (Figure 3.8, A and C). In contrast, *ced-3(n717)* had no effect on ECT-2::GFP V:D ratio in the NSM neuroblast at metaphase ( $t_{0min}$ ) [1.00 in *ced-3(n717)* animals compared to 1.05 in wild-type animals] (Figure 3.8, C). This result suggests that *ced-3* influences the temporal ventral enrichment of ECT-2 in the NSM neuroblast. Next, I investigated whether the caspase activity of *ced-3* is important for the ventral enrichment of ECT-2. Thus, I analyzed animals homozygous for a missense *ced-3* mutation, *n2433*, which causes an amino acid change (G360S) that disrupts the active site of CED-3. Similar to *ced-3(n717)*, I found that the ventral asymmetric enrichment

of ECT-2::GFP at  $t_{-5\text{min}}$  was lost in *ced-3(n2433)* animals (Figure 3.7, B and C). The mean V:D ratio of animals homozygous for *ced-3(n2433)* at  $t_{-5\text{min}}$  was 1.04, which is significantly different from the mean ratio of 1.11 in wild-type animals. In contrast, *ced-3(n2433)* had no effect on ECT-2::GFP V:D ratio in the NSM neuroblast at metaphase ( $t_{0\text{min}}$ ) [1.06 in *ced-3(n2433)* animals compared to 1.05 in wild-type animals] (Figure 3.7, C). Overall, my analysis shows that the caspase activity of *ced-3* is responsible for establishing the transient ventral enrichment of ECT-2 in the NSM neuroblast at ~5 minutes before metaphase.

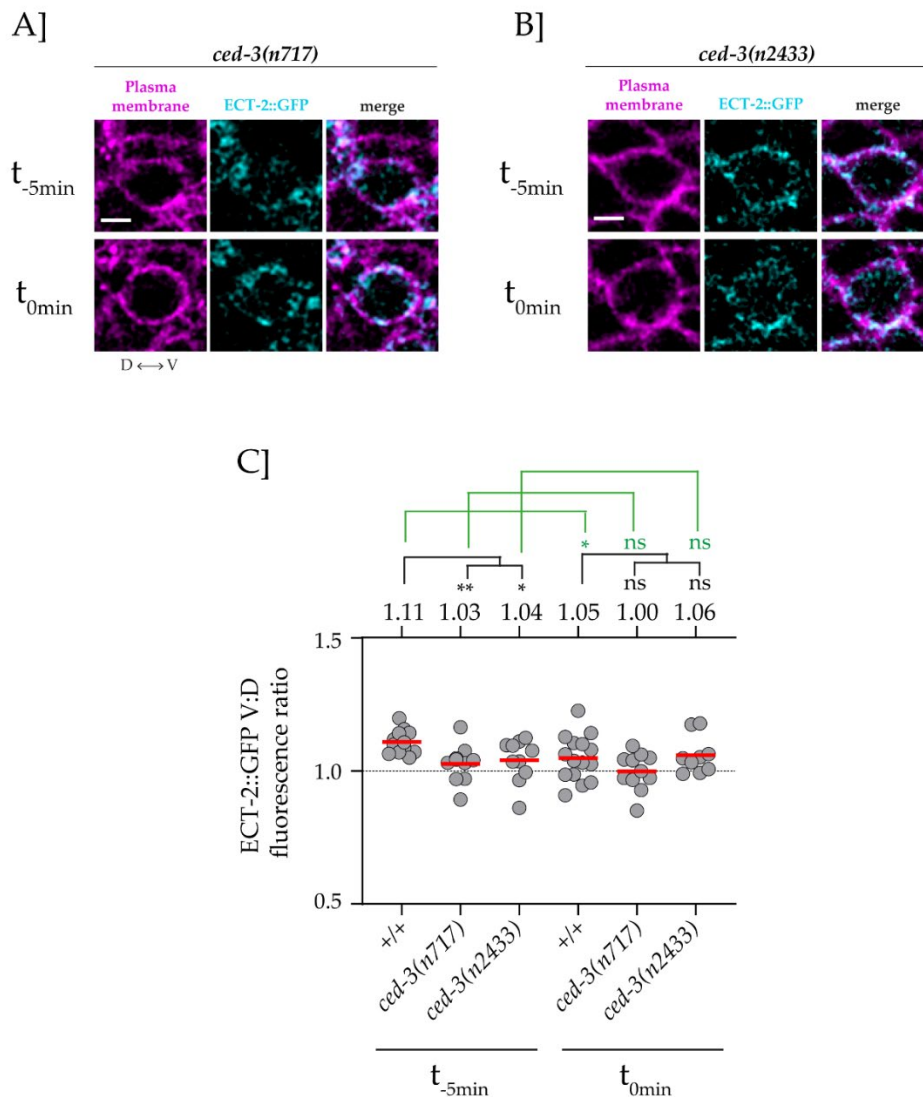


**Figure 3.8 Ventral enrichment of ECT-2::GFP in the NSM neuroblast depends on *ced-3* caspase.** A, B] Representative images of the central Z-slice of *ced-3(n717)* and *ced-3(n2433)*

NSM neuroblasts expressing the transgene *ltIs44* ( $P_{pie-1}::mCherry::PH^{PLCA}$ ) (magenta) and CRISPR allele *zh135* (*ect-2::zf-1::gfp*) (cyan) at two timepoints – 5 minutes before metaphase ( $t_{-5min}$ ) and at metaphase ( $t_{min}$ ). D indicates the dorsal side and V the ventral side of the NSMnb. Scale bar: 2  $\mu$ m. C] Ventral/dorsal (V:D) ratios of mean fluorescence intensities in the NSM neuroblast carrying the CRISPR allele *zh135* (*ect-2::zf-1::gfp*) in various genotypes. Each gray dot represents the ventral/dorsal fluorescence intensity ratio of 1 NSM neuroblast ( $n = 10-15$ ). The mean values are indicated by the horizontal red lines and are also given on top. The horizontal black dotted line represents a fluorescence intensity ratio of 1, which indicates no asymmetry in fluorescence intensity between the ventral and dorsal side of the NSM neuroblast. Statistical significance is indicated on top. The black lines represent statistical significance comparing the wild-type to *ced-3(n717)* and *ced-3(n2433)*. The green lines represent statistical significance comparing the two time points ( $t_{-5min} = 5$  minutes before metaphase,  $t_{min} =$  metaphase) of the same genotype. Statistical significance was determined using the Welch's 2 sample t test (\*\* =  $P < 0.01$ , \* =  $P < 0.05$ , ns =  $P > 0.05$ ).

### 3.2.3 Asymmetric enrichment of NMY-2 and F-actin in the NSM neuroblast is not *ced-3*-dependent

In single-celled *C. elegans* embryos, it has been shown that *ect-2* promotes actomyosin contractility in the anterior half of the embryo, which forms the larger AB daughter cell (Cowan & Hyman, 2007; Rose & Gonczy, 2014). Furthermore, studies in higher organisms show that *ect-2* promotes Myosin II activation and Formin-mediated actin polymerization, which ultimately leads to local contractions of the actomyosin network (Piekny et al., 2005). Considering that I found that ECT-2 is asymmetrically ventrally enriched in the NSM neuroblast, I wanted to investigate whether non-muscle Myosin II (NMY-2) and filamentous actin (F-actin) were also asymmetrically enriched in the NSM neuroblast. Wei et al., 2020 had shown that NMY-2 is ventrally enriched in the NSM neuroblast before division (Wei et al., 2020). To that end, I used an endogenously-labelled C-terminal GFP fusion of *nmy-2* generated using CRISPR-Cas9 (NMY-2::GFP) (Wernike et al., 2016) to examine the localization of NMY-2 in the NSM neuroblast. I also used LifeAct::GFP, which can be used to visualize F-actin *in vivo* (Redemann et al., 2010) to examine the localization of F-actin in the NSM neuroblast. I found that both, NMY-2::GFP and LifeAct::GFP were ventrally enriched in the NSM neuroblast at 5 minutes before metaphase, similar to ECT-2::GFP (Figure

3.9, A and D). The mean V:D ratios for NMY-2::GFP and LifeAct::GFP at  $t_{-5\text{min}}$  were 1.77 and 1.35 respectively (Figure 3.9, C and F). Also, similar to ECT-2::GFP, I found that there was no asymmetric enrichment of NMY-2::GFP and LifeAct::GFP at metaphase ( $t_{0\text{min}}$ ), with the mean V:D ratios being 1.12 and 1.02 respectively (Figure 3.9, A, C, D and F). These results demonstrate that components of the actomyosin network, particularly non-muscle myosin II and F-actin are also transiently ventrally enriched in the NSM neuroblast at 5 minutes before metaphase.

Next, I aimed to determine whether *ced-3* influences this transient enrichment of NMY-2 and F-actin in the NSM neuroblast. I found that the ventral enrichment of NMY-2::GFP and LifeAct::GFP was not significantly changed in animals homozygous for the *ced-3* putative null allele *n717* at both time-points (Figure 3.9 B, C, E and F). These results suggest that the *ced-3-ect-2* axis does not influence NMY-2 or F-actin localization in the NSM neuroblast. Although Ect2 has been shown to promote myosin II activation and actin polymerization in higher organisms, there is no direct evidence of such in *C. elegans*. We propose that the *ced-3-ect-2* axis acts via phosphorylation of myosin light chain (*mlc-4*) to promote actomyosin contractility and therefore we do not see an effect on NMY-2 and F-actin localization. Additionally, it is also possible that the influence of the *ced-3-ect-2* axis on NMY-2 and F-actin localization is too subtle to detect using our system.



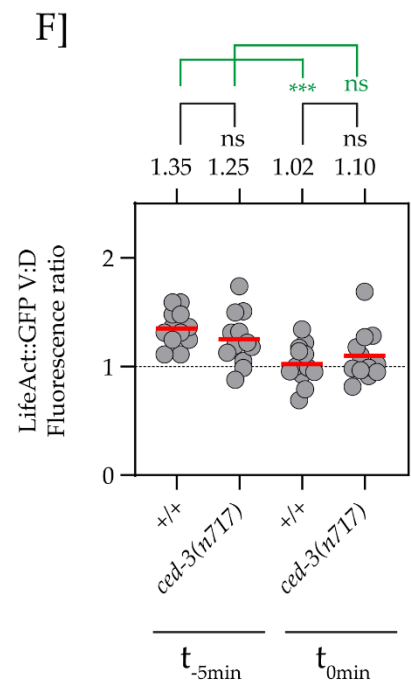
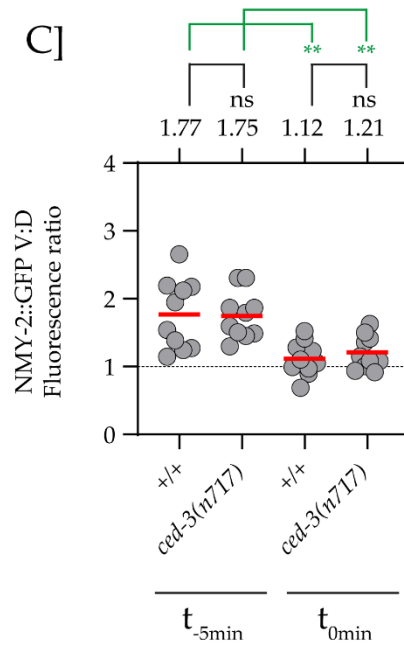
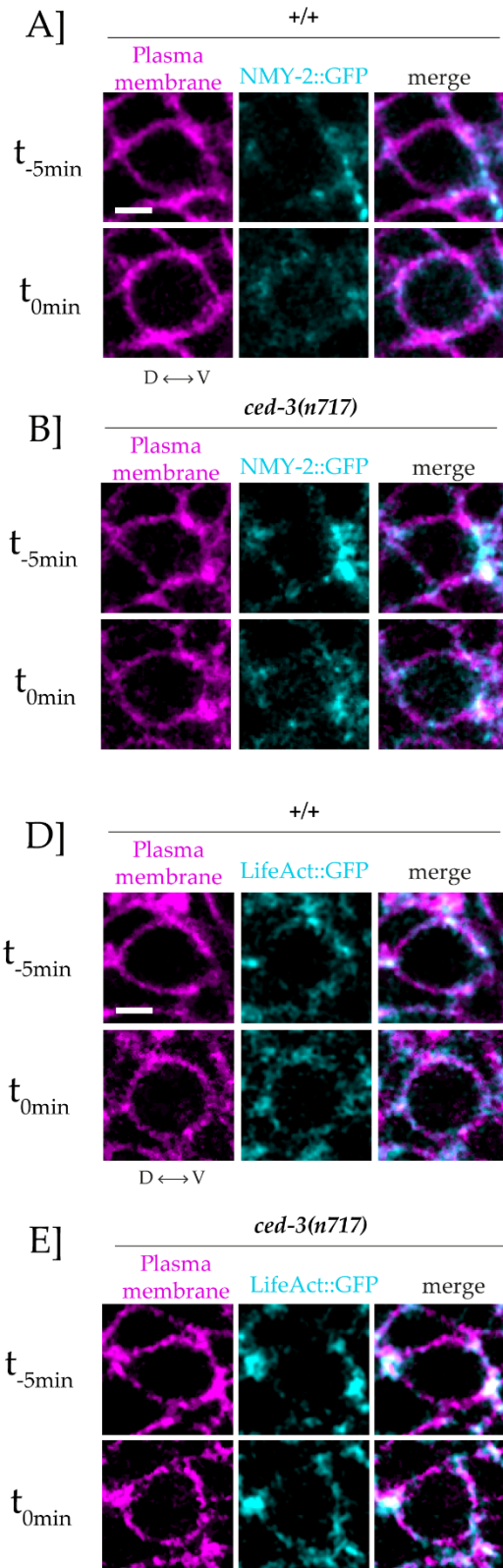


**Figure 3.9 Ventral enrichment of NMY-2::GFP and LifeAct::GFP in the NSM neuroblast does not depend on *ced-3* caspase.** A, B, D, E] Representative images of the central Z-slice of wild-type (+/+) and *ced-3(n717)* NSM neuroblasts expressing the transgene *lIs44* ( $P_{pie-1::mCherry::PH^{PLC\Delta}}$ ) (magenta) and CRISPR allele *cp13* (*nmy-2::gfp* + *LoxP*) (cyan) (A, B) or the transgene *ddl86* ( $P_{pie-1::LifeAct::gfp}$ ) (cyan) (D, E) at two timepoints – 5 minutes before metaphase ( $t_{-5min}$ ) and at metaphase ( $t_{0min}$ ). D indicates the dorsal side and V the ventral side of the NSMnb. Scale bar: 2  $\mu$ m. C, D] Ventral/dorsal (V:D) ratios of mean fluorescence intensities of wild-type (+/+) and *ced-3(n717)* NSM neuroblast carrying the CRISPR allele *cp13* (*nmy-2::gfp* + *LoxP*) (C) or *ddl86* ( $P_{pie-1::LifeAct::gfp}$ ) (F). Each gray dot represents the ventral/dorsal fluorescence intensity ratio of 1 NSM neuroblast (n = 10–15). The mean values are indicated by the horizontal red lines and are also given on top. The horizontal black dotted line represents a fluorescence intensity ratio of 1, which indicates no asymmetry in fluorescence intensity between the ventral and dorsal side of the NSM neuroblast. Statistical significance is indicated on top. The black lines represent statistical significance comparing the wild-type to *ced-3(n717)*. The green lines represent statistical significance comparing the two time points ( $t_{-5min}$  = 5 minutes before metaphase,  $t_{0min}$  = metaphase) of the same genotype. Statistical significance was determined using the Welch's 2 sample t test (\*\* =  $P < 0.01$ , \*\*\* =  $P < 0.001$ , ns =  $P > 0.05$ ).

### 3.2.4 Total CED-3 protein is uniformly distributed in the NSM neuroblast

Our biochemical assays showed that CED-3 physically interacts with ECT-2. Furthermore, our *in vivo* studies showed that ECT-2 is ventrally enriched in the NSM neuroblast, which depends on *ced-3* caspase activity. Next, we aimed to examine the localization of CED-3 in the NSM neuroblast. CED-3 protein is synthesized as an inactive zymogen called proCED-3, which needs to undergo auto-cleavage and dimerization to become fully-active CED-3 (Figure 3.10, A) (Nicholson, 1999; Srinivasula et al., 1998; Yang et al., 1998). Currently, no tools are available in *C. elegans* to visualize the cellular localization of only active CED-3. Previous attempts from our lab have also failed to construct such a tool. Therefore, I visualized total CED-3 protein (both proCED-3 and active CED-3) in the NSM neuroblast using a functional, fosmid-based reporter  $P_{ced-3::ced-3::gfp}$  (CED-3::GFP) (Chakraborty et al., 2015). I examined CED-3::GFP at two time-points - ~5 minutes before metaphase ( $t_{-5min}$ ) and at metaphase ( $t_{0min}$ ). I found that CED-3::GFP was uniformly distributed throughout the NSM neuroblast, with no evidence of any sub-cellular localization at both time-points (Figure 3.10, B). We know from previous studies in our lab that there is a dorsal to

ventral CED-3 activity gradient in the NSM neuroblast (Chakraborty et al., 2015). However, from the tools available to us currently, we cannot distinguish between total CED-3 protein and active CED-3 protein visually.

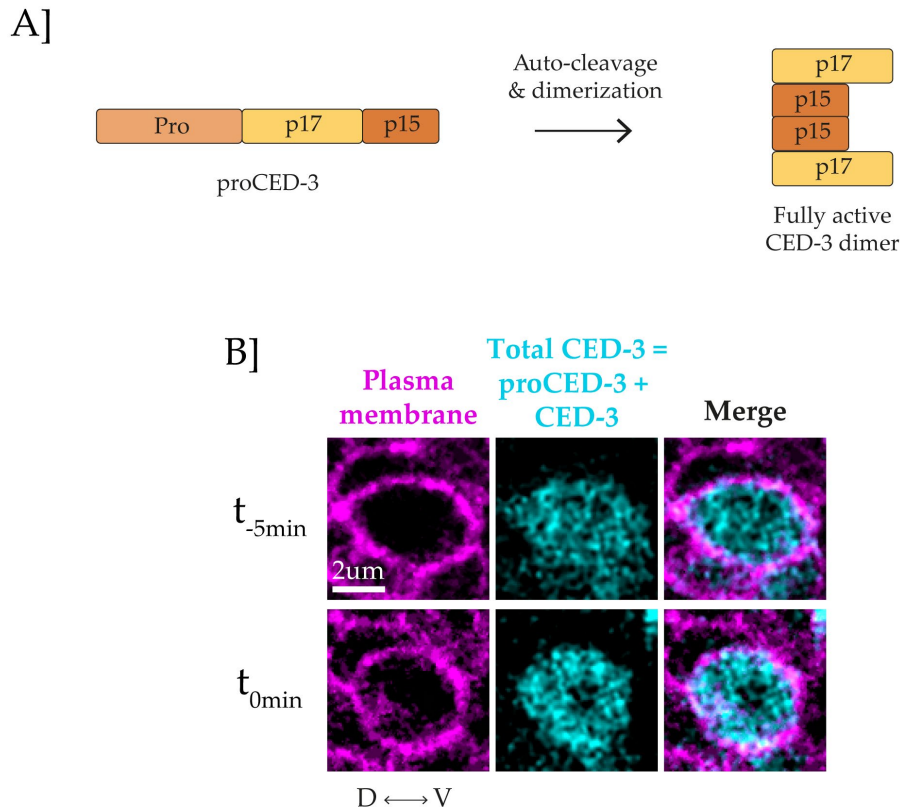


**Figure 3.10 Total CED-3 protein in the NSM neuroblast.** A] ProCED-3 has three domains – a Pro domain, a p17 domain and a p15 domain. To become fully active, proCED-3 undergoes autocleavage and dimerization to form an active CED-3 dimer, which contains two p17 domains and two p15 domains. B] Representative images of the central Z-slice of the NSM neuroblast expressing the transgene *ItIs44* ( $P_{pie-1}::mCherry::PH^{PLC\Delta}$ ) (magenta) and *bcIs109* ( $P_{ced-3}::ced-3::gfp$ ) (cyan) at two timepoints – 5 minutes before metaphase ( $t_{-5\text{min}}$ ) and at metaphase ( $t_{0\text{min}}$ ). D indicates the dorsal side and V indicates the ventral side of the NSM neuroblast. Scale bar: 2  $\mu\text{m}$ .

Overall, in sections 3.2.1 to 3.2.4, we showed that ECT-2, NMY-2 and F-actin are ventrally enriched in the NSM neuroblast ~5 minutes before metaphase. Furthermore, the ventral enrichment of ECT-2, but not NMY-2 and F-actin, is *ced-3*-dependent. In the next section, we investigated the genetic pathway that promotes the asymmetric division of the NSM neuroblast and thereby the formation of a smaller NSMsc. We

quantified NSMsc:NSM daughter cell size ratios in various loss-of-function and gain-of-function mutations to dissect this genetic pathway.

### 3.2.5 *ect-2* promotes a smaller NSM sister cell size

In the previous sections, I showed that CED-3 physically interacts with ECT-2 *in vitro* and that ECT-2 is ventrally enriched in the NSM neuroblast. The next aim of the study was to uncover whether *ect-2* has a role in controlling the asymmetric division of the NSM neuroblast and thereby the smaller size of the apoptotic daughter cell i.e. NSM sister cell (NSMsc). To that end, we quantified the cell sizes of the NSMsc and the NSM in various *ect-2* mutant backgrounds. Using a fluorescent plasma membrane marker *P<sub>pie-1</sub>mCherry::PH<sup>PLC $\Delta$</sup>* , that labels the boundary of all cells in the embryo, I was able to identify the NSM neuroblast based on the shape and the position of the cell in comma-stage embryos. Subsequently, we tracked the division of the NSM neuroblast in real-time *in vivo* and identified the two daughter cells – the smaller daughter cell (NSMsc) and the larger daughter cell (NSM) (Figure 3.11, A). The volumes of the two daughter cells were then estimated immediately post-division by summing up the area of the cells at different slices (Z-slice interval = 0.5 microns) (Figure 3.11, B). Once the volumes of the two daughter cells was determined, we divided the volume of the NSMsc with the volume of the NSM cell to obtain a ‘daughter cell size ratio’. We found that the daughter cell size ratio in wild-type embryos had a mean value of 0.66 [from 0.61 to 0.71] (Figure 3.11, B and C). This means that on average, the NSMsc is 0.66 times the size of the NSM. Next, we analysed the daughter cell size ratio in a temperature-sensitive partial loss-of-function (lf) allele of *ect-2*, *ax751ts*, caused by a point mutation that leads to an amino-acid change (G738R) (Figure 3.11, E) (Zonies et al., 2010). We found that the mean value of the daughter cell size ratio in *ax751ts* mutants increases to 0.72 [from 0.59 to 0.90], as compared to 0.66 in wild-type animals (Figure 3.11, B and C). This result demonstrates that decreasing the amount of functional *ect-2* increases the size of the smaller NSMsc as compared to wild-type

animals, which implies that *ect-2* promotes asymmetric division of the NSM neuroblast and a smaller NSMsc size.

Furthermore, we also had available to us three gain-of-function (gf) alleles of *ect-2* caused by point mutations leading to a single amino-acid change, *xs111* (E129K), *xs129* (G707D) and *zh8* (E225K) (Figure 3.11, E) (Canevascini et al., 2005; Zhang & Glotzer, 2015). These mutations most likely lead to hyper-activation of *ect-2* function. We found that all three gain-of-function alleles reduce the mean value of daughter cell size ratio as compared to wild-type animals. Specifically, the mean daughter cell size ratio in *ect-2(xs111)* animals was 0.55, in *ect-2(xs129)* animals was 0.60 and in *ect-2(zh8)* animals was 0.52 (Figure 3.11, C). Furthermore, the mean values of *xs111* and *zh8* alleles (0.55 and 0.52 respectively) were significantly different to the mean value of wild-type animals (Figure 3.11, C). The gain-of-function allele *zh8* is genetically linked to the *unc-4(e120)* mutation. Therefore, as a control, we also analyzed the daughter cell size ratio in *unc-4(e120)* animals and found no difference as compared to wild-type animals (Figure 3.11, D). Overall, these results demonstrate that hyper-activation of *ect-2* function decreases the size of the smaller NSMsc, supporting our previous findings that *ect-2* promotes a smaller NSMsc size.

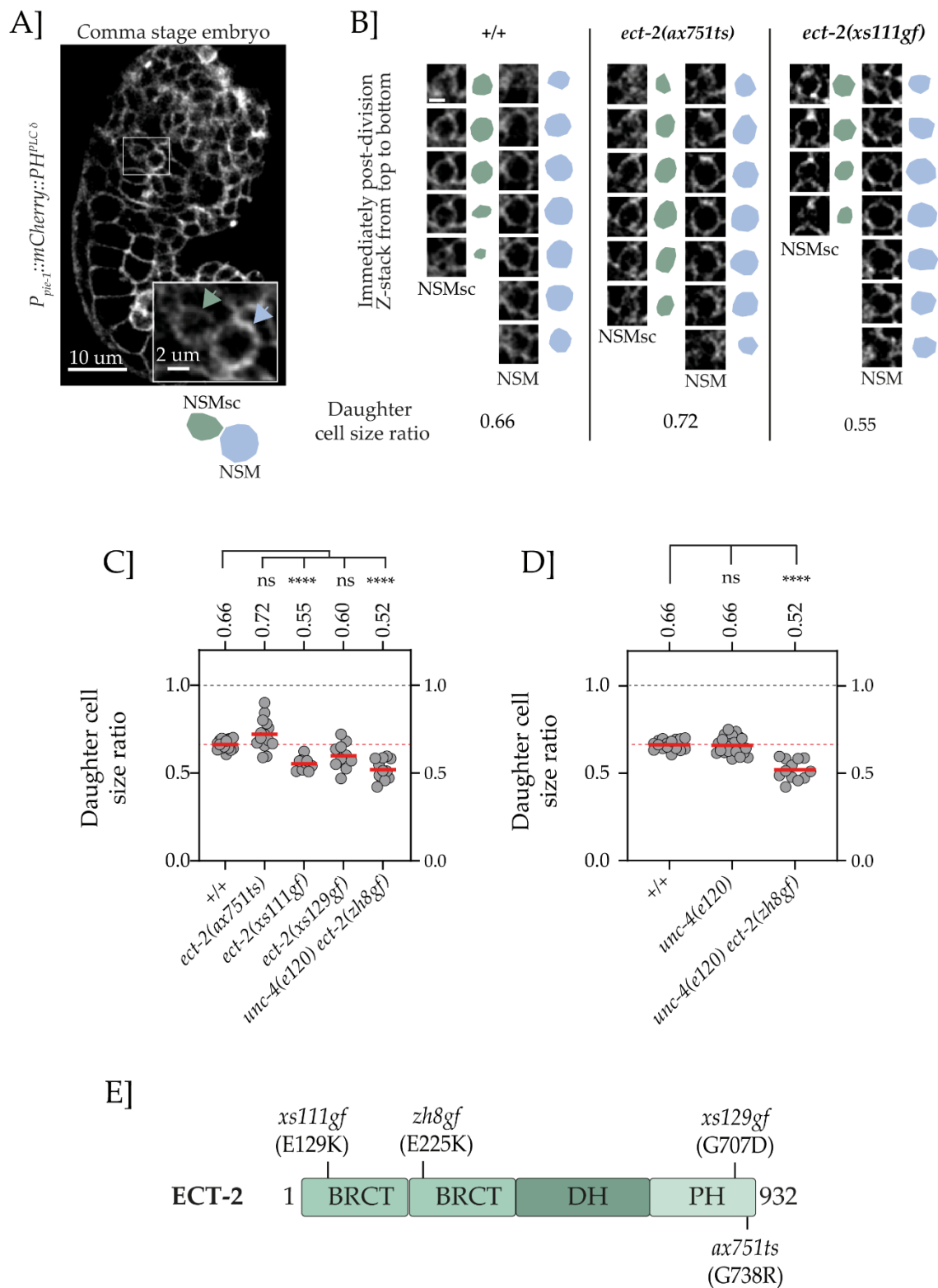


**Figure 3.11 Measuring the NSMsc:NSM daughter cell size ratio in various *ect-2* mutants.** A] The NSMsc (green) and the NSM (blue) can be identified in comma-stage embryos expressing the cell boundary marker *ItIs44* ( $P_{pie-1}::mCherry::PH^{PLC\Delta}$ ) (magenta). Scale bars: 10  $\mu$ m and 2  $\mu$ m. B] To measure the daughter cell size ratio, a Z-stack of the NSMsc (green) and the NSM (blue) is obtained immediately post-division using confocal microscopy. The

genotype is indicated on top and the daughter cell size ratio is indicated on the bottom. C, D] Daughter cell size ratios in various *ect-2* mutants. Each gray dot represents the daughter cell size ratio of one pair of daughter cells (n =10-20). Horizontal red lines represent the mean values, which is also indicated on top. The horizontal dotted red line represents the mean daughter cell size ratio of +/+ animals for comparison. The horizontal dotted black line represents a daughter cell size ratio of 1.00, which would indicate equally sized daughter cells. Statistical significance was determined using Dunnett's T3 multiple comparisons test (\*\*\*\* = P < 0.0001, ns = P > 0.05). E] Schematic representation of amino acid changes of the various *ect-2* alleles used in this study.

### 3.2.6 *ced-3* might act upstream of *ect-2* to promote a smaller NSM sister cell size

From our biochemical studies, I showed that CED-3 physically interacts with ECT-2. Additionally, I found that the ventral enrichment of ECT-2 in the NSM neuroblast depends on *ced-3* caspase activity. These results led me to propose that *ced-3* acts upstream of *ect-2* in the NSM neuroblast to promote a smaller daughter cell size. To test this hypothesis, we examined the effect of reducing *ced-3* function on the daughter cell size ratio of various *ect-2* mutant animals. This would enable me to perform epistasis analysis. First, we checked the daughter cell size ratios in three differently penetrant *ced-3* loss-of-function alleles – a very weak loss-of-function allele *n2427* (Shaham et al., 1999), an intermediately weak loss-of-function allele *n2436* (Shaham et al., 1999) and a putative null allele *n717* (Ellis & Horvitz, 1986) (Figure 3.12, A). We found that the mean daughter cell size ratios for animals homozygous for *ced-3(n2427)*, *ced-3(n2436)* and *ced-3(n717)* was 0.65, 0.66 and 0.63 respectively, which is not significantly different from the ratio of 0.66 in wild-type animals (Figure 3.12, B and C). This suggests that *ced-3* alone cannot control asymmetric cell division and promote a smaller daughter cell size. However, importantly, we found that when we combine the *ced-3* mutant alleles with *ect-2(ax751ts)* animals, the ranges of the daughter cell size ratios increase compared to the range of daughter cell size ratios of *ect-2(ax751ts)* animals alone (Figure 3.12, B). Particularly, the range of values in *ced-3(n2427); ect-2(ax751)* animals, is 0.62 to 1.00, in *ced-3(n2436); ect-2(ax751)* animals is 0.55 to 1.05 and in *ced-3(n717); ect-2(ax751)* animals is 0.54 to 1.00 (Figure 3.12, B). Strikingly, of note is

that in all double mutant animals, we observed cases where the daughter cell size ratio was 1.00, which means that the two daughter cells were of similar sizes (Figure 3.12, B). A daughter cell size ratio of 1.00 was never observed in *ect-2(ax751)* animals. These results suggest that *ced-3* acts together (in parallel or in the same pathway) with *ect-2* to promote asymmetric division of the NSM neuroblast and thereby promote a smaller NSMsc size.

Subsequently, I wanted to test the interaction between *ced-3* loss-of-function alleles with the *ect-2* gain-of-function alleles. As shown previously, *ect-2* gain-of-function animals have a decreased daughter cell size ratio as compared to wild-type animals. We found that the *ced-3* loss-of-function alleles did not significantly alter the daughter cell size ratios of the *ect-2* gain-of-function animals (Figure 3.12, C). These results suggest that *ced-3* acts either upstream of or in parallel to *ect-2* to promote a smaller NSMsc size. However, owing to the fact that CED-3 physically interacts with ECT-2 *in vitro* and that ECT-2 enrichment depends on *ced-3*, we propose that *ced-3* most likely acts upstream of *ect-2* to promote asymmetric division of the NSM neuroblast and a smaller daughter cell size. We refer to this axis as the '*ced-3-ect-2* axis'.



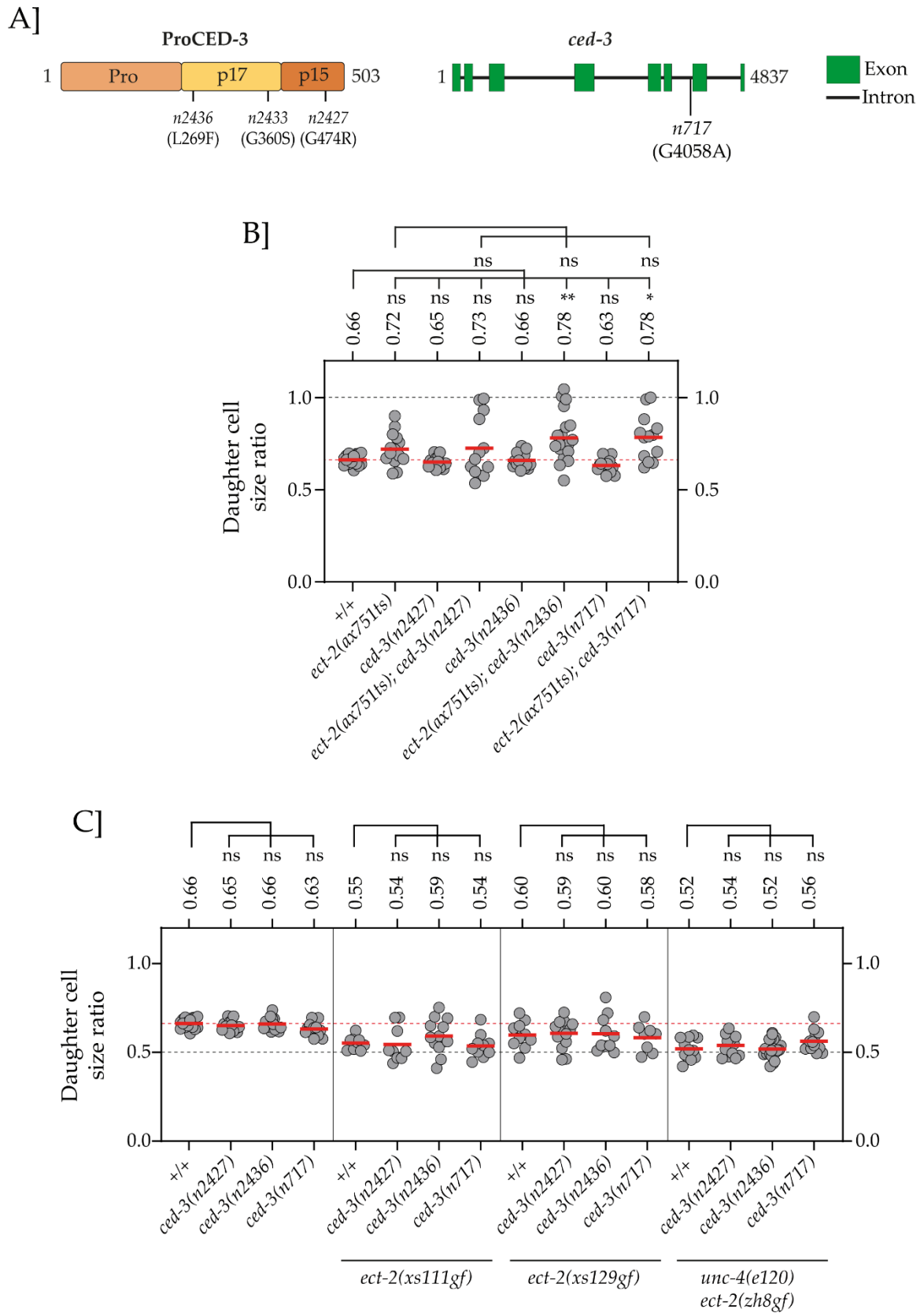


**Figure 3.12 NSMsc:NSM daughter cell size ratios in various *ect-2* and *ced-3* mutants.** A] Schematic representation of proCED-3 protein and *ced-3* gene indicating the amino acid or nucleotide changes in the *ced-3* alleles used in this study. B, C] Daughter cell size ratios in

various *ect-2* and *ced-3* mutants. Each gray dot represents the daughter cell size ratio of one pair of daughter cells (n =10-20). Horizontal red lines represent the mean values, which is also indicated on top. The horizontal dotted red line represents the mean daughter cell size ratio of +/+ animals for comparison. The horizontal dotted black line in B represents a daughter cell size ratio of 1.00, which would indicate equally sized daughter cells. The horizontal dotted black line in C represents a daughter cell size ratio of 0.5, which would indicate that the NSMsc is half the size of the NSM. Statistical significance was determined using Dunnett's T3 multiple comparisons test (\*\* = P < 0.01, \* = P < 0.05, ns = P > 0.05).

### **3.2.7 The *ced-3-ect-2* axis acts in parallel with the *pig-1-nmy-2* axis to promote a smaller daughter cell size**

Studies from our lab had previously shown that the gene *pig-1*, which encodes for the *C. elegans* orthologue of the mammalian 'Maternal Embryonic Leucine Zipper Kinase' (MELK), controls the asymmetric division of the NSM neuroblast (Wei et al., 2020). *pig-1* was found to act upstream of *nmy-2*, where PIG-1 kinase phosphorylates NMY-2 and this promotes a smaller NSMsc size. It was shown that in animals homozygous for a *pig-1* loss-of-function mutation, *gm344*, the daughter cell size ratio increases from 0.64 to 1.01, indicating that the two daughter cells are of similar sizes (Wei et al., 2020). Additionally, animals homozygous for the temperature-sensitive *nmy-2* loss-of-function mutation *ne3409ts* also led to formation of similarly sized daughter cells (Wei et al., 2020). Genetic studies also revealed that *par-4* LKB, *strd-1* STRAD $\alpha$  and *mop-25.1/2* MO25 act upstream of *pig-1* in this context (Wei et al., 2020). We refer to this as the '*pig-1-nmy-2* axis'.

Notably, it was also shown that the putative null allele of *ced-3*, *n717*, enhances the daughter cell size ratio in *pig-1* loss-of-function animals from 1.00 to 1.25 (Mishra et al., 2018). This result depicts that in animals that have a loss-of-function of both genes, *ced-3* and *pig-1*, the daughter cell size asymmetry is reversed and the NSMsc is now larger than the NSM. This would imply that *ced-3* acts in parallel or together with *pig-1* to ensure that the size of the NSMsc is below a critical threshold. Since we propose that *ect-2* acts in the same pathway as *ced-3* to promote a smaller NSMsc size, I wanted to examine the daughter cell size ratios in animals homozygous for both *ect-2* and *pig-*

1 mutations. To that end, I attempted to construct a *C. elegans* strain that was homozygous for the loss-of-function of both, *ect-2* and *pig-1*. However, animals homozygous for both, *ect-2(ax751)* and *pig-1(gm344)* showed a synthetic lethal phenotype and therefore could not be analyzed.

To circumvent this issue, I decided to utilize the gene *strd-1* (STRAD $\alpha$ ), which has been shown to act upstream of *pig-1* in the *pig-1-nmy-2* axis (Wei et al., 2020). Specifically, it was shown that the daughter cell size ratio of animals homozygous for the loss-of-function mutation of *strd-1*, was similar to the daughter cell size ratio of animals homozygous for loss-of-function of both, *pig-1* and *strd-1* (Wei et al., 2020). I used the loss-of-function allele of *strd-1*, *ok2283* (Consortium, 2012) and found that animals homozygous for *ok2283* had a mean daughter cell size ratio of 0.97 (Figure 3.13, A). Importantly, I found that reducing the amount of functional *ect-2* using the partial loss-of-function allele *ect-2(ax751)* further increases the mean daughter cell size ratio of animals homozygous for *strd-1(ok2283)* from 0.97 to 1.11 (Figure 3.13, A). Notably, in some cases, animals homozygous for both *ect-2(ax751)* and *strd-1(ok2283)* showed a daughter cell size ratio of more than 1.20, indicating that the NSMsc was now much larger than the NSM (Figure 3.13, A). Subsequently, I also examined the daughter cell size ratios in animals homozygous for the gain-of-function mutation of *ect-2*, *xs111*, and loss-of-function of *strd-1*, *ok2283*. I found that *ect-2(xs111)* suppresses the daughter cell size ratio found in *strd-1(ok2283)* animals, from 0.97 to 0.83 (Figure 3.13, A). Taken together, from my findings of these experiments, I propose that the *ced-3-ect-2* axis acts in parallel to the *pig-1-nmy-2* axis to promote a smaller NSMsc size.

### 3.2.8 *nop-1* does not act with *ect-2* to promote a smaller NSM sister cell size

Recently, a novel regulator of cytokinesis and polarization in the single-celled *C. elegans* embryo was identified, called *nop-1* (No pseudocleavage or reduced pseudocleavage) (Rose et al., 1995). *nop-1* was shown to act as an upstream activator of *ect-2*, redundantly with *cyk-4*, during the polarization phase and cytokinesis of the single-cell embryo (Tse et al., 2012). Interestingly, *nop-1* was shown to be the predominant RhoA activator present during the polarization phase, whereas, both *cyk-4* and *nop-1* acted together during cytokinesis (Tse et al., 2012). I knew from our *in vivo* localization studies that ECT-2 is asymmetrically enriched in the NSM neuroblast before metaphase and cytokinesis, and thus, I imagined that *nop-1* would be a good candidate for the upstream activator of ECT-2 during this time-point. Therefore, I aimed to investigate whether *nop-1* acts upstream of *ect-2* in NSM neuroblast to control its asymmetric division and thereby a smaller NSMsc size. To that end, I used a putative null mutant of *nop-1*, *it142* caused by a nonsense mutation that leads to a premature stop codon (W696X) (Tse et al., 2012). I found that animals homozygous for *nop-1(it142)* did not have an effect on the daughter cell size ratio as compared to wild-type animals (Figure 3.13, B). The mean value of the daughter cell size ratio in *nop-1(it142)* animals was 0.60 as compared to 0.61 in wild-type animals (Figure 3.13, B). Furthermore, I imagined that maybe *ced-3* and *nop-1* act together as upstream regulators of *ect-2*. Therefore, I analyzed daughter cell size ratios in animals homozygous for both, *nop-1(it142)* and *ced-3(n717)*. However, again, I did not see a significant effect on the mean daughter cell size ratio as compared to wild-type animals. The mean value of the daughter cell size ratio in *nop-1(it142); ced-3(n717)* animals was 0.62 as compared to 0.61 in wild-type animals (Figure 3.13, B). From these results, we could conclude that *nop-1* is not an upstream regulator of *ect-2* for promoting asymmetric division of the NSM neuroblast.

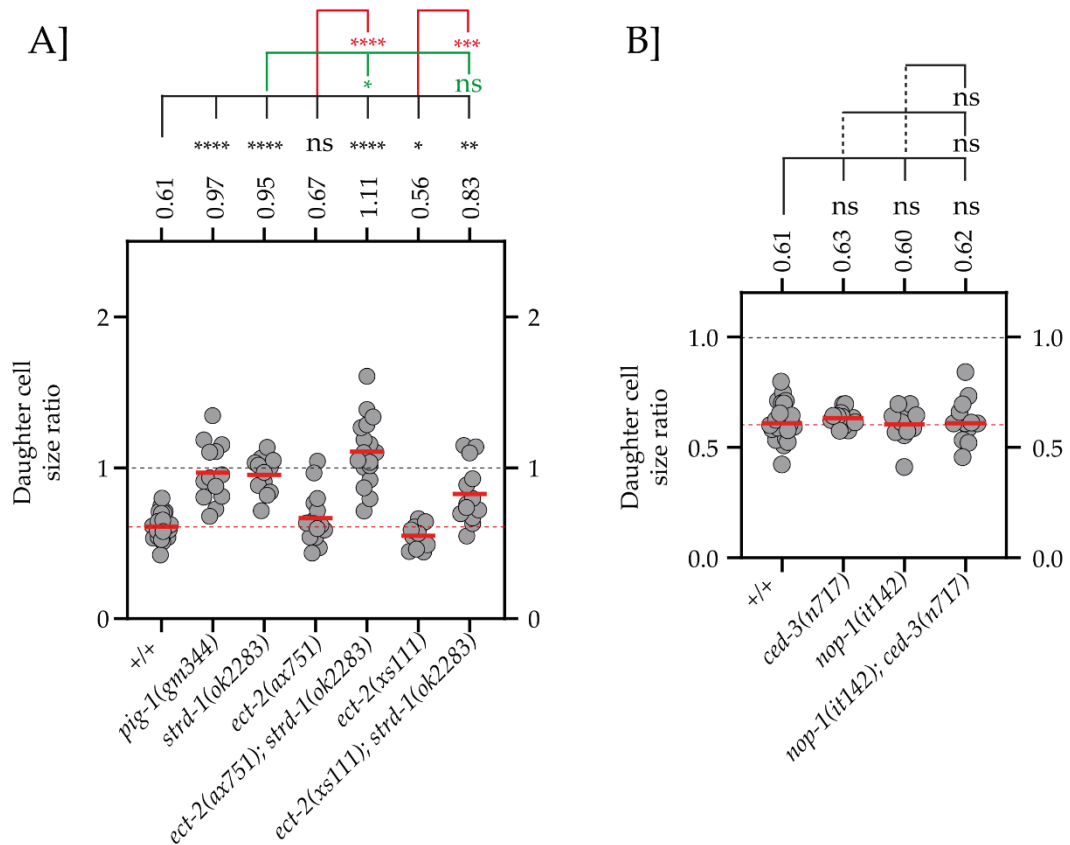


**Figure 3.13 NSMsc:NSM daughter cell size ratios in various mutants** A, B] Daughter cell size ratios in various mutants with the genotype indicated on the X-axis. Each gray dot represents the daughter cell size ratio of one pair of daughter cells (n =10-30). Horizontal red lines represent the mean values, which is also indicated on top. The horizontal dotted red line represents the mean daughter cell size ratio of +/+ animals for comparison. The horizontal dotted black line represents a daughter cell size ratio of 1.00, which would indicate equally sized daughter cells. Statistical significance was determined using Welch’s two-sample t-test (\*\*\*\* =  $P < 0.0001$ , \*\* =  $P < 0.01$ , \* =  $P < 0.05$ , ns =  $P > 0.05$ ).

Overall, in sections 3.2.5 to 3.2.8, we showed that the *ced-3-ect-2* axis promotes asymmetric division of the NSM neuroblast and thereby the formation of a smaller NSMsc. We also showed that this axis acts in parallel to the previously discovered *pig-1-nmy-2* axis. In the next section, we aimed to investigate the effect of the size of the NSMsc on its apoptotic fate.

### 3.3 A smaller cell size promotes apoptosis

---

#### 3.3.1 Larger NSMsc are more prone to survive

From our *in vivo* daughter cell size studies, we showed that the *ced-3-ect-2* axis promotes a smaller NSMsc size. We showed that a partial loss-of-function mutation of *ect-2* leads to a relatively larger NSMsc when compared to wild-type. Conversely, increasing *ect-2* function via the gain-of-function mutations leads to a relatively smaller NSMsc. Subsequently, we wanted to investigate the effect of changing the size of the NSMsc on its apoptotic fate. To that end, we used a serotonergic neuron reporter, *Ptph-1::his-24::gfp*, which labels all serotonergic neurons in *C. elegans* larvae and adults (Yan et al., 2013). Using this reporter, it is possible to identify the NSM neuron in the lower half of the anterior pharynx of L3/L4 animals (Figure 3.14, A). In wild-type animals, the NSM differentiates to form a neuron that can be seen in the anterior pharynx (Figure 3.14, A), and the NSMsc always undergoes apoptosis, which leads to 0% NSM sister cell survival (Figure 3.14, B). In contrast, animals that have a null mutation in the pro-apoptotic *ced-3* gene, like *ced-3(n717)*, show a NSMsc survival of 100%, indicating that the NSMsc does not undergo apoptosis (Figure 3.14, B).

Using the NSMsc survival assay, we found that decreasing *ect-2* function by using *ect-2(ax751)* mutation leads to a NSMsc survival of 4% (Figure 3.14, B). Furthermore, we found that *ect-2(ax751)* enhances the NSMsc survival phenotype of two partial loss-of-function mutations of *ced-3*. Specifically, *ect-2(ax751)* increases the NSMsc survival in *ced-3(n2427)* animals from 18% to 25%, and in *ced-3(n2436)* animals from 68% to 81% (Figure 3.14, B). We know from cell size studies that in *ect-2(ax751)* animals, the NSMsc is slightly larger than the NSMsc in wild-type animals. Additionally, *ect-2(ax751)* increases the relative size of the NSMsc in *ced-3* mutants (Figure 3.12, B). From these results, we propose that increased survival of the NSMsc in *ect-2(ax751)* animals is because of the increase in the relative size of the NSMsc.

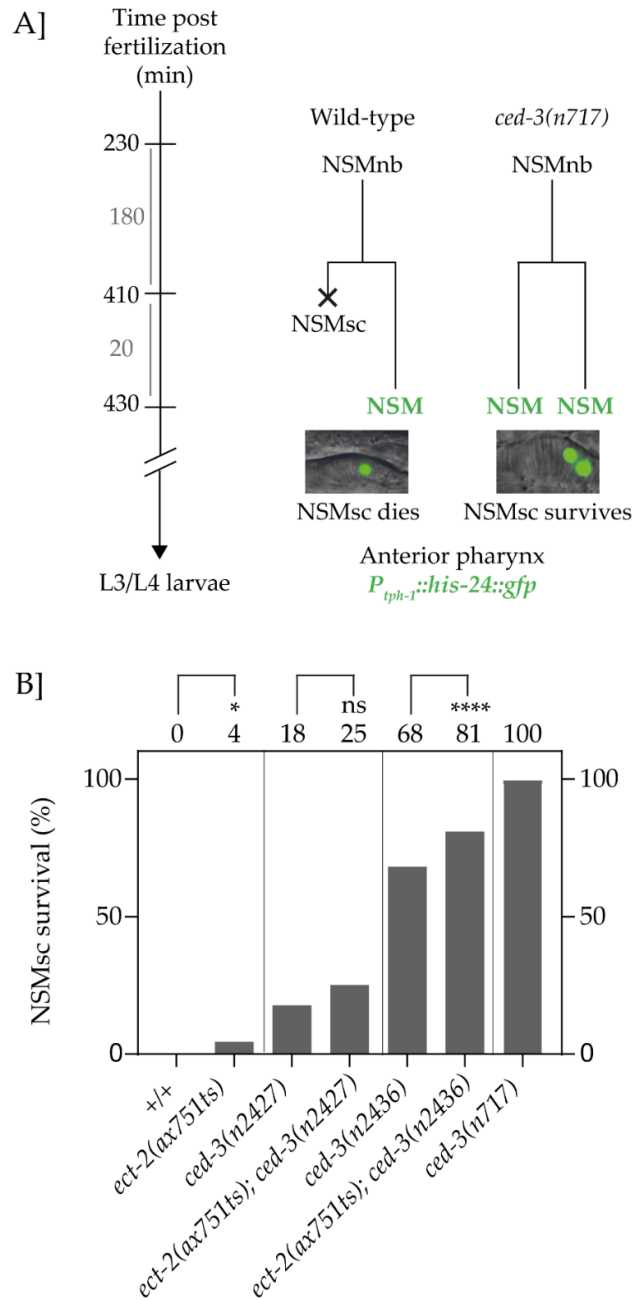


**Figure 3.14 Larger NSMsc are more prone to survive.** A] Schematic of the NSM lineage, where the differentiated NSM neuron can be identified in the anterior pharynx of L3/L4 larvae using the *P<sub>tph-1</sub>::his-24::gfp* transgene reporter. In wild-type (+/+) animals, the NSMsc always dies (indicated with a black cross) and one surviving NSM neuron can be seen on each side of the anterior pharynx. In cell death mutants, such as *ced-3(n717)*, the NSMsc survives to form an 'NSM'-like cell and thereby two 'NSM' neurons can be seen on each side of the anterior pharynx. B] Bar graphs depicting the NSMsc survival percentage in various mutants (n = 100-200). The NSMsc survival percentage is denoted on top of each bar graph. Statistical significance was determined using Fischer's exact test. (\*\*\*\* = P < 0.0001, \* = P < 0.05, ns = P > 0.05).

### 3.3.2 Smaller NSMsc are more prone to die

We next examined the effect of reducing the size of the NSMsc on its apoptotic fate. We used the three gain-of-function alleles of *ect-2* (*xs111*, *xs129* and *zh8*) to reduce the size of the NSMsc. We found that *ect-2(xs111)*, *ect-2(xs129)* and *ect-2(zh8)* animals had a NSMsc survival of 0%, the same as wild-type animals (Figure 3.15, A). This is expected because in wild-type animals the NSMsc always dies. However, very interestingly, we found that all three gain-of-function alleles of *ect-2* suppress the NSMsc survival phenotype of the two partial loss-of-function alleles of *ced-3*. Specifically, the NSMsc survival in *ced-3(n2427)* animals is 18%, which is reduced to 9%, 11% and 5% when combined with *ect-2(xs111)*, *ect-2(xs129)* and *ect-2(zh8)* respectively (Figure 3.15, A). The NSMsc survival in *ced-3(n2436)* animals is 68%, which is reduced to 26%, 40% and 41% when combined with *ect-2(xs111)*, *ect-2(xs129)* and *ect-2(zh8)* respectively (Figure 3.15, A). Furthermore, we also utilized two partial loss-of-function mutations of the two other pro-apoptotic genes, *ced-4* and *egl-1*. The NSMsc survival phenotype of *ced-4(n3312)* and *egl-1(n3331)* animals is 31% and 19% respectively, which is reduced to 19% and 13% respectively, when combined with *ect-2(xs111)* gain-of-function mutation (Figure 3.15, B). (Strains carrying the *ced-4(n3312)* mutation were maintained and scored for NSMsc survival at 15°C). The suppression of the Ced (cell death) phenotype of the weak apoptotic mutants has not been observed before, at least to the best of our knowledge. From our cell size studies, we know that *ect-2* gain-of-function mutations reduce the relative size of the NSMsc in *ced-3* mutant backgrounds. From these results, we propose that reducing the size of the NSMsc increases its ability to undergo apoptosis, even when the apoptotic pathway has been partially compromised. Overall, we hypothesize that there is an inverse correlation between apoptosis and cell size – smaller cells are more prone to die, whereas larger cells have a higher probability to survive.



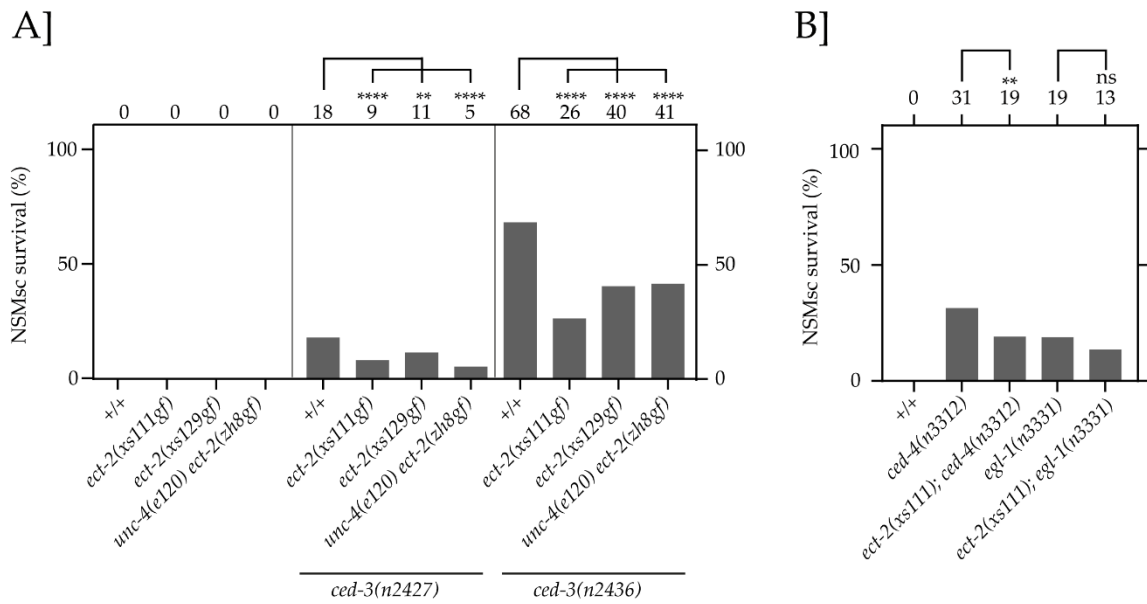


**Figure 3.15 Smaller NSMsc are more prone to die.** A, B] Bar graphs depicting the NSMsc survival percentage in various mutants (n = 100-200). The NSMsc survival percentage is denoted on top of each bar graph. Statistical significance was determined using Fischer's exact test. (\*\*\*\* =  $P < 0.0001$ , \*\* =  $P < 0.01$ , ns =  $P > 0.05$ ).

### 3.3.3 Size-dependent death of the NSMsc depends on the apoptotic pathway

In the previous result we showed that reducing the size of the NSMsc increases its ability to undergo apoptosis, even when the apoptotic pathway has been partially compromised. Next, we wondered whether the enhanced ability of smaller cells to die was mediated via the apoptotic pathway or was independent of the apoptotic pathway. To that end, we used a putative null allele of *ced-3*, *n717*, which shows a NSMsc survival of 100% (Figure 3.16, A). We combined *ced-3(n717)* with either of the three gain-of-function mutations of *ect-2* (*xs111*, *xs129* and *zh8*) and investigated the NSMsc survival in these double mutants. We observed that the *ect-2* gain-of-function mutations did not suppress the NSMsc survival of *ced-3(n717)* animals. The NSMsc survival of *ced-3(n717); ect-2(xs111)* animals is 100%, of *ced-3(n717); ect-2(xs129)* animals is 100% and of *ced-3(n717); ect-2(zh8)* animals is 99% (Figure 3.16, A). I also investigated the effect of *ect-2(xs111)* on NSMsc survival of null alleles of the two remaining pro-apoptotic genes – *ced-4* and *egl-1*, which act upstream of *ced-3* in the

central apoptotic pathway. Animals homozygous for the null allele of *ced-4(n1162)* or *egl-1(n3330)* showed a NSMsc survival phenotype of 96% and 98% respectively, indicating that almost all NSMsc survive (Figure 3.16, B). The gain-of-function mutation of *ect-2, xs111*, did not suppress the NSMsc survival of *ced-4(n1162)* and *egl-1(n3330)*. Animals homozygous of *ced-4(n1162); ect-2(xs111)* showed a NSMsc survival of 97% and animals homozygous of *egl-1(n3330); ect-2(xs111)* showed a NSMsc survival of 97% (Figure 3.16, B). Taken together, these results show that the enhanced ability of smaller cells to die depends on the central apoptotic pathway rather than a different kind of cell elimination. These results also suggest that cell size acts upstream of the central apoptotic pathway in this context.

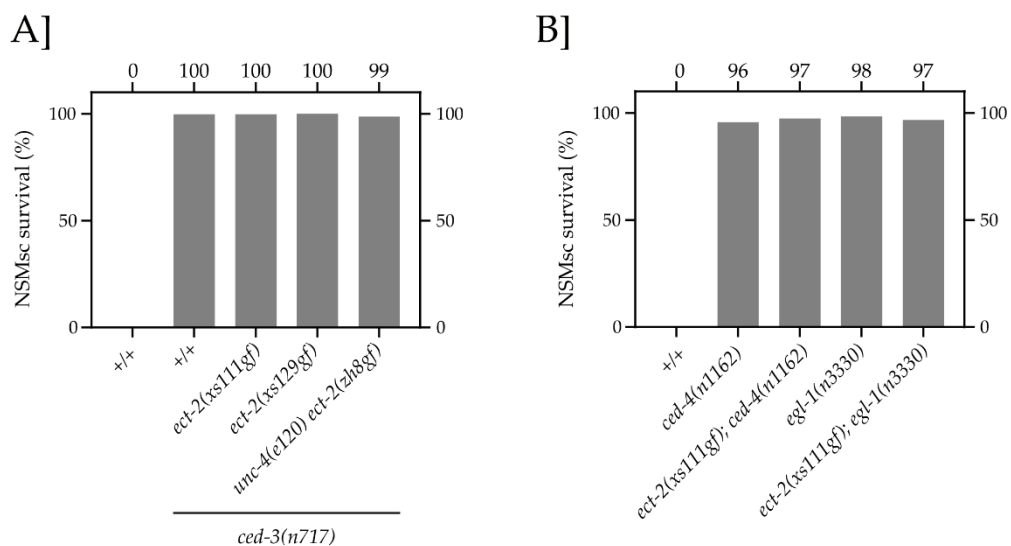


**Figure 3.16 Size-dependent death of the NSMsc depends on the apoptotic pathway.** A, B] Bar graphs depicting the NSMsc survival percentage in various mutants (n = 100-200).

### 3.4 Other experiments performed to investigate the *ced-3-ect-2* axis

---

#### 3.4.1 The *ced-3-ect-2* axis promotes mitotic rounding of the NSM neuroblast

Mitotic rounding is a universal phenomenon in all animal cells, where cells undergo dramatic structural changes during the onset of mitosis to form a rigid cortex and a completely spherical cell (Taubenberger et al., 2020). Defects in mitotic rounding have severe consequences on chromosome segregation and cell division, which can ultimately lead to diseases such as cancer (Cadart et al., 2014). Actomyosin reorganization is a key regulator of mitotic rounding and several factors are known to play a role in this process, such as myosin II, RhoA and members of the ezrin/radixin/moesin (ERM) family of actin crosslinkers (Kelkar et al., 2020). Interestingly, it was shown that export of Ect2 from the nucleus to the cytoplasm during the onset of mitosis drives the mitotic rounding of HeLa cells (Matthews et al., 2012). From our previous results, we had proposed that binding of CED-3 to the PH domain of ECT-2 clears it from the dorsal cortex of the NSM neuroblast before metaphase. Therefore, we tested whether the *ced-3-ect-2* axis also had an effect on mitotic rounding.

Like all animal cells, the NSM neuroblast undergoes dramatic cell shape changes during *C. elegans* embryonic development. Initially, the NSM neuroblast has an ovoid shape, which subsequently becomes completely rounded during metaphase (Figure 3.17, A). I measured the circularity of the central Z-slice of the NSM neuroblast at metaphase using cell boundary marker  $P_{pie-1mCherry}::PH^{PLC\Delta}$  (Figure 3.17, B). A circularity value of 1.00 means a completely circular cell. I found that in wild-type animals, the NSM neuroblast had a mean circularity value of 0.97 at metaphase (Figure 3.17, C and D). Neither the partial loss-of-function allele of *ect-2(ax751)*, nor the putative null allele of *ced-3(n717)* had an effect on metaphase circularity of the NSM neuroblast (Figure 3.17, C and D). Conversely, animals homozygous for both, *ect-*

*2(ax751)* and *ced-3(n717)*, showed a significant reduction in circularity compared to wild-type (from 0.97 in wild-type to 0.93 in *ect-2(ax751); ced-3(n717)* animals) (Figure 3.17, C and D). These results suggest that *ect-2* and *ced-3* have a synergistic effect on mitotic rounding. We believe that the *ced-3-ect-2* axis might influence actomyosin reorganization and thereby mitotic rounding of the NSM neuroblast.

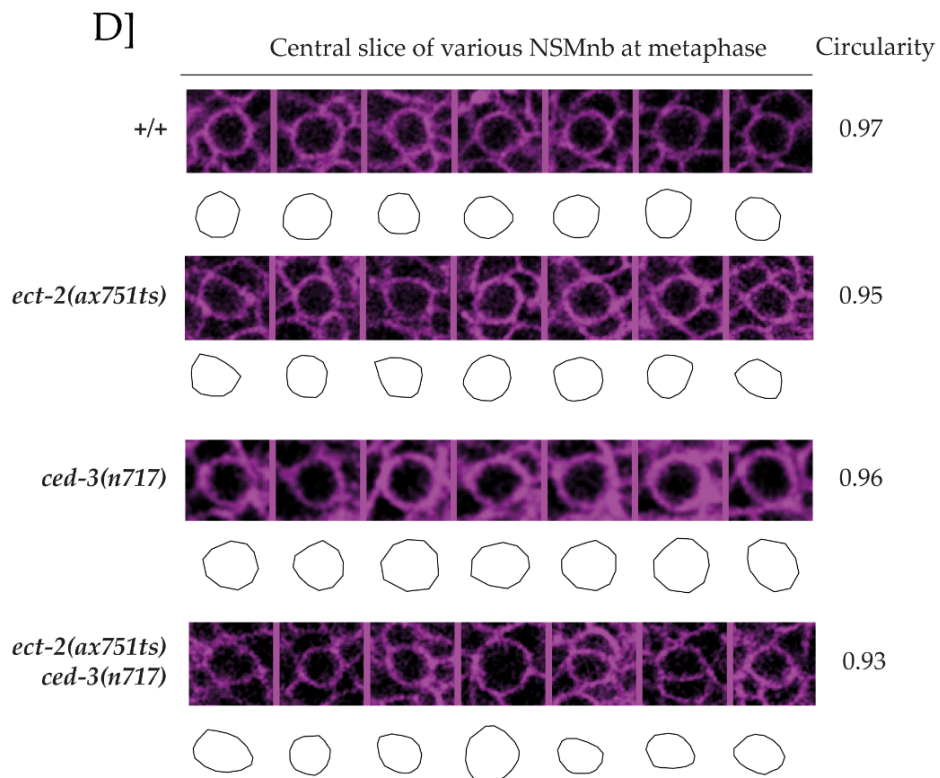
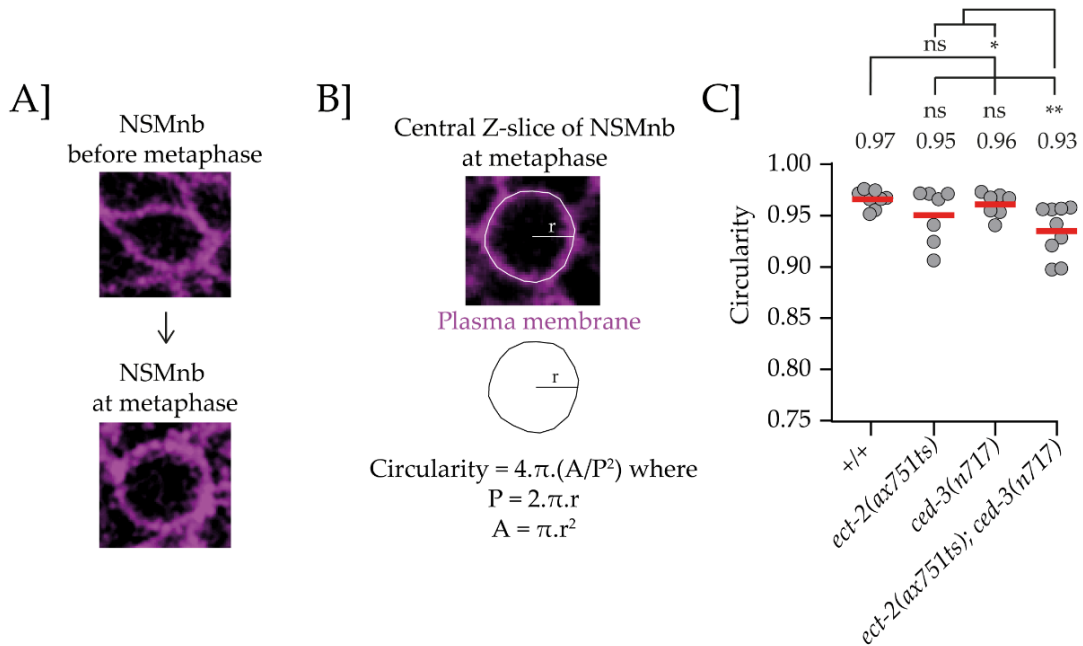


**Figure 3.17 Metaphase rounding of the NSM neuroblast depends on the *ced-3-ect-2* axis.** A] The NSM neuroblast (NSMnb) appears elliptical before metaphase and adopts a more rounded spherical shape during metaphase. B] To calculate the circularity of the NSMnb, a region of interest was drawn on the cell boundary of the NSMnb at metaphase using the plasma membrane marker  $P_{pie-1mCherry::PH^{PLCA}}$ . The radius of the region of interest was used to calculate the circularity with the given formula. C] Circularity of the NSMnb at metaphase in various genotypes. Each gray dot represents one NSMnb at metaphase (n=8-10). The horizontal red line indicates the mean value, which is also written on top. Statistical significance was calculated using Welch's two-sample t-test (\*\* =  $P < 0.01$ , \* =  $P < 0.05$ , ns =  $P > 0.05$ ). D] Representative images showing the central Z-slice of seven NSMnbs at metaphase, with the genotype indicated on the left and the mean circularity value on the right.

**4**

# **DISCUSSION**

## 4.1 Reciprocal interactions between the apoptotic pathway and cell size are coordinated by the *ced-3-ect-2* axis

---

Based on our findings, we propose that there are reciprocal interactions between the apoptotic pathway and cell size (Figure 4.1). In the mother of the apoptotic cell (NSMnb), the apoptotic pathway promotes asymmetric division by size of the mother cell and thereby the formation of a smaller apoptotic daughter cell (NSMsc). Here, the apoptotic pathway acts upstream of cell size (Figure 4.1). Conversely, in the smaller apoptotic daughter cell, the small cell size promotes the activation/activity of the apoptotic pathway. Here, cell size acts upstream of the apoptotic pathway (Figure 4.1). The details of these reciprocal interactions are discussed below in sections 4.1.1 to 4.1.3.

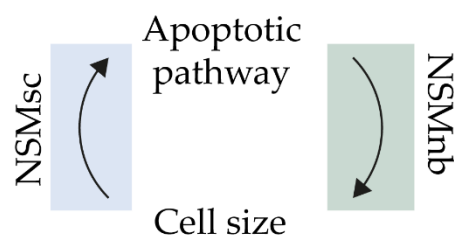


**Figure 4.1 Reciprocal interactions between the apoptotic pathway and cell size.** In the NSM neuroblast (NSMnb) (green), the apoptotic pathway acts upstream of cell size. In the NSM sister cell (NSMsc) (blue), cell size acts upstream of the apoptotic pathway.

### 4.1.1 CED-3 caspase mediates the clearance of ECT-2 RhoGEF from the dorsal cortex of the NSM neuroblast

Our data showed that there is a transient enrichment of ECT-2 RhoGEF in the ventral cortex of the NSM neuroblast at approximately 5 minutes before metaphase (Figure 4.2). Conversely, we also showed that ECT-2 is uniformly localized in the cortex of the NSM neuroblast 10 minutes before metaphase and at metaphase (Figure 4.2). These findings suggest that at 5 minutes before metaphase, ECT-2 is cleared from the dorsal

cortex, which leads to its enrichment on the ventral cortex of the NSM neuroblast. Interestingly, it has been previously shown in our lab that CED-3 caspase forms a dorsal to ventral activity gradient in the NSM neuroblast (Figure 4.2) (Chakraborty et al., 2015). Therefore, we propose that CED-3 caspase de-recruits ECT-2 from the dorsal cortex of the NSM neuroblast, thereby leading to its ventral enrichment at 5 minutes before metaphase (Figure 4.2). To support this hypothesis, we looked at ECT-2 localization in two *ced-3* mutants – a putative null mutation and a mutation that disrupts CED-3's active site. In both mutants, we found that the ventral enrichment of ECT-2 at 5 minutes before metaphase is lost (Result 3.2.2). Therefore, CED-3 caspase and its activity is required for the clearance of ECT-2 from the dorsal cortex. Additionally, we also found that CED-3 physically interacts with the PH domain of ECT-2 *in vitro* (Result 3.1.4). The PH domain is a protein domain that can bind to phosphatidylinositol lipids in the plasma membrane and is responsible for recruiting proteins to the membrane (Wang & Shaw, 1995). Thus, we imagine that either binding of CED-3 to ECT-2's PH domain or CED-3-mediated cleavage of the PH domain enables ECT-2's clearance from the dorsal cortex of the NSM neuroblast (Figure 4.2). However, using our *in vitro* cleavage assay, I was not able to detect any CED-3-mediated cleavage of ECT-2 or its PH domain (Result 3.1.5). From our *in vivo* localization studies, however, we found that CED-3 caspase activity is required for the dorsal clearance of ECT-2 (Result 3.2.2). It is possible that CED-3-mediated cleavage of proteins other than ECT-2 could be responsible for ECT-2's clearance from the dorsal cortex. Alternatively, possible explanations for not detecting any cleavage of ECT-2 *in vitro* could be due to our assays not being sensitive enough to detect small amounts of cleavage, or CED-3 requiring other factors and binding partners to effectively cleave ECT-2.

Similar to the enrichment of ECT-2 in the ventral cortex of the NSM neuroblast, it has been shown in single-celled *C. elegans* embryos that ECT-2 is enriched to the anterior cortex of the embryo, which forms the larger AB daughter cell (Motegi & Sugimoto, 2006). This enrichment of ECT-2 on the anterior side of the single-celled embryo is due



to the clearance of ECT-2 from the posterior cortex (Kapoor & Kotak, 2019). Furthermore, it has been proposed that the clearance of ECT-2 from the posterior cortex of single-celled embryos is mediated by a centrosome-associated protein called Aurora A kinase (AIR-1 in *C. elegans*) (Gan & Motegi, 2020; Kapoor & Kotak, 2019; Klinkert et al., 2019; Zhao et al., 2019). Interestingly, CED-3 has also been shown to interact with a centrosome protein called TAC-1 (Chakraborty et al., 2015). Depletion of AIR-1 led to uniform distribution of ECT-2 in the cortex of single-celled embryos (Kapoor & Kotak, 2019). It is possible that AIR-1 physically interacts with ECT-2 to de-recruit it from the posterior cortex, however, there is no direct evidence of such. Overall, the asymmetric localization of ECT-2 in single-celled embryos as well as in the NSM neuroblast occurs due to the de-recruitment of ECT-2 from one side of the cortex. In single-celled embryos, this de-recruitment might be mediated by centrosome AIR-1, whereas, in the NSM neuroblast, the de-recruitment might be mediated by CED-3.

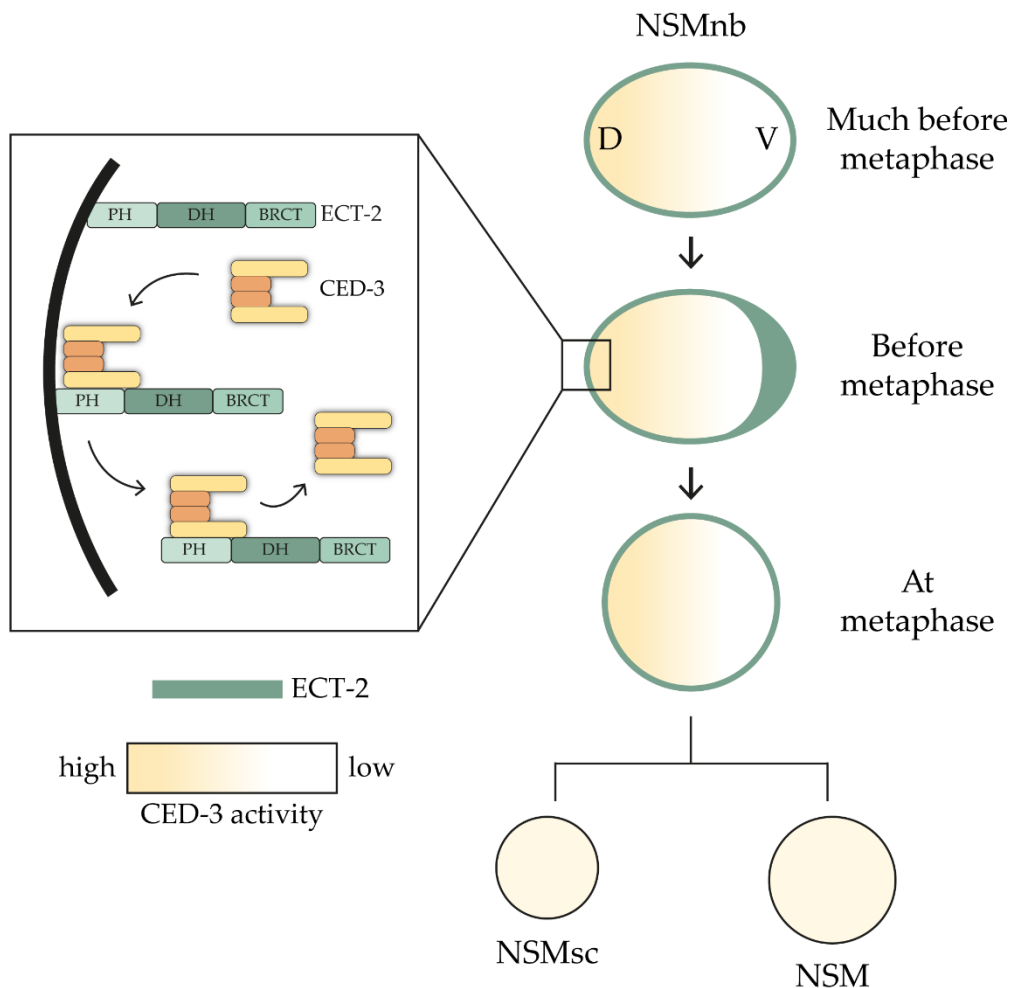


**Figure 4.2 CED-3 caspase mediates clearance of ECT-2 RhoGEF from the dorsal cortex of the NSMnb.** Much before metaphase, ECT-2 (green) is uniformly distributed in the cortex of the NSMnb. D is for dorsal and V is for ventral. Before metaphase, CED-3 binds to the PH domain of ECT-2 on the dorsal cortex, which de-recruits ECT-2 from the dorsal cortex and hence ECT-2 enriches in the ventral cortex. There is a dorsal to ventral gradient of CED-3 activity in the NSMnb (yellow). At metaphase, ECT-2 is again uniformly distributed in the cortex of the NSMnb. The NSMnb undergoes asymmetric division to form a smaller NSMsc and a larger NSM.

#### 4.1.2 The *ced-3-ect-2* axis acts in parallel with the *pig-1-nmy-2* axis to promote the formation of a smaller NSMsc below a lethal threshold

A previous study from our lab had shown that a *pig-1* MELK - *nmy-2* non-muscle myosin II axis promotes the asymmetric division of the NSM neuroblast, and thereby the formation of a smaller NSMsc (Wei et al., 2020). The study proposed that the *pig-1-nmy-2* axis promotes actomyosin contractility in the ventral side of the NSM

neuroblast, which was required for the NSM neuroblast to divide asymmetrically. The loss of ventral enrichment of NMY-2, using a *pig-1* loss-of-function mutation, led to the symmetric division of the NSM neuroblast and formation of equally sized daughter cells (NSMsc and NSM). Furthermore, *par-4*, *strd-1*, *mop25.1,2* and *ces-1* act upstream of *pig-1* and *nmy-2* in this context (Figure 4.3) (Wei et al., 2020). In our study, we provide evidence that another axis, called the *ced-3* caspase - *ect-2* RhoGEF axis, acts in parallel to the *pig-1-nmy-2* axis to promote asymmetric division of the NSM neuroblast, and thereby the formation of a smaller apoptotic NSMsc (Figure 4.3). We propose that *ced-3* acts upstream of *ect-2* to promote actomyosin contractility on the ventral side of the NSM neuroblast (Figure 4.3). In this context, we imagine that *ect-2* may act via promoting the activation of the RHO-1 (RhoA in mammals) signaling pathway, which consists of LET-502 (Rho-associated coiled-coil containing protein kinase (ROCK) in mammals) and myosin light chain MLC-4 (Myosin light chain 9 (MYL9) in mammals) (Figure 4.3). In higher organisms, Ect2 has been shown to promote F-actin polymerization and Myosin II activation (Figure 1.6) (Piekny et al., 2005). Our study provides evidence that the loss of *ced-3* caspase led to loss of ventral enrichment of ECT-2 in the NSM neuroblast, but did not affect the ventral enrichment of NMY-2 and F-actin (Result 3.2.2 and 3.2.3). Therefore, it is possible that the *ced-3-ect-2* axis in *C. elegans* might have targets other than NMY-2 and F-actin to promote asymmetric division of the NSM neuroblast. Alternatively, it could be possible that ECT-2 RhoGEF does not promote the ventral enrichment of NMY-2, but promotes its activity. This would mean that even though NMY-2 enriches on the ventral cortex of the NSM neuroblast in *ced-3* mutants, it might be less active than in wild-type animals. Finally, in this study, we also propose that the *ced-3-ect-2* axis plays a smaller role than the *pig-1-nmy-2* axis to promote the asymmetric division of the NSM neuroblast. In support of this proposal, we know that *ced-3* loss-of-function mutations alone do not have an effect on the asymmetric division of the NSM neuroblast. Only when we combine *ced-3* loss-of-function mutation with a temperature-sensitive partial loss-of-function mutation of *ect-2*, we see a significant effect on the asymmetric division of the

NSM neuroblast (Result 3.2.6). Even so, this effect is not as strong as in mutations of genes in the *pig-1-nmy-2* axis. Additionally, a previous study from our lab showed that in animals homozygous for the loss-of-function of both, *pig-1* and *ced-3*, led to a reversal of size asymmetry of the daughter cells, where the NSMsc is larger than the NSM (Mishra et al., 2018). We found that compromising both axes using a complete loss-of-function of *strd-1* (in the *pig-1-nmy-2* axis) and partial loss of *ect-2* (in the *ced-3-ect-2* axis) simultaneously also led to a reversal of size asymmetry of the daughter cells, where the NSMsc is larger than the NSM (Result 3.2.7). In summary, we propose that the *ced-3-ect-2* axis acts in parallel to the *pig-1-nmy-2* axis to promote the asymmetric division of the NSM neuroblast and thereby the formation of a smaller NSMsc. Furthermore, in this context, the *ced-3-ect-2* axis plays a smaller role than the *pig-1-nmy-2* axis.

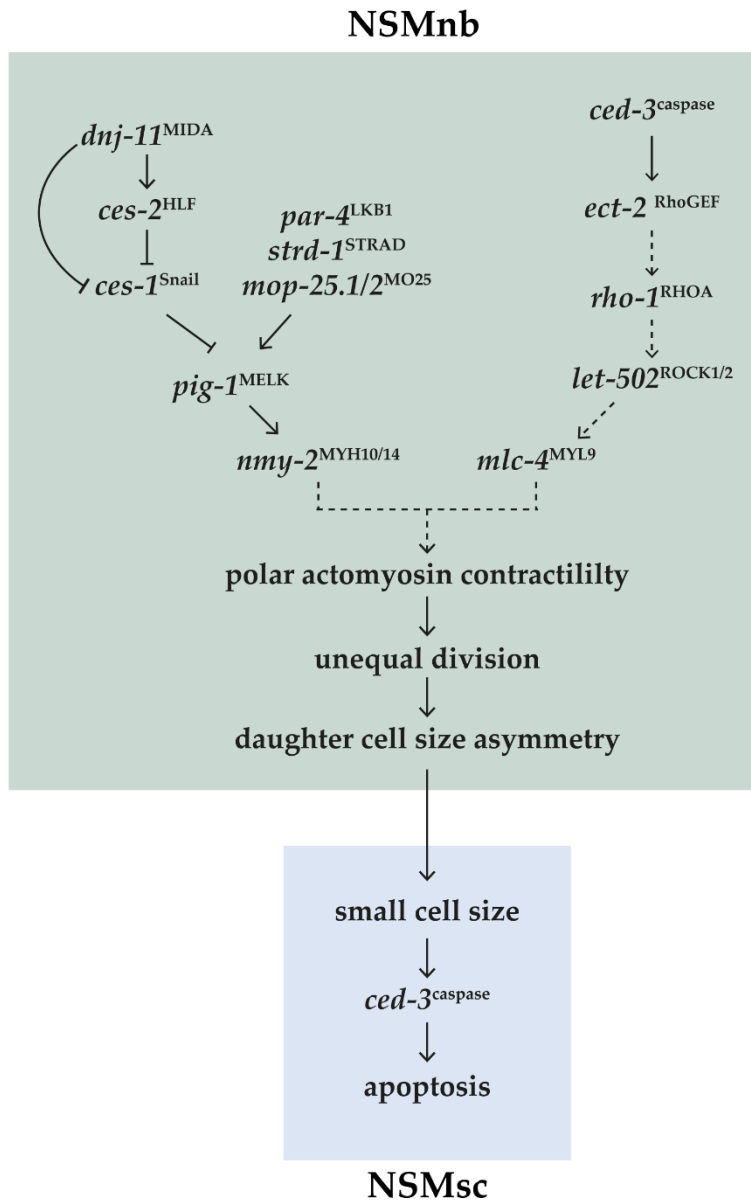


**Figure 4.3** The *ced-3-ect-2* axis acts in parallel to the *pig-1-nmy-2* axis to promote a smaller apoptotic NSMsc. In the NSMnb (green), two axes i.e. *pig-1-nmy-2* (left) and *ced-3-ect-2* (right), act in parallel to promote daughter cell size asymmetry. In the NSMsc (blue), a small cell size promotes apoptosis via *ced-3* activation/activity.

#### 4.1.3 The small size of the NSMsc promotes its apoptotic death via activation and/or activity of CED-3 caspase

In this study, we used various mutations that affect the asymmetric division of the NSM neuroblast, and thereby increase or decrease the relative size of the smaller apoptotic daughter cell, the NSMsc. We then tested the apoptotic fate of the NSMsc in these mutants. In wild-type animals, the NSMsc is approximately 0.66 times the size of the NSM and always undergoes apoptosis. We found that decreasing *ect-2* function by using a temperature-sensitive partial loss-of-function allele *ax751*, increases the relative size of the NSMsc (Figure 4.4), and in these animals, the NSMsc survives in 4% of the cases (Result 3.3.1). Furthermore, when we combine *ect-2(ax751)* mutation to partial loss-of-function mutations in *ced-3*, the survival of the NSMsc is enhanced (Result 3.3.1). We believe that this is due to the increase in the relative size of the NSMsc in these mutants. Previous studies in our lab have also used mutations in other genes, which affect the asymmetric division of the NSM neuroblast and lead to the formation of a relatively larger NSMsc. For instance, Wei *et al.*, 2020 used loss-of-function mutations of genes involved in actomyosin contractility, such as *pig-1* and *nmy-2*, which led the formation of larger NSMsc and thereby its inappropriate survival in 2.3% and 1.7% of cases, respectively (Wei *et al.*, 2020). Another study by Hatzold *et al.*, found that mutations in genes that control gene expression, such as *dnj-11* also led to formation of a larger NSMsc and thereby its inappropriate survival in 28% of cases (Hatzold & Conradt, 2008). Overall, there is evidence from various studies implying that a larger NSMsc has a higher probability to survive. Apart from increasing the relative size of the NSMsc, we were also able to decrease the relative size of the NSMsc by using gain-of-function mutations in *ect-2* that lead to its hyperactivation (Figure 4.4.) (Result 3.3.2). This is the first time, at least to the best of my knowledge, that anyone was able to decrease the relative size of the apoptotic daughter i.e the NSMsc. We found that by decreasing the size of the NSMsc, we were able to suppress the inappropriate survival of the NSMsc in animals harboring partial loss-of-function

mutations of *ced-3* (Result 3.3.2) (Figure 4.4). Again, this was the first time, at least to the best of my knowledge, where we could suppress the Ced (cell death) phenotype of *ced-3* partial loss-of-function mutant animals. We propose that the enhanced apoptotic ability of these mutants is due to the smaller size of the NSMsc. Taken together, there is an inverse correlation between cell size and apoptotic cell death – a larger cell size has lower probability of undergoing apoptosis and a smaller cell size promotes apoptotic probability.

What is the molecular mechanism that promotes apoptosis in smaller cells? To gain insight into that question, we investigated whether the enhanced ability of smaller cells to die is mediated by the apoptotic pathway. We found that decreasing the cell size via *ect-2* hyperactivation does not suppress cell survival in complete loss-of-function mutations of the pro-apoptotic genes – *ced-3*, *ced-4* and *egl-1* (Result 3.3.3). Therefore, smaller cells are more prone to die via apoptosis and not some other type of cell death. These results led us to propose that a smaller cell size has a higher concentration of pro-apoptotic proteins acting upstream of *ced-3*, such as EGL-1 and CED-4, which facilitates the activation of proCED-3 zymogen into active CED-3 caspase (Figure 4.3, bottom and Figure 4.4). We imagine that there is a critical lethal threshold of concentration of pro-apoptotic proteins that promote apoptosis – cells that have a size below this lethal threshold will have a high concentration of pro-apoptotic factors that will lead to its death. Conversely, cells that have a size above the lethal threshold will have a low concentration of pro-apoptotic factors resulting in their inappropriate survival.

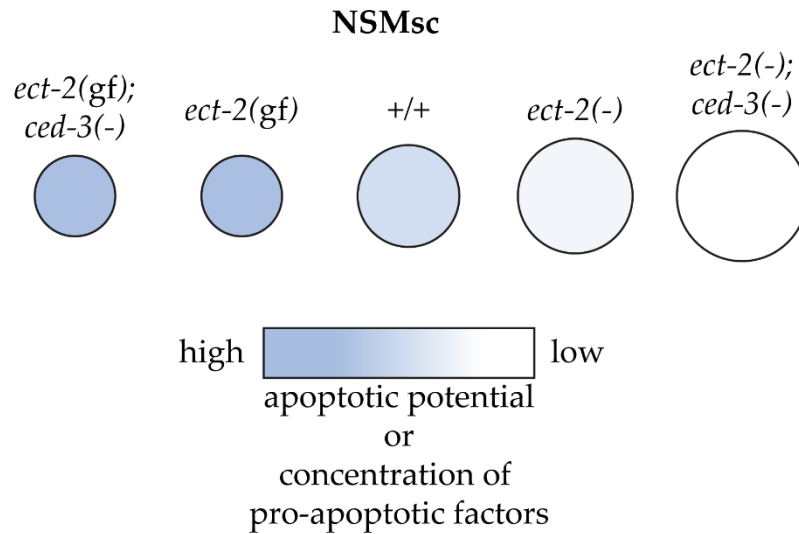


**Figure 4.4 Inverse correlation between cell size and apoptosis.** Smaller cells, as shown in *ect-2(gf)* and *ect-2(gf); ced-3(-)* have higher apoptotic potential (blue gradient). Larger cells, as shown in *ect-2(-)* and *ect-2(-); ced-3(-)* have lower apoptotic potential.

In single-celled *C. elegans* embryos, *ect-2* plays an important role in promoting asymmetric actomyosin contractility on the anterior side of the embryo, which generates cortical flows that are required for the polarization of the embryo (Motegi & Sugimoto, 2006; Schonegg & Hyman, 2006). Reducing *ect-2* function leads to the disruption of polarization dynamics of single-celled embryos (Zonies et al., 2010). In this study, we propose that reducing *ect-2* function leads to generation of a larger NSMsc, which has higher probability to survive because of its larger size. However, we cannot rule out the possibility that reducing *ect-2* function enhances the probability of the NSMsc to survive because of changes in cell polarity or processes other than cell size. Currently, we cannot imagine any experiments that could unlink cell polarity and cell size.



## 4.2 Actomyosin-associated substrates of caspases during apoptosis

---

In my study, we showed that CED-3 caspase physically interacts with ECT-2 RhoGEF, which is a regulator of the actomyosin network. In line with our findings, there have also been two studies in mammalian cells that have shown direct interactions between caspases and the actomyosin network in the context of apoptosis. The first study demonstrated that mammalian cells undergoing apoptosis show caspase-mediated cleavage of actin (Mashima et al., 1999). The cleaved actin acts downstream of the apoptotic pathway and induces cell shrinkage, which is characteristic of apoptotic cells. The second study showed that in apoptotic mammalian cells, caspase-3-mediated cleavage of ROCK I results in the removal of its inhibitory domain leading to ROCK I having constitutive kinase activity (Sebbagh et al., 2001). Constitutively active ROCK I can thereby lead to phosphorylation of myosin light chain and induce membrane blebbing in these apoptotic cells (Coleman et al., 2001; Sebbagh et al., 2001). Apart from mammalian cells, there was another study that aimed to identify substrates of *C. elegans* CED-3 caspase-mediated cleavage that could explain the apoptotic morphology of cells (Taylor et al., 2007). Although an *in vitro* approach was used, 22 *C. elegans* proteins were identified as targets of CED-3 caspase-mediated cleavage including actomyosin-associated proteins such as Actin (Act-1,2,3,4), Myosin light chain (MLC-2), Tubulin beta-2 chain (TBB-2) and Tubulin alpha (TBA-2) (Taylor et al., 2007). Overall, there is mounting evidence that the apoptotic pathway interacts with the actomyosin network in the context of apoptosis.

### 4.3 Non-apoptotic roles of caspases

---

While caspases are best known for their role in apoptosis, a plethora of studies in mammals, flies and worms have also established that caspases play a number of non-apoptotic roles in the cell (Galluzzi et al., 2012; Kuranaga & Miura, 2007; Nakajima & Kuranaga, 2017). In fact, caspases were originally known as cysteine proteases called ICE (interleukin-1 beta-converting enzymes), where their function was to cleave inflammatory cytokines during immune responses (Black et al., 1989; Kostura et al., 1989). ICE was subsequently renamed to Caspase-1 after the discovery of *ced-3* in *C. elegans* in 1993, where researchers found that *ced-3* encodes for an enzyme similar to mammalian ICE proteins (Yuan et al., 1993). Since the discovery of *ced-3* most studies focused on the role of caspases in the initiation and execution of apoptosis. However, in the last two decades, many non-apoptotic roles of caspases have been demonstrated such as cell differentiation, cell proliferation, control of cell cycle, cell migration and cytoskeletal dynamics. In our study, we have shed light on the mechanism of a novel non-apoptotic role of *ced-3* caspase in asymmetric cell division of neuroblasts. Similar to our findings, multiple studies in *C. elegans* have also identified other non-apoptotic roles of *ced-3* caspase, which will be described below.

#### 4.3.1 Non-apoptotic roles of the *C. elegans ced-3* caspase

In the last decade, there have been multiple studies that have identified various non-apoptotic roles of the *C. elegans ced-3* caspase. For example, *ced-3* was shown to act during early responses to neuronal injury to promote axon regeneration and reconnection (Pinan-Lucarre et al., 2012). The researchers proposed that *ced-3* acts via calcium signaling pathways to promote axon regeneration, although a substrate for CED-3-mediated cleavage was not identified for this function (Pinan-Lucarre et al., 2012). Another study found that pro-apoptotic factors, including *ced-3* are required for

mitochondria reactive oxygen species (mtROS)-mediated signaling in the pro-longevity response (Yee et al., 2014). Again, the researchers did not identify targets of CED-3-mediated cleavage required for this response. Furthermore, at least two more studies not only discovered non-apoptotic roles of *ced-3*, but also identified novel targets of CED-3-mediated cleavage to regulate those functions. The most recent study published in 2020 demonstrated that *ced-3* promotes larval development in the absence of stress by antagonizing the function of PMK-1 (p38 Map Kinase Family 1) (Weaver et al., 2020). Specifically, they found that CED-3 represses PMK-1 function by cleaving it at Asp327 residue and thereby promotes development (Weaver et al., 2020). Another study reported that CED-3 cooperates with a E3 ubiquitin ligase UBR-1 to effectively cleave and inactivate a pluripotency factor LIN-28 (Weaver et al., 2017). Inactivation of LIN-28 by CED-3 enables proper cell fate patterning of seam-cells during *C. elegans* development (Weaver et al., 2017; Weaver et al., 2014). In our study, we have identified another novel non-apoptotic role of *ced-3* caspase in promoting asymmetric cell division of the NSM neuroblast. Furthermore, we provide evidence that CED-3 physically interacts with ECT-2 RhoGEF in this context, however, whether CED-3 proteolytically cleaves ECT-2 remains unclear from our studies.

#### **4.3.2 Non-apoptotic role of caspases in regulation of the cytoskeletal dynamics**

In our study, we showed that *ced-3* caspase interacts with *ect-2* RhoGEF to promote asymmetric division of the neuroblasts, most likely by influencing actomyosin contractility. Thus, we shed light on the mechanism of a novel non-apoptotic function of *ced-3* caspase as a regulator of the actomyosin network and thereby the cytoskeleton. Similar to our finding, some studies have also shown caspases to interact with cytoskeletal components in non-apoptotic contexts. For example, it was shown that caspase-3-mediated cleavage and activation of ROCK I controls polarity and cell shape of mouse macrophages (Liu et al., 2016). Additionally, studies in *Drosophila* have shown that the initiator caspase Dronc influences F-actin polymerization and thereby the shape of cellular structures called arista (Oshima et al., 2006). There have also

been studies showing the involvement of caspases in regulating cell migration and cell motility suggesting that caspases can influence cytoskeletal dynamics (Helfer et al., 2006; Li et al., 2007; Torres et al., 2010). Furthermore, we also have preliminary evidence that the *ced-3* caspase -*ect-2* RhoGEF axis promotes mitotic rounding of the NSM neuroblast, a process that requires cytoskeleton reorganization (Result 3.4.1). This evidence further supports the notion that caspases are regulators of cytoskeletal dynamics in non-apoptotic contexts. Overall, there are several studies supporting our findings that caspases can influence the cytoskeletal actomyosin network in non-apoptotic contexts.

#### 4.4 A small cell size can trigger apoptosis

---

In our study we showed that a smaller NSMsc has higher probability to undergo apoptotic cell death. Similar to our findings, studies in animal culture cells have shown a similar phenomenon. For example, a study in Kc167 cultured cells, which is a *Drosophila* cell line, found that the smallest cells within the population showed the highest level of apoptotic death (Miettinen & Bjorklund, 2016). Another study in HeLa cells showed that in mutants where the cell divides asymmetrically, 15% of the smaller daughter cells undergo apoptotic death (Kiyomitsu & Cheeseman, 2013). The researchers in this study suggested that cells have a size threshold for survival. Furthermore, in order to investigate whether cell size reduction can trigger apoptosis, many studies in cell cultures have shown that when cells are subjected to shrinkage by incubating them in hypertonic solutions, the cells undergo apoptotic cell death (Lang & Hoffmann, 2012). Overall, the studies in *in vitro* cell cultures have demonstrated that a small cell size can trigger apoptosis. Additionally, there have also been *in vivo* studies that show that a small cell size can trigger apoptosis. For example, a study in *Drosophila* germ stem cells found that knock-down of a family of microtubule motors leads to the stem cells dividing asymmetrically by size. Subsequently, there was a significant increase in apoptosis of the smaller daughter cells (Chen et al., 2016). Another study in *C. elegans* germ line found that reducing germ cell size via thermoviscous pumping leads to their apoptotic death (Chartier et al., 2021). Furthermore, the *C. elegans* lineage is invariant, where exactly 131 somatic cells die during embryonic and post-embryonic development. Interestingly, most of the 131 dying cells are the smaller daughter cell of a blast cell that divides asymmetrically by size (Sulston & Horvitz, 1977; Sulston et al., 1983).

Apart from showing that a small cell size triggers apoptosis, there have been a few studies in *C. elegans*, which show that increasing the size of cells reduces their ability

to undergo apoptosis. For example, a study in 2006 investigated the effect of the loss of the gene *pig-1* (MELK) on the apoptotic fate of the smaller daughter cells of various asymmetric neuroblast divisions (Cordes et al., 2006). The researchers in this study found that the loss of *pig-1* results in the neuroblasts dividing symmetrically by size instead of asymmetrically and thereby forming a comparatively larger apoptotic daughter cell. They found that in many cases, the now larger 'apoptotic' daughter cells did not undergo apoptosis and survived to differentiate into a neuron (Cordes et al., 2006). Taken together, there is increasing evidence that smaller cells have higher probability to undergo apoptotic cell death, however, the molecular mechanisms remain largely unexplored.

## 4.5 Future directions of the project

---

### 4.5.1 Molecular mechanisms that promote the apoptotic death of small cells

In the above section, I described the various studies which show that a small cell size can trigger apoptosis. In our study, we also showed that reducing the size of the NSMsc increases its probability to undergo apoptosis. However, what are the molecular mechanisms that trigger apoptosis in smaller cells? We found that a smaller NSMsc will not undergo death if the apoptotic pathway has been completely compromised. These results suggest that smaller cells die via apoptosis rather than another type of cell death. Thus, we propose that a smaller cells have a higher concentration of pro-apoptotic proteins acting upstream of *ced-3*, such as EGL-1 and CED-4 (Figure 4.4), which facilitate the activation of proCED-3 zymogen into active CED-3 caspase. In order to gain further insight into the mechanism, I imagine that developing an *in vivo* real-time caspase activity sensor would be the most promising approach. Although caspase activity sensors have been developed in living cells and *Drosophila melanogaster*, a *C. elegans* specific caspase sensor has not yet been developed, at least to the best of my knowledge (Bardet et al., 2008; Cen et al., 2008; Chen et al., 2009; den Hamer et al., 2017; Tang et al., 2016; Wang et al., 2005; Zhang et al., 2013). Development of a caspase sensor in *C. elegans* would enable the investigation of the effect of cell size on the activation of CED-3 caspase. Using the various mutants mentioned in this study, we can increase or decrease the size of the apoptotic NSMsc and subsequently study the kinetics, localization and dynamics of CED-3 caspase activation using the caspase sensor. Additionally, in our study, we proposed that CED-3 forms an activity gradient in the NSM neuroblast i.e. the mother of the apoptotic NSMsc. To that end, a caspase sensor would enable us to analyze this caspase activity gradient and identify genes that can alter the gradient.

#### 4.5.2 RNAi screen to identify genes other than *ect-2*, which act with *ced-3* caspase to promote a smaller NSMsc size

In our study, we identified a *ced-3-ect-2* axis that promotes the asymmetric division of the NSM neuroblast and the formation of a smaller NSMsc. One of the future avenues of this project would be to identify genes other than *ect-2*, that act with *ced-3* to promote a smaller NSMsc size. We imagined that a genetic screen approach using RNA-mediated interference (RNAi) would be ideal to identify genes that act with *ced-3*. RNAi by feeding is quick and effective method to knockdown genes of interest in *C. elegans* (Timmons & Fire, 1998). Instead of performing a genome-wide RNAi screen, we decided that we could only screen for interactors of proCED-3 and proCED-3(C358S) protein that we had obtained from the Yeast two-hybrid screen (Result 3.1.1). Furthermore, we also decided to screen for genes that act in the Ras, Notch and Wnt signaling pathways as we know that signals arriving from neighboring cells are also important for setting up the CED-3 activity gradient in the NSM neuroblast (Chakraborty et al., 2015). To that end, I constructed an RNAi sub-library from the commercially available Ahringer feeding RNAi library (Kamath et al., 2003). The sub-library contained RNAi clones targeting 558 genes (Table 4). I also sequence verified all the RNAi clones in the sub-library and found that ~90% of the clones had the appropriate sequences. Additionally, I chose to use the partial loss-of-function mutation of *ced-3, n2427*, as the genetic background for the screen. I also chose NSMsc survival as the scorable phenotype for the screen because we have shown in our study that changes in asymmetric division and cell size can alter the apoptotic fate of the NSMsc. Finally, neurons have been known to be resistant to RNAi because of the lack of double-stranded RNA (dsRNA) transporter (Feinberg & Hunter, 2003; Winston et al., 2002). Thus, I decided to utilize a transgene that drives the expression of the dsRNA transporter *sid-1* pan-neuronally to enhance neuronal RNAi (Calixto et al., 2010).



**Table 4: Number of genes that will be used for the RNAi screen**

|  | Number of genes |
|--|-----------------|
| Interactors of proCED-3                | 186             |
| Interactors of proCED-3(C358S)         | 448             |
| Ras, Notch and Wnt signaling           | 111             |
| Total genes (with overlap)             | 657             |
| Genes out of total in Ahringer library | 558             |

The NSMsc survival of animals carrying *ced-3(n2427)* mutation is 18% (Result 3.3.1). We have shown that increasing the size of the NSMsc by reducing *ect-2* function causes a significant increase in the NSMsc survival of *ced-3(n2427)* animals from 18% to 25% (Result 3.3.1). Therefore, using this RNAi screen approach, we can possibly identify genes, which when knocked down would lead to an enhancement of the 18% NSMsc survival phenotype of *ced-3(n2427)* animals. Conversely, we have also shown that reducing the size of the NSMsc by hyperactivation of *ect-2* results in a significant decrease in the NSMsc survival of *ced-3(n2427)* animals from 18% to 9% (Result 3.3.2). Thus, we can also possibly identify genes, which when knocked down would lead to an suppression of the 18% NSMsc survival phenotype of *ced-3(n2427)* animals. Overall, it is possible to perform a genetic enhancer and suppressor screen using RNAi to identify genes that cooperate with *ced-3* to promote the smaller size of the NSMsc. Although during my thesis timeframe, I was able to construct the strains and RNAi sub-library, I could not manage to perform the screen.

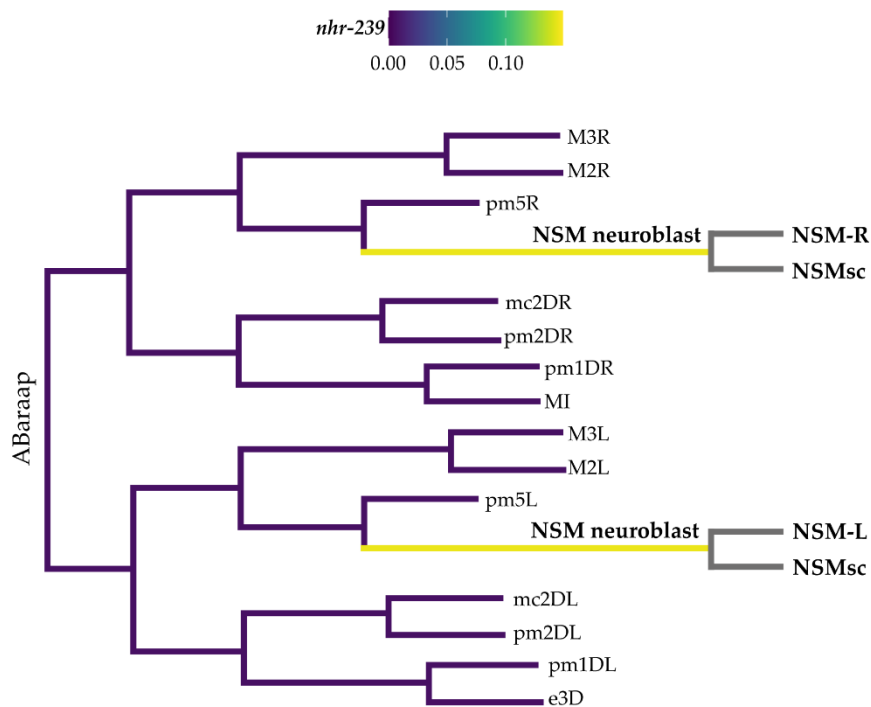
### 4.5.3 Establishing a NSM lineage specific reporter in developing embryos

To date, no reporter has been identified that can exclusively label the NSM lineage (NSM neuroblast, NSMsc and NSM) in *C. elegans* embryos and larvae. The only method to visualize the NSM neurons in larvae and adults is by using a serotonergic neuron reporter, *Ptph-1::his-24::gfp*, that labels all serotonergic neurons in worms, which includes the NSM (Yan et al., 2013). This reporter is not expressed in embryos and cannot be used to identify the NSM neuroblast. The only method to identify the NSM neuroblast and its daughters (NSM and NSMsc) in developing embryos is by using a plasma membrane reporter, *P<sub>pie-1m</sub>Cherry::PH<sup>PLCΔ</sup>* that labels the cell boundary of all cells (Figure 1.13). Using this reporter, the NSM neuroblast can be identified based on its shape and neighboring cells, however, the identification requires weeks' worth of practice. Therefore, one of our future aims was to develop a reporter that is expressed in the NSM neuroblast and its daughter cells, the NSMsc and NSM, in developing embryos. To that end, I utilized single-cell RNA sequencing (scRNAseq) data of *C. elegans* embryogenesis available publicly to identify a reporter that would be exclusively expressed in the NSM lineage (Packer et al., 2019). The scRNAseq dataset was generated by Packer *et al.*, 2019 by analyzing the transcriptome of ~80,000 cells dissociated from developing embryos, and thereby generating a RNA profile for each cell and assigning their identities post-hoc (Packer et al., 2019). I used the interactive online application tool of this dataset, called VisCello, ([https://cello.shinyapps.io/celegans\\_explorer/](https://cello.shinyapps.io/celegans_explorer/)) and identified a gene called *nhr-239* (nuclear hormone receptor family) that should be exclusively expressed in the NSM lineage (Figure 4.5, A).

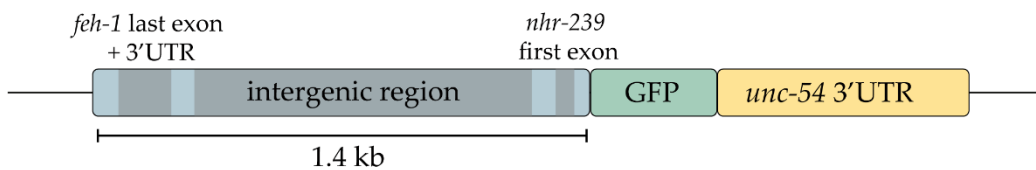
To generate a transcriptional reporter for this gene, I fused a 1.4 kb genomic region upstream of the *nhr-239* gene locus with GFP and *unc-54* 3' UTR (*P<sub>nhr-239</sub>::GFP*) (Figure 4.5, B). The upstream region also contains the last exon and 3' UTR of the upstream gene *feh-1* and the first exon of *nhr-239* (Figure 4.5, B). Subsequently, my colleague M. Ghani generated a single-copy insertion of this transcriptional reporter

using MosSCI (El Mouridi & Frokjaer-Jensen, 2022) and we analyzed GFP expression. Although we observed very bright GFP expression exclusively in the two NSM neurons in larvae and adults (Figure 4.5, C), we could not observe any fluorescence signal in the embryo stage when the NSM neuroblast is present (data not shown). The possible reasons for not seeing any fluorescence in embryos could be because the reporter is not expressed at such an early stage or because the expression is too low to be detected. If the latter, the issue could be solved by generating a multi-copy reporter using UV integration or other techniques available to make multi-copy insertions. Another reason for not seeing good levels of expression in the embryos could be that the construct lacks important cis-acting elements that might be located in the introns or downstream of the coding region of the *nhr-239* gene. Establishment of a reporter that is expressed exclusively in the NSM lineage would allow us to drive the expression of genes of interest in the NSM neuroblast and its daughter cells. It would enable analysis of protein localization in the NSM lineage in developing embryos without interfering signals from neighboring cells. Furthermore, strong expression of a reporter in the NSM lineage would enable FACS-based sorting and subsequent transcriptome profiling of the NSM neuroblast, NSMsc and NSM in dissociated embryos. This could give us novel insights into the gene expression profile of the NSM lineage. Lastly, a NSM lineage specific reporter would enable targeted depletion of gene products exclusively in the NSM lineage. For example, proteins that are tagged with ZF1 tags (zinc finger domain) can be degraded in the NSM lineage by expressing E3 ubiquitin ligase substrate-recognition subunit ZIF-1 using the NSM lineage reporter (Armenti et al., 2014). Thereby, ZIF-1 will only be present in the NSM lineage, which will bind to ZF1-tagged proteins and target them for degradation. Overall, a NSM lineage exclusive reporter will help advance our knowledge of the NSM lineage further.

A]



B]



C]



**Figure 4.5 *nhr-239* is a good candidate for a NSM lineage specific reporter.** A] Adapted from (Packer et al., 2019). Expression level of *nhr-239* from single-cell RNA sequencing data shows that *nhr-239* is exclusively expressed in the NSM neuroblasts. B] Schematic representation of the transcription reporter construct used for labelling the NSM lineage. C] Fluorescence and DIC images of animals expressing a single-copy of the transcriptional reporter *Pnhr-239::GFP*.

## 4.6 Concluding remarks

---

My study of the reciprocal interactions between the apoptotic pathway and cell size in *C. elegans* have led to two novel and important discoveries in cell biology. The first discovery is the mechanistic insight into how *ced-3* caspase promotes asymmetric cell division. Using *in vitro* assays and the NSM lineage, we uncovered a novel genetic pathway, called the *ced-3-ect-2* axis. We showed that this axis promotes asymmetric division of the NSM neuroblast and thereby the formation of a smaller apoptotic daughter cell (NSMsc), which is below the critical lethal threshold. Furthermore, we showed for the first time that CED-3 protein physically and directly interacts with ECT-2, which most likely promotes polar actomyosin contractility in the NSM neuroblast. Genes are mostly pleiotropic i.e. the same gene can have multiple functions. Although *ced-3* is most well-known for its role in executing apoptosis, in this study, we have gained insight into a non-canonical function of *ced-3* in promoting asymmetric cell division and a smaller daughter cell size.

The second discovery of this study was the effect of cell size on apoptotic fate of cells. We found that a smaller cells are more prone to die via apoptosis and larger cells are more prone to evade apoptosis. While studying the effect of cell size on apoptosis, we were able to, for the first time, reduce the size of apoptotic cells in *C. elegans* and suppress the cell death (Ced) phenotype. Apoptosis is a common cell fate during animal development and is subject to multiple levels of regulation (transcriptional, post-transcriptional, post-translational etc.) to ensure that only the appropriate cells undergo apoptosis. With this discovery, we have shed light on another regulator of apoptosis, which is cell size. We believe that a small cell size can trigger apoptosis by having a higher concentration of pro-apoptotic factors, which thereby leads to increased activation/activity of caspases. Further studies will be required to decipher the exact mechanism by which a small cell size can trigger apoptosis.

Research in *C. elegans* is critical to understanding the fundamentals of biology that can apply to all living organisms. For example, the discovery of the apoptotic pathway in *C. elegans* fuelled the discovery of a homologous mammalian apoptotic pathway that is evolutionarily conserved. Similarly, my study of the interactions between the apoptotic pathway and cell size could enhance our knowledge of fundamental phenomena in cell biology and development.

## References

---

- Agarwal, P., & Zaidel-Bar, R. (2019). Principles of Actomyosin Regulation In Vivo. *Trends Cell Biol*, 29(2), 150-163. <https://doi.org/10.1016/j.tcb.2018.09.006>
- Alberts, A. S. (2001). Identification of a carboxyl-terminal diaphanous-related formin homology protein autoregulatory domain. *J Biol Chem*, 276(4), 2824-2830. <https://doi.org/10.1074/jbc.M006205200>
- Allen, R. D., David, G. B., & Nomarski, G. (1969). The zeiss-Nomarski differential interference equipment for transmitted-light microscopy. *Z Wiss Mikrosk*, 69(4), 193-221. <https://www.ncbi.nlm.nih.gov/pubmed/5361069>
- Alnemri, E. S., Livingston, D. J., Nicholson, D. W., Salvesen, G., Thornberry, N. A., Wong, W. W., & Yuan, J. (1996). Human ICE/CED-3 protease nomenclature. *Cell*, 87(2), 171. [https://doi.org/10.1016/s0092-8674\(00\)81334-3](https://doi.org/10.1016/s0092-8674(00)81334-3)
- Armenti, S. T., Lohmer, L. L., Sherwood, D. R., & Nance, J. (2014). Repurposing an endogenous degradation system for rapid and targeted depletion of *C. elegans* proteins. *Development*, 141(23), 4640-4647. <https://doi.org/10.1242/dev.115048>
- Arnold, T. R., Stephenson, R. E., & Miller, A. L. (2017). Rho GTPases and actomyosin: Partners in regulating epithelial cell-cell junction structure and function. *Exp Cell Res*, 358(1), 20-30. <https://doi.org/10.1016/j.yexcr.2017.03.053>
- Audhya, A., Hyndman, F., McLeod, I. X., Maddox, A. S., Yates, J. R., 3rd, Desai, A., & Oegema, K. (2005). A complex containing the Sm protein CAR-1 and the RNA helicase CGH-1 is required for embryonic cytokinesis in *Caenorhabditis elegans*. *J Cell Biol*, 171(2), 267-279. <https://doi.org/10.1083/jcb.200506124>
- Axang, C., Rauthan, M., Hall, D. H., & Pilon, M. (2008). Developmental genetics of the *C. elegans* pharyngeal neurons NSML and NSMR. *BMC Dev Biol*, 8, 38. <https://doi.org/10.1186/1471-213X-8-38>
- Bakhshi, A., Jensen, J. P., Goldman, P., Wright, J. J., McBride, O. W., Epstein, A. L., & Korsmeyer, S. J. (1985). Cloning the chromosomal breakpoint of t(14;18) human lymphomas: clustering around JH on chromosome 14 and near a transcriptional unit on 18. *Cell*, 41(3), 899-906. [https://doi.org/10.1016/s0092-8674\(85\)80070-2](https://doi.org/10.1016/s0092-8674(85)80070-2)
- Bardet, P. L., Kolahgar, G., Mynett, A., Miguel-Aliaga, I., Briscoe, J., Meier, P., & Vincent, J. P. (2008). A fluorescent reporter of caspase activity for live imaging. *Proc Natl Acad Sci U S A*, 105(37), 13901-13905. <https://doi.org/10.1073/pnas.0806983105>
- Basant, A., & Glotzer, M. (2017). A GAP that Divides. *F1000Res*, 6, 1788. <https://doi.org/10.12688/f1000research.12064.1>
- Bertheloot, D., Latz, E., & Franklin, B. S. (2021). Necroptosis, pyroptosis and apoptosis: an intricate game of cell death. *Cell Mol Immunol*, 18(5), 1106-1121. <https://doi.org/10.1038/s41423-020-00630-3>

- Black, R. A., Kronheim, S. R., & Sleath, P. R. (1989). Activation of interleukin-1 beta by a co-induced protease. *FEBS Lett*, 247(2), 386-390. [https://doi.org/10.1016/0014-5793\(89\)81376-6](https://doi.org/10.1016/0014-5793(89)81376-6)
- Brenner, S. (1974). The genetics of *Caenorhabditis elegans*. *Genetics*, 77(1), 71-94. <https://doi.org/10.1093/genetics/77.1.71>
- Cabernard, C., Prehoda, K. E., & Doe, C. Q. (2010). A spindle-independent cleavage furrow positioning pathway. *Nature*, 467(7311), 91-94. <https://doi.org/10.1038/nature09334>
- Cadart, C., Zlotek-Zlotkiewicz, E., Le Berre, M., Piel, M., & Matthews, H. K. (2014). Exploring the function of cell shape and size during mitosis. *Dev Cell*, 29(2), 159-169. <https://doi.org/10.1016/j.devcel.2014.04.009>
- Calixto, A., Chelur, D., Topalidou, I., Chen, X., & Chalfie, M. (2010). Enhanced neuronal RNAi in *C. elegans* using SID-1. *Nat Methods*, 7(7), 554-559. <https://doi.org/10.1038/nmeth.1463>
- Canevascini, S., Marti, M., Frohli, E., & Hajnal, A. (2005). The *Caenorhabditis elegans* homologue of the proto-oncogene *ect-2* positively regulates RAS signalling during vulval development. *EMBO Rep*, 6(12), 1169-1175. <https://doi.org/10.1038/sj.embor.7400574>
- Cen, H., Mao, F., Aronchik, I., Fuentes, R. J., & Firestone, G. L. (2008). DEVD-NucView488: a novel class of enzyme substrates for real-time detection of caspase-3 activity in live cells. *FASEB J*, 22(7), 2243-2252. <https://doi.org/10.1096/fj.07-099234>
- Cerretti, D. P., Kozlosky, C. J., Mosley, B., Nelson, N., Van Ness, K., Greenstreet, T. A., March, C. J., Kronheim, S. R., Druck, T., Cannizzaro, L. A., & et al. (1992). Molecular cloning of the interleukin-1 beta converting enzyme. *Science*, 256(5053), 97-100. <https://doi.org/10.1126/science.1373520>
- Chakraborty, S., Lambie, E. J., Bindu, S., Mikeladze-Dvali, T., & Conradt, B. (2015). Engulfment pathways promote programmed cell death by enhancing the unequal segregation of apoptotic potential. *Nat Commun*, 6, 10126. <https://doi.org/10.1038/ncomms10126>
- Chan, E., & Nance, J. (2013). Mechanisms of CDC-42 activation during contact-induced cell polarization. *J Cell Sci*, 126(Pt 7), 1692-1702. <https://doi.org/10.1242/jcs.124594>
- Chartier, N. T., Mukherjee, A., Pfanzerter, J., Furthauer, S., Larson, B. T., Fritsch, A. W., Amini, R., Kreysing, M., Julicher, F., & Grill, S. W. (2021). A hydraulic instability drives the cell death decision in the nematode germline. *Nat Phys*, 17(8), 920-925. <https://doi.org/10.1038/s41567-021-01235-x>
- Chen, C., Inaba, M., Venkei, Z. G., & Yamashita, Y. M. (2016). Klp10A, a stem cell centrosome-enriched kinesin, balances asymmetries in *Drosophila* male germline stem cell division. *Elife*, 5. <https://doi.org/10.7554/eLife.20977>
- Chen, F., Hersh, B. M., Conradt, B., Zhou, Z., Riemer, D., Gruenbaum, Y., & Horvitz, H. R. (2000). Translocation of *C. elegans* CED-4 to nuclear membranes during



- programmed cell death. *Science*, 287(5457), 1485-1489. <https://doi.org/10.1126/science.287.5457.1485>
- Chen, M., Pan, H., Sun, L., Shi, P., Zhang, Y., Li, L., Huang, Y., Chen, J., Jiang, P., Fang, X., Wu, C., & Chen, Z. (2020). Structure and regulation of human epithelial cell transforming 2 protein. *Proc Natl Acad Sci U S A*, 117(2), 1027-1035. <https://doi.org/10.1073/pnas.1913054117>
- Chen, N., Huang, Y., Yang, L., Liu, R., & Yang, J. J. (2009). Designing caspase-3 sensors for imaging of apoptosis in living cells. *Chemistry*, 15(37), 9311-9314. <https://doi.org/10.1002/chem.200901439>
- Cherfils, J., & Zeghouf, M. (2013). Regulation of small GTPases by GEFs, GAPs, and GDIs. *Physiol Rev*, 93(1), 269-309. <https://doi.org/10.1152/physrev.00003.2012>
- Chesarone, M. A., & Goode, B. L. (2009). Actin nucleation and elongation factors: mechanisms and interplay. *Curr Opin Cell Biol*, 21(1), 28-37. <https://doi.org/10.1016/j.ceb.2008.12.001>
- Cleary, M. L., Smith, S. D., & Sklar, J. (1986). Cloning and structural analysis of cDNAs for bcl-2 and a hybrid bcl-2/immunoglobulin transcript resulting from the t(14;18) translocation. *Cell*, 47(1), 19-28. [https://doi.org/10.1016/0092-8674\(86\)90362-4](https://doi.org/10.1016/0092-8674(86)90362-4)
- Coleman, M. L., Sahai, E. A., Yeo, M., Bosch, M., Dewar, A., & Olson, M. F. (2001). Membrane blebbing during apoptosis results from caspase-mediated activation of ROCK I. *Nat Cell Biol*, 3(4), 339-345. <https://doi.org/10.1038/35070009>
- Connell, M., Cabernard, C., Ricketson, D., Doe, C. Q., & Prehoda, K. E. (2011). Asymmetric cortical extension shifts cleavage furrow position in *Drosophila* neuroblasts. *Mol Biol Cell*, 22(22), 4220-4226. <https://doi.org/10.1091/mbc.E11-02-0173>
- Conradt, B., & Horvitz, H. R. (1998). The *C. elegans* protein EGL-1 is required for programmed cell death and interacts with the Bcl-2-like protein CED-9. *Cell*, 93(4), 519-529. [https://doi.org/10.1016/s0092-8674\(00\)81182-4](https://doi.org/10.1016/s0092-8674(00)81182-4)
- Conradt, B., Wu, Y. C., & Xue, D. (2016). Programmed Cell Death During *Caenorhabditis elegans* Development. *Genetics*, 203(4), 1533-1562. <https://doi.org/10.1534/genetics.115.186247>
- Conradt, B., & Xue, D. (2005). Programmed cell death. *WormBook*, 1-13. <https://doi.org/10.1895/wormbook.1.32.1>
- Consortium, C. e. D. M. (2012). large-scale screening for targeted knockouts in the *Caenorhabditis elegans* genome. *G3 (Bethesda)*, 2(11), 1415-1425. <https://doi.org/10.1534/g3.112.003830>
- Cordes, S., Frank, C. A., & Garriga, G. (2006). The *C. elegans* MELK ortholog PIG-1 regulates cell size asymmetry and daughter cell fate in asymmetric neuroblast divisions. *Development*, 133(14), 2747-2756. <https://doi.org/10.1242/dev.02447>
- Cowan, C. R., & Hyman, A. A. (2004a). Asymmetric cell division in *C. elegans*: cortical polarity and spindle positioning. *Annu Rev Cell Dev Biol*, 20, 427-453. <https://doi.org/10.1146/annurev.cellbio.19.111301.113823>

- Cowan, C. R., & Hyman, A. A. (2004b). Centrosomes direct cell polarity independently of microtubule assembly in *C. elegans* embryos. *Nature*, 431(7004), 92-96. <https://doi.org/10.1038/nature02825>
- Cowan, C. R., & Hyman, A. A. (2007). Acto-myosin reorganization and PAR polarity in *C. elegans*. *Development*, 134(6), 1035-1043. <https://doi.org/10.1242/dev.000513>
- del Peso, L., Gonzalez, V. M., & Nunez, G. (1998). *Caenorhabditis elegans* EGL-1 disrupts the interaction of CED-9 with CED-4 and promotes CED-3 activation. *J Biol Chem*, 273(50), 33495-33500. <https://doi.org/10.1074/jbc.273.50.33495>
- DeLong, M. J. (1998). Apoptosis: a modulator of cellular homeostasis and disease states. *Ann N Y Acad Sci*, 842, 82-90. <https://doi.org/10.1111/j.1749-6632.1998.tb09635.x>
- den Hamer, A., Dierickx, P., Arts, R., de Vries, J., Brunsveld, L., & Merckx, M. (2017). Bright Bioluminescent BRET Sensor Proteins for Measuring Intracellular Caspase Activity. *ACS Sens*, 2(6), 729-734. <https://doi.org/10.1021/acssensors.7b00239>
- Doe, C. Q. (2008). Neural stem cells: balancing self-renewal with differentiation. *Development*, 135(9), 1575-1587. <https://doi.org/10.1242/dev.014977>
- El Mouridi, S., & Frokjaer-Jensen, C. (2022). Targeted and Random Transposon-Assisted Single-Copy Transgene Insertion in *C. elegans*. *Methods Mol Biol*, 2468, 239-256. [https://doi.org/10.1007/978-1-0716-2181-3\\_12](https://doi.org/10.1007/978-1-0716-2181-3_12)
- Ellis, H. M., & Horvitz, H. R. (1986). Genetic control of programmed cell death in the nematode *C. elegans*. *Cell*, 44(6), 817-829. [https://doi.org/10.1016/0092-8674\(86\)90004-8](https://doi.org/10.1016/0092-8674(86)90004-8)
- Ellis, R. E., & Horvitz, H. R. (1991). Two *C. elegans* genes control the programmed deaths of specific cells in the pharynx. *Development*, 112(2), 591-603. <https://doi.org/10.1242/dev.112.2.591>
- Elmore, S. (2007). Apoptosis: a review of programmed cell death. *Toxicol Pathol*, 35(4), 495-516. <https://doi.org/10.1080/01926230701320337>
- Feinberg, E. H., & Hunter, C. P. (2003). Transport of dsRNA into cells by the transmembrane protein SID-1. *Science*, 301(5639), 1545-1547. <https://doi.org/10.1126/science.1087117>
- Fickentscher, R., & Weiss, M. (2017). Physical determinants of asymmetric cell divisions in the early development of *Caenorhabditis elegans*. *Sci Rep*, 7(1), 9369. <https://doi.org/10.1038/s41598-017-09690-4>
- Fletcher, D. A., & Mullins, R. D. (2010). Cell mechanics and the cytoskeleton. *Nature*, 463(7280), 485-492. <https://doi.org/10.1038/nature08908>
- Fuchs, Y., & Steller, H. (2011). Programmed cell death in animal development and disease. *Cell*, 147(4), 742-758. <https://doi.org/10.1016/j.cell.2011.10.033>
- Fuchs, Y., & Steller, H. (2015). Live to die another way: modes of programmed cell death and the signals emanating from dying cells. *Nat Rev Mol Cell Biol*, 16(6), 329-344. <https://doi.org/10.1038/nrm3999>

- Galli, M., & van den Heuvel, S. (2008). Determination of the cleavage plane in early *C. elegans* embryos. *Annu Rev Genet*, 42, 389-411. <https://doi.org/10.1146/annurev.genet.40.110405.090523>
- Galluzzi, L., Kepp, O., Trojel-Hansen, C., & Kroemer, G. (2012). Non-apoptotic functions of apoptosis-regulatory proteins. *EMBO Rep*, 13(4), 322-330. <https://doi.org/10.1038/embor.2012.19>
- Galvin, B. D., Denning, D. P., & Horvitz, H. R. (2011). SPK-1, an SR protein kinase, inhibits programmed cell death in *Caenorhabditis elegans*. *Proc Natl Acad Sci U S A*, 108(5), 1998-2003. <https://doi.org/10.1073/pnas.1018805108>
- Gan, W. J., & Motegi, F. (2020). Mechanochemical Control of Symmetry Breaking in the *Caenorhabditis elegans* Zygote. *Front Cell Dev Biol*, 8, 619869. <https://doi.org/10.3389/fcell.2020.619869>
- Ganguly, R., Mohyeldin, A., Thiel, J., Kornblum, H. I., Beullens, M., & Nakano, I. (2015). MELK-a conserved kinase: functions, signaling, cancer, and controversy. *Clin Transl Med*, 4, 11. <https://doi.org/10.1186/s40169-014-0045-y>
- Gibson, D. G., Young, L., Chuang, R. Y., Venter, J. C., Hutchison, C. A., 3rd, & Smith, H. O. (2009). Enzymatic assembly of DNA molecules up to several hundred kilobases. *Nat Methods*, 6(5), 343-345. <https://doi.org/10.1038/nmeth.1318>
- Glotzer, M. (2005). The molecular requirements for cytokinesis. *Science*, 307(5716), 1735-1739. <https://doi.org/10.1126/science.1096896>
- Goldstein, B., & Macara, I. G. (2007). The PAR proteins: fundamental players in animal cell polarization. *Dev Cell*, 13(5), 609-622. <https://doi.org/10.1016/j.devcel.2007.10.007>
- Hatzold, J., & Conradt, B. (2008). Control of apoptosis by asymmetric cell division. *PLoS Biol*, 6(4), e84. <https://doi.org/10.1371/journal.pbio.0060084>
- Hedgecock, E. M., Sulston, J. E., & Thomson, J. N. (1983). Mutations affecting programmed cell deaths in the nematode *Caenorhabditis elegans*. *Science*, 220(4603), 1277-1279. <https://doi.org/10.1126/science.6857247>
- Helfer, B., Boswell, B. C., Finlay, D., Cipres, A., Vuori, K., Bong Kang, T., Wallach, D., Dorfleutner, A., Lahti, J. M., Flynn, D. C., & Frisch, S. M. (2006). Caspase-8 promotes cell motility and calpain activity under nonapoptotic conditions. *Cancer Res*, 66(8), 4273-4278. <https://doi.org/10.1158/0008-5472.CAN-05-4183>
- Hengartner, M. O., Ellis, R. E., & Horvitz, H. R. (1992). *Caenorhabditis elegans* gene *ced-9* protects cells from programmed cell death. *Nature*, 356(6369), 494-499. <https://doi.org/10.1038/356494a0>
- Hird, S. N., & White, J. G. (1993). Cortical and cytoplasmic flow polarity in early embryonic cells of *Caenorhabditis elegans*. *J Cell Biol*, 121(6), 1343-1355. <https://doi.org/10.1083/jcb.121.6.1343>
- Holdorf, A. D., Higgins, D. P., Hart, A. C., Boag, P. R., Pazour, G. J., Walhout, A. J. M., & Walker, A. K. (2020). WormCat: An Online Tool for Annotation and Visualization of *Caenorhabditis elegans* Genome-Scale Data. *Genetics*, 214(2), 279-294. <https://doi.org/10.1534/genetics.119.302919>

- Huang, W., Jiang, T., Choi, W., Qi, S., Pang, Y., Hu, Q., Xu, Y., Gong, X., Jeffrey, P. D., Wang, J., & Shi, Y. (2013). Mechanistic insights into CED-4-mediated activation of CED-3. *Genes Dev*, 27(18), 2039-2048. <https://doi.org/10.1101/gad.224428.113>
- Huxley, A. F. (2000). Mechanics and models of the myosin motor. *Philos Trans R Soc Lond B Biol Sci*, 355(1396), 433-440. <https://doi.org/10.1098/rstb.2000.0584>
- Jaeken, L. (2007). A new list of functions of the cytoskeleton. *IUBMB Life*, 59(3), 127-133. <https://doi.org/10.1080/15216540701320593>
- Kamath, R. S., Fraser, A. G., Dong, Y., Poulin, G., Durbin, R., Gotta, M., Kanapin, A., Le Bot, N., Moreno, S., Sohrmann, M., Welchman, D. P., Zipperlen, P., & Ahringer, J. (2003). Systematic functional analysis of the *Caenorhabditis elegans* genome using RNAi. *Nature*, 421(6920), 231-237. <https://doi.org/10.1038/nature01278>
- Kane, R. E. (1983). Interconversion of structural and contractile actin gels by insertion of myosin during assembly. *J Cell Biol*, 97(6), 1745-1752. <https://doi.org/10.1083/jcb.97.6.1745>
- Kapoor, S., & Kotak, S. (2019). Centrosome Aurora A regulates RhoGEF ECT-2 localisation and ensures a single PAR-2 polarity axis in *C. elegans* embryos. *Development*, 146(22). <https://doi.org/10.1242/dev.174565>
- Kelkar, M., Bohec, P., & Charras, G. (2020). Mechanics of the cellular actin cortex: From signalling to shape change. *Curr Opin Cell Biol*, 66, 69-78. <https://doi.org/10.1016/j.ceb.2020.05.008>
- Kerr, J. F., Wyllie, A. H., & Currie, A. R. (1972). Apoptosis: a basic biological phenomenon with wide-ranging implications in tissue kinetics. *Br J Cancer*, 26(4), 239-257. <https://doi.org/10.1038/bjc.1972.33>
- Kiyomitsu, T., & Cheeseman, I. M. (2013). Cortical dynein and asymmetric membrane elongation coordinately position the spindle in anaphase. *Cell*, 154(2), 391-402. <https://doi.org/10.1016/j.cell.2013.06.010>
- Klinkert, K., Levernier, N., Gross, P., Gentili, C., von Tobel, L., Pierron, M., Busso, C., Herrman, S., Grill, S. W., Kruse, K., & Gonczy, P. (2019). Aurora A depletion reveals centrosome-independent polarization mechanism in *Caenorhabditis elegans*. *Elife*, 8. <https://doi.org/10.7554/eLife.44552>
- Kostura, M. J., Tocci, M. J., Limjoco, G., Chin, J., Cameron, P., Hillman, A. G., Chartrain, N. A., & Schmidt, J. A. (1989). Identification of a monocyte specific pre-interleukin 1 beta convertase activity. *Proc Natl Acad Sci U S A*, 86(14), 5227-5231. <https://doi.org/10.1073/pnas.86.14.5227>
- Kreis, T. E., & Birchmeier, W. (1980). Stress fiber sarcomeres of fibroblasts are contractile. *Cell*, 22(2 Pt 2), 555-561. [https://doi.org/10.1016/0092-8674\(80\)90365-7](https://doi.org/10.1016/0092-8674(80)90365-7)
- Kuranaga, E., & Miura, M. (2007). Nonapoptotic functions of caspases: caspases as regulatory molecules for immunity and cell-fate determination. *Trends Cell Biol*, 17(3), 135-144. <https://doi.org/10.1016/j.tcb.2007.01.001>
- Lang, F., & Hoffmann, E. K. (2012). Role of ion transport in control of apoptotic cell death. *Compr Physiol*, 2(3), 2037-2061. <https://doi.org/10.1002/cphy.c110046>

- Li, J., Briehner, W. M., Scimone, M. L., Kang, S. J., Zhu, H., Yin, H., von Andrian, U. H., Mitchison, T., & Yuan, J. (2007). Caspase-11 regulates cell migration by promoting Aip1-Cofilin-mediated actin depolymerization. *Nat Cell Biol*, 9(3), 276-286. <https://doi.org/10.1038/ncb1541>
- Liu, Y., Minze, L. J., Mumma, L., Li, X. C., Ghobrial, R. M., & Kloc, M. (2016). Mouse macrophage polarity and ROCK1 activity depend on RhoA and non-apoptotic Caspase 3. *Exp Cell Res*, 341(2), 225-236. <https://doi.org/10.1016/j.yexcr.2016.02.004>
- Liu, Z., & Zhang, Z. (2022). Mapping cell types across human tissues. *Science*, 376(6594), 695-696. <https://doi.org/10.1126/science.abq2116>
- Mashima, T., Naito, M., & Tsuruo, T. (1999). Caspase-mediated cleavage of cytoskeletal actin plays a positive role in the process of morphological apoptosis. *Oncogene*, 18(15), 2423-2430. <https://doi.org/10.1038/sj.onc.1202558>
- Matsumura, F. (2005). Regulation of myosin II during cytokinesis in higher eukaryotes. *Trends Cell Biol*, 15(7), 371-377. <https://doi.org/10.1016/j.tcb.2005.05.004>
- Matthews, H. K., Delabre, U., Rohn, J. L., Guck, J., Kunda, P., & Baum, B. (2012). Changes in Ect2 localization couple actomyosin-dependent cell shape changes to mitotic progression. *Dev Cell*, 23(2), 371-383. <https://doi.org/10.1016/j.devcel.2012.06.003>
- McMillan, S. N., & Scarff, C. A. (2022). Cryo-electron microscopy analysis of myosin at work and at rest. *Curr Opin Struct Biol*, 75, 102391. <https://doi.org/10.1016/j.sbi.2022.102391>
- McNally, F. J. (2013). Mechanisms of spindle positioning. *J Cell Biol*, 200(2), 131-140. <https://doi.org/10.1083/jcb.201210007>
- Metzstein, M. M., Hengartner, M. O., Tsung, N., Ellis, R. E., & Horvitz, H. R. (1996). Transcriptional regulator of programmed cell death encoded by *Caenorhabditis elegans* gene *ces-2*. *Nature*, 382(6591), 545-547. <https://doi.org/10.1038/382545a0>
- Metzstein, M. M., & Horvitz, H. R. (1999). The *C. elegans* cell death specification gene *ces-1* encodes a snail family zinc finger protein. *Mol Cell*, 4(3), 309-319. [https://doi.org/10.1016/s1097-2765\(00\)80333-0](https://doi.org/10.1016/s1097-2765(00)80333-0)
- Miettinen, T. P., & Bjorklund, M. (2016). Cellular Allometry of Mitochondrial Functionality Establishes the Optimal Cell Size. *Dev Cell*, 39(3), 370-382. <https://doi.org/10.1016/j.devcel.2016.09.004>
- Mishra, N., Wei, H., & Conradt, B. (2018). *Caenorhabditis elegans* *ced-3* Caspase Is Required for Asymmetric Divisions That Generate Cells Programmed To Die. *Genetics*, 210(3), 983-998. <https://doi.org/10.1534/genetics.118.301500>
- Mosaddeghzadeh, N., & Ahmadian, M. R. (2021). The RHO Family GTPases: Mechanisms of Regulation and Signaling. *Cells*, 10(7). <https://doi.org/10.3390/cells10071831>

- Motegi, F., & Sugimoto, A. (2006). Sequential functioning of the ECT-2 RhoGEF, RHO-1 and CDC-42 establishes cell polarity in *Caenorhabditis elegans* embryos. *Nat Cell Biol*, 8(9), 978-985. <https://doi.org/10.1038/ncb1459>
- Munro, E., & Bowerman, B. (2009). Cellular symmetry breaking during *Caenorhabditis elegans* development. *Cold Spring Harb Perspect Biol*, 1(4), a003400. <https://doi.org/10.1101/cshperspect.a003400>
- Munro, E., Nance, J., & Priess, J. R. (2004). Cortical flows powered by asymmetrical contraction transport PAR proteins to establish and maintain anterior-posterior polarity in the early *C. elegans* embryo. *Dev Cell*, 7(3), 413-424. <https://doi.org/10.1016/j.devcel.2004.08.001>
- Nakajima, Y. I., & Kuranaga, E. (2017). Caspase-dependent non-apoptotic processes in development. *Cell Death Differ*, 24(8), 1422-1430. <https://doi.org/10.1038/cdd.2017.36>
- Nicholson, D. W. (1999). Caspase structure, proteolytic substrates, and function during apoptotic cell death. *Cell Death Differ*, 6(11), 1028-1042. <https://doi.org/10.1038/sj.cdd.4400598>
- Niederman, R., & Pollard, T. D. (1975). Human platelet myosin. II. In vitro assembly and structure of myosin filaments. *J Cell Biol*, 67(1), 72-92. <https://doi.org/10.1083/jcb.67.1.72>
- Oshima, K., Takeda, M., Kuranaga, E., Ueda, R., Aigaki, T., Miura, M., & Hayashi, S. (2006). IKK epsilon regulates F actin assembly and interacts with *Drosophila* IAP1 in cellular morphogenesis. *Curr Biol*, 16(15), 1531-1537. <https://doi.org/10.1016/j.cub.2006.06.032>
- Ou, G., Stuurman, N., D'Ambrosio, M., & Vale, R. D. (2010). Polarized myosin produces unequal-size daughters during asymmetric cell division. *Science*, 330(6004), 677-680. <https://doi.org/10.1126/science.1196112>
- Packer, J. S., Zhu, Q., Huynh, C., Sivaramakrishnan, P., Preston, E., Dueck, H., Stefanik, D., Tan, K., Trapnell, C., Kim, J., Waterston, R. H., & Murray, J. I. (2019). A lineage-resolved molecular atlas of *C. elegans* embryogenesis at single-cell resolution. *Science*, 365(6459). <https://doi.org/10.1126/science.aax1971>
- Parrish, J., Metters, H., Chen, L., & Xue, D. (2000). Demonstration of the in vivo interaction of key cell death regulators by structure-based design of second-site suppressors. *Proc Natl Acad Sci U S A*, 97(22), 11916-11921. <https://doi.org/10.1073/pnas.210391597>
- Pham, T. T., Monnard, A., Helenius, J., Lund, E., Lee, N., Muller, D. J., & Cabernard, C. (2019). Spatiotemporally Controlled Myosin Relocalization and Internal Pressure Generate Sibling Cell Size Asymmetry. *iScience*, 13, 9-19. <https://doi.org/10.1016/j.isci.2019.02.002>
- Piekny, A., Werner, M., & Glotzer, M. (2005). Cytokinesis: welcome to the Rho zone. *Trends Cell Biol*, 15(12), 651-658. <https://doi.org/10.1016/j.tcb.2005.10.006>
- Pinan-Lucarre, B., Gabel, C. V., Reina, C. P., Hulme, S. E., Shevkoplyas, S. S., Slone, R. D., Xue, J., Qiao, Y., Weisberg, S., Roodhouse, K., Sun, L., Whitesides, G. M.,

- Samuel, A., & Driscoll, M. (2012). The core apoptotic executioner proteins CED-3 and CED-4 promote initiation of neuronal regeneration in *Caenorhabditis elegans*. *PLoS Biol*, 10(5), e1001331. <https://doi.org/10.1371/journal.pbio.1001331>
- Pollard, T. D. (2007). Regulation of actin filament assembly by Arp2/3 complex and formins. *Annu Rev Biophys Biomol Struct*, 36, 451-477. <https://doi.org/10.1146/annurev.biophys.35.040405.101936>
- Pollard, T. D., & Korn, E. D. (1973). Electron microscopic identification of actin associated with isolated amoeba plasma membranes. *J Biol Chem*, 248(2), 448-450. <https://www.ncbi.nlm.nih.gov/pubmed/4567783>
- Qi, S., Pang, Y., Hu, Q., Liu, Q., Li, H., Zhou, Y., He, T., Liang, Q., Liu, Y., Yuan, X., Luo, G., Li, H., Wang, J., Yan, N., & Shi, Y. (2010). Crystal structure of the *Caenorhabditis elegans* apoptosome reveals an octameric assembly of CED-4. *Cell*, 141(3), 446-457. <https://doi.org/10.1016/j.cell.2010.03.017>
- Reddien, P. W., Cameron, S., & Horvitz, H. R. (2001). Phagocytosis promotes programmed cell death in *C. elegans*. *Nature*, 412(6843), 198-202. <https://doi.org/10.1038/35084096>
- Redemann, S., Pcreaux, J., Goehring, N. W., Khairy, K., Stelzer, E. H., Hyman, A. A., & Howard, J. (2010). Membrane invaginations reveal cortical sites that pull on mitotic spindles in one-cell *C. elegans* embryos. *PLoS One*, 5(8), e12301. <https://doi.org/10.1371/journal.pone.0012301>
- Riddle, D. L., Blumenthal, T., Meyer, B. J., & Priess, J. R. (1997). In *C. elegans II* (2nd ed.). Cold Spring Harbor (NY).
- Roberston, A. M. G., & Thomson, J. N. (1982). Morphology of programmed cell death in the ventral nerve cord of *Caenorhabditis elegans* larvae. *Development*, 67(1), 89-100. <https://doi.org/https://doi.org/10.1242/dev.67.1.89>
- Rolland, S. G., Lu, Y., David, C. N., & Conradt, B. (2009). The BCL-2-like protein CED-9 of *C. elegans* promotes FZO-1/Mfn1,2- and EAT-3/Opa1-dependent mitochondrial fusion. *J Cell Biol*, 186(4), 525-540. <https://doi.org/10.1083/jcb.200905070>
- Rose, L., & Gonczy, P. (2014). Polarity establishment, asymmetric division and segregation of fate determinants in early *C. elegans* embryos. *WormBook*, 1-43. <https://doi.org/10.1895/wormbook.1.30.2>
- Rose, L. S., Lamb, M. L., Hird, S. N., & Kemphues, K. J. (1995). Pseudocleavage is dispensable for polarity and development in *C. elegans* embryos. *Dev Biol*, 168(2), 479-489. <https://doi.org/10.1006/dbio.1995.1096>
- Schneid, S., Wolff, F., Buchner, K., Bertram, N., Baygun, S., Barbosa, P., Mangal, S., & Zanin, E. (2021). The BRCT domains of ECT2 have distinct functions during cytokinesis. *Cell Rep*, 34(9), 108805. <https://doi.org/10.1016/j.celrep.2021.108805>
- Schonegg, S., & Hyman, A. A. (2006). CDC-42 and RHO-1 coordinate acto-myosin contractility and PAR protein localization during polarity establishment in *C. elegans* embryos. *Development*, 133(18), 3507-3516. <https://doi.org/10.1242/dev.02527>

- Sebbagh, M., Renvoize, C., Hamelin, J., Riche, N., Bertoglio, J., & Breard, J. (2001). Caspase-3-mediated cleavage of ROCK I induces MLC phosphorylation and apoptotic membrane blebbing. *Nat Cell Biol*, 3(4), 346-352. <https://doi.org/10.1038/35070019>
- Seshagiri, S., & Miller, L. K. (1997). Caenorhabditis elegans CED-4 stimulates CED-3 processing and CED-3-induced apoptosis. *Curr Biol*, 7(7), 455-460. [https://doi.org/10.1016/s0960-9822\(06\)00216-8](https://doi.org/10.1016/s0960-9822(06)00216-8)
- Shaham, S., & Horvitz, H. R. (1996). Developing Caenorhabditis elegans neurons may contain both cell-death protective and killer activities. *Genes Dev*, 10(5), 578-591. <https://doi.org/10.1101/gad.10.5.578>
- Shaham, S., Reddien, P. W., Davies, B., & Horvitz, H. R. (1999). Mutational analysis of the Caenorhabditis elegans cell-death gene ced-3. *Genetics*, 153(4), 1655-1671. <https://doi.org/10.1093/genetics/153.4.1655>
- Sherrard, R., Luehr, S., Holzkamp, H., McJunkin, K., Memar, N., & Conradt, B. (2017). miRNAs cooperate in apoptosis regulation during C. elegans development. *Genes Dev*, 31(2), 209-222. <https://doi.org/10.1101/gad.288555.116>
- Srinivasula, S. M., Ahmad, M., Fernandes-Alnemri, T., & Alnemri, E. S. (1998). Autoactivation of procaspase-9 by Apaf-1-mediated oligomerization. *Mol Cell*, 1(7), 949-957. [https://doi.org/10.1016/s1097-2765\(00\)80095-7](https://doi.org/10.1016/s1097-2765(00)80095-7)
- Stossel, T. P. (1984). Contribution of actin to the structure of the cytoplasmic matrix. *J Cell Biol*, 99(1 Pt 2), 15s-21s. <https://doi.org/10.1083/jcb.99.1.15s>
- Sulston, J. E., & Horvitz, H. R. (1977). Post-embryonic cell lineages of the nematode, Caenorhabditis elegans. *Dev Biol*, 56(1), 110-156. [https://doi.org/10.1016/0012-1606\(77\)90158-0](https://doi.org/10.1016/0012-1606(77)90158-0)
- Sulston, J. E., Schierenberg, E., White, J. G., & Thomson, J. N. (1983). The embryonic cell lineage of the nematode Caenorhabditis elegans. *Dev Biol*, 100(1), 64-119. [https://doi.org/10.1016/0012-1606\(83\)90201-4](https://doi.org/10.1016/0012-1606(83)90201-4)
- Sunchu, B., & Cabernard, C. (2020). Principles and mechanisms of asymmetric cell division. *Development*, 147(13). <https://doi.org/10.1242/dev.167650>
- Tang, H. L., Tang, H. M., Fung, M. C., & Hardwick, J. M. (2016). In Vivo Biosensor Tracks Non-apoptotic Caspase Activity in Drosophila. *J Vis Exp*(117). <https://doi.org/10.3791/53992>
- Taubenberger, A. V., Baum, B., & Matthews, H. K. (2020). The Mechanics of Mitotic Cell Rounding. *Front Cell Dev Biol*, 8, 687. <https://doi.org/10.3389/fcell.2020.00687>
- Taylor, R. C., Brumatti, G., Ito, S., Hengartner, M. O., Derry, W. B., & Martin, S. J. (2007). Establishing a blueprint for CED-3-dependent killing through identification of multiple substrates for this protease. *J Biol Chem*, 282(20), 15011-15021. <https://doi.org/10.1074/jbc.M611051200>
- Taylor, R. C., Cullen, S. P., & Martin, S. J. (2008). Apoptosis: controlled demolition at the cellular level. *Nat Rev Mol Cell Biol*, 9(3), 231-241. <https://doi.org/10.1038/nrm2312>



- Theilmann, M., Hatzold, J., & Conradt, B. (2003). The Snail-like CES-1 protein of *C. elegans* can block the expression of the BH3-only cell-death activator gene *egl-1* by antagonizing the function of bHLH proteins. *Development*, 130(17), 4057-4071. <https://doi.org/10.1242/dev.00597>
- Thornberry, N. A., Bull, H. G., Calaycay, J. R., Chapman, K. T., Howard, A. D., Kostura, M. J., Miller, D. K., Molineaux, S. M., Weidner, J. R., Aunins, J., & et al. (1992). A novel heterodimeric cysteine protease is required for interleukin-1 beta processing in monocytes. *Nature*, 356(6372), 768-774. <https://doi.org/10.1038/356768a0>
- Timmons, L., & Fire, A. (1998). Specific interference by ingested dsRNA. *Nature*, 395(6705), 854. <https://doi.org/10.1038/27579>
- Torres, V. A., Mielgo, A., Barbero, S., Hsiao, R., Wilkins, J. A., & Stupack, D. G. (2010). Rab5 mediates caspase-8-promoted cell motility and metastasis. *Mol Biol Cell*, 21(2), 369-376. <https://doi.org/10.1091/mbc.e09-09-0769>
- Trent, C., Tsuing, N., & Horvitz, H. R. (1983). Egg-laying defective mutants of the nematode *Caenorhabditis elegans*. *Genetics*, 104(4), 619-647. <https://doi.org/10.1093/genetics/104.4.619>
- Tsankova, A., Pham, T. T., Garcia, D. S., Otte, F., & Cabernard, C. (2017). Cell Polarity Regulates Biased Myosin Activity and Dynamics during Asymmetric Cell Division via *Drosophila* Rho Kinase and Protein Kinase N. *Dev Cell*, 42(2), 143-155 e145. <https://doi.org/10.1016/j.devcel.2017.06.012>
- Tse, Y. C., Werner, M., Longhini, K. M., Labbe, J. C., Goldstein, B., & Glotzer, M. (2012). RhoA activation during polarization and cytokinesis of the early *Caenorhabditis elegans* embryo is differentially dependent on NOP-1 and CYK-4. *Mol Biol Cell*, 23(20), 4020-4031. <https://doi.org/10.1091/mbc.E12-04-0268>
- Tsujimoto, Y., & Croce, C. M. (1986). Analysis of the structure, transcripts, and protein products of *bcl-2*, the gene involved in human follicular lymphoma. *Proc Natl Acad Sci U S A*, 83(14), 5214-5218. <https://doi.org/10.1073/pnas.83.14.5214>
- Vale, R. D., & Milligan, R. A. (2000). The way things move: looking under the hood of molecular motor proteins. *Science*, 288(5463), 88-95. <https://doi.org/10.1126/science.288.5463.88>
- Wang, D. S., & Shaw, G. (1995). The association of the C-terminal region of beta I sigma II spectrin to brain membranes is mediated by a PH domain, does not require membrane proteins, and coincides with a inositol-1,4,5 triphosphate binding site. *Biochem Biophys Res Commun*, 217(2), 608-615. <https://doi.org/10.1006/bbrc.1995.2818>
- Wang, Z. Q., Liao, J., & Diwu, Z. (2005). N-DEVD-N'-morpholinecarbonyl-rhodamine 110: novel caspase-3 fluorogenic substrates for cell-based apoptosis assay. *Bioorg Med Chem Lett*, 15(9), 2335-2338. <https://doi.org/10.1016/j.bmcl.2005.02.081>
- Weaver, B. P., Weaver, Y. M., Mitani, S., & Han, M. (2017). Coupled Caspase and N-End Rule Ligase Activities Allow Recognition and Degradation of Pluripotency

- Factor LIN-28 during Non-Apoptotic Development. *Dev Cell*, 41(6), 665-673 e666. <https://doi.org/10.1016/j.devcel.2017.05.013>
- Weaver, B. P., Weaver, Y. M., Omi, S., Yuan, W., Ewbank, J. J., & Han, M. (2020). Non-Canonical Caspase Activity Antagonizes p38 MAPK Stress-Priming Function to Support Development. *Dev Cell*, 53(3), 358-369 e356. <https://doi.org/10.1016/j.devcel.2020.03.015>
- Weaver, B. P., Zabinsky, R., Weaver, Y. M., Lee, E. S., Xue, D., & Han, M. (2014). CED-3 caspase acts with miRNAs to regulate non-apoptotic gene expression dynamics for robust development in *C. elegans*. *Elife*, 3, e04265. <https://doi.org/10.7554/eLife.04265>
- Wei, H., Lambie, E. J., Osorio, D. S., Carvalho, A. X., & Conradt, B. (2020). PIG-1 MELK-dependent phosphorylation of nonmuscle myosin II promotes apoptosis through CES-1 Snail partitioning. *PLoS Genet*, 16(9), e1008912. <https://doi.org/10.1371/journal.pgen.1008912>
- Wei, H., Yan, B., Gagneur, J., & Conradt, B. (2017). Caenorhabditis elegans CES-1 Snail Represses pig-1 MELK Expression To Control Asymmetric Cell Division. *Genetics*, 206(4), 2069-2084. <https://doi.org/10.1534/genetics.117.202754>
- Wernike, D., Chen, Y., Mastronardi, K., Makil, N., & Piekny, A. (2016). Mechanical forces drive neuroblast morphogenesis and are required for epidermal closure. *Dev Biol*, 412(2), 261-277. <https://doi.org/10.1016/j.ydbio.2016.02.023>
- Winston, W. M., Molodowitch, C., & Hunter, C. P. (2002). Systemic RNAi in *C. elegans* requires the putative transmembrane protein SID-1. *Science*, 295(5564), 2456-2459. <https://doi.org/10.1126/science.1068836>
- Xue, D., Shaham, S., & Horvitz, H. R. (1996). The Caenorhabditis elegans cell-death protein CED-3 is a cysteine protease with substrate specificities similar to those of the human CPP32 protease. *Genes Dev*, 10(9), 1073-1083. <https://doi.org/10.1101/gad.10.9.1073>
- Yan, B., Memar, N., Gallinger, J., & Conradt, B. (2013). Coordination of cell proliferation and cell fate determination by CES-1 snail. *PLoS Genet*, 9(10), e1003884. <https://doi.org/10.1371/journal.pgen.1003884>
- Yan, N., Chai, J., Lee, E. S., Gu, L., Liu, Q., He, J., Wu, J. W., Kokel, D., Li, H., Hao, Q., Xue, D., & Shi, Y. (2005). Structure of the CED-4-CED-9 complex provides insights into programmed cell death in Caenorhabditis elegans. *Nature*, 437(7060), 831-837. <https://doi.org/10.1038/nature04002>
- Yan, N., Gu, L., Kokel, D., Chai, J., Li, W., Han, A., Chen, L., Xue, D., & Shi, Y. (2004). Structural, biochemical, and functional analyses of CED-9 recognition by the proapoptotic proteins EGL-1 and CED-4. *Mol Cell*, 15(6), 999-1006. <https://doi.org/10.1016/j.molcel.2004.08.022>
- Yang, S., Tiwari, P., Lee, K. H., Sato, O., Ikebe, M., Padron, R., & Craig, R. (2020). Cryo-EM structure of the inhibited (10S) form of myosin II. *Nature*, 588(7838), 521-525. <https://doi.org/10.1038/s41586-020-3007-0>

- Yang, X., Chang, H. Y., & Baltimore, D. (1998). Autoproteolytic activation of procaspases by oligomerization. *Mol Cell*, 1(2), 319-325. [https://doi.org/10.1016/s1097-2765\(00\)80032-5](https://doi.org/10.1016/s1097-2765(00)80032-5)
- Yee, C., Yang, W., & Hekimi, S. (2014). The intrinsic apoptosis pathway mediates the pro-longevity response to mitochondrial ROS in *C. elegans*. *Cell*, 157(4), 897-909. <https://doi.org/10.1016/j.cell.2014.02.055>
- Yuan, J., & Horvitz, H. R. (1992). The *Caenorhabditis elegans* cell death gene *ced-4* encodes a novel protein and is expressed during the period of extensive programmed cell death. *Development*, 116(2), 309-320. <https://doi.org/10.1242/dev.116.2.309>
- Yuan, J., Shaham, S., Ledoux, S., Ellis, H. M., & Horvitz, H. R. (1993). The *C. elegans* cell death gene *ced-3* encodes a protein similar to mammalian interleukin-1 beta-converting enzyme. *Cell*, 75(4), 641-652. [https://doi.org/10.1016/0092-8674\(93\)90485-9](https://doi.org/10.1016/0092-8674(93)90485-9)
- Zaidel-Bar, R., Zhenhuan, G., & Luxenburg, C. (2015). The contractome--a systems view of actomyosin contractility in non-muscle cells. *J Cell Sci*, 128(12), 2209-2217. <https://doi.org/10.1242/jcs.170068>
- Zhang, D., & Glotzer, M. (2015). The RhoGAP activity of CYK-4/MgcRacGAP functions non-canonically by promoting RhoA activation during cytokinesis. *Elife*, 4. <https://doi.org/10.7554/eLife.08898>
- Zhang, J., Wang, X., Cui, W., Wang, W., Zhang, H., Liu, L., Zhang, Z., Li, Z., Ying, G., Zhang, N., & Li, B. (2013). Visualization of caspase-3-like activity in cells using a genetically encoded fluorescent biosensor activated by protein cleavage. *Nat Commun*, 4, 2157. <https://doi.org/10.1038/ncomms3157>
- Zhao, P., Teng, X., Tantirimudalige, S. N., Nishikawa, M., Wohland, T., Toyama, Y., & Motegi, F. (2019). Aurora-A Breaks Symmetry in Contractile Actomyosin Networks Independently of Its Role in Centrosome Maturation. *Dev Cell*, 48(5), 631-645 e636. <https://doi.org/10.1016/j.devcel.2019.02.012>
- Zonies, S., Motegi, F., Hao, Y., & Seydoux, G. (2010). Symmetry breaking and polarization of the *C. elegans* zygote by the polarity protein PAR-2. *Development*, 137(10), 1669-1677. <https://doi.org/10.1242/dev.045823>
- Zou, H., Henzel, W. J., Liu, X., Lutschg, A., & Wang, X. (1997). Apaf-1, a human protein homologous to *C. elegans* CED-4, participates in cytochrome c-dependent activation of caspase-3. *Cell*, 90(3), 405-413. [https://doi.org/10.1016/s0092-8674\(00\)80501-2](https://doi.org/10.1016/s0092-8674(00)80501-2)
- Zou, H., Li, Y., Liu, X., & Wang, X. (1999). An APAF-1-cytochrome c multimeric complex is a functional apoptosome that activates procaspase-9. *J Biol Chem*, 274(17), 11549-11556. <https://doi.org/10.1074/jbc.274.17.11549>

## Acknowledgements

---

I would like to start by thanking Barbara for supervising and mentoring me during my PhD. She has always motivated me to become a better scientist and researcher. I have learnt so much during my PhD, both intellectually and emotionally. We faced two big challenges together – A move from Germany to the UK and the COVID pandemic. She was extremely helpful during our move from Munich to London and guided us along the way. She was also our biggest pillar of support during the pandemic. I remember Barbara insisting that our lab should meet via video call every day during the first few months of the lockdown to check up on us and make sure we were doing ok. I also want to thank Eric Lambie, who has always been there whenever I needed advice or support with my experiments.

Secondly, I want to thank the IMPRS-LS coordination team – Hans-Joerg, Maxi, Ingrid, Marta and Sabine. They are the most organised and supportive team that I could have asked for. Thank you for making my PhD life so much easier. I also want to thank my Thesis Advisory Committee members – Alex Hajnal and Wolfgang Enard – whose advice during our annual meetings have been very valuable for the successful completion of my thesis.

I would like to thank all the members of the Conradt lab, both in Munich and in London for providing me with a great lab environment and always keeping me entertained – Laura, Elisabeth, Simon, Nikhil, Jimei, Yanwen, Ioannis, Fabian, Nadin, Hai, Madiha, Jens and Louisa. I also want to thank my friends in Munich, who made my life in Munich so much fun – Laura, Elisabeth, Simon, Sandra, Fritzi, Lisa, Jennifer and Marion. I also want to thank Padma, Arushi and Elena who have been the most amazing and supportive friends since I started my PhD.

To my closest friends and colleagues in UCL – Evie, Matthew, Susana, Laura and Carla - you all are family to me and you have been a big part of why I have decided to stay

in London for the long-term. I also want to thank my partner, Mati, whose constant love, support and patience cannot be expressed in words.

To my family – Mom, Dad, Neha and Sid – thank you for putting up with me. It would not have been possible to be the person I am today without you.

## Curriculum Vitae

---

**Aditya Rajiv Sethi**

[adityasethi.28@gmail.com](mailto:adityasethi.28@gmail.com)

University College London

Cell and Developmental Biology, Division of Biosciences

Gower Street, London

United Kingdom

### Education

1. PhD in Biology (2018-present)  
*Ludwig-Maximilians University, Munich, Germany*  
*International Max Planck Research School for Molecular Life Sciences, Germany*
2. Masters (M.Sc.) in Medical Biotechnology (2015-2017)  
*School of Life Sciences, Manipal University, Manipal, India*  
*ERASMUS Mundus – BioHealth Computing*
3. Bachelors (B. Sc) in Life Science-Biochemistry (2012-2015)  
*St. Xavier's College (Autonomous), Mumbai, India*

### Work Experience

1. Temporary Assistant Lecturer (2017-2018)  
*St. Xavier's College (Autonomous), Mumbai, India*
  - Taught Cell Biology to first-year Masters students, Environmental Science & Biochemistry to third-year Bachelor students
  - 20 hours of student contact per week & guided students in minor research projects
  - Assisted in editing syllabi, career guidance and setting and scoring examination questions.

### Certifications and training

1. Systems Training in Maths, Informatics, Statistics and Computational Biology (SysMIC) (2020-2021)  
*University College London, United Kingdom*
  - 120 hours of learning, programming using MATLAB, data analysis using R, mathematics for modelling, network theory and working with Petri nets
  - Completed mini-project (20 hours) involving modelling and networks in MATLAB

2. Computational Medicine (2017)  
*European Scientific Institute, France*
  - 80 hours of learning: multidisciplinary approach to understanding biological & pathological processes in chronic illness, using COPD as a case study
3. Innovation and Big Data for Health (2017)  
*European Scientific Institute, France*
  - 80 hours of learning: insight into challenges of using Big Data for optimizing healthcare, with obesity as a case study.

### **Scholarships**

1. IDEX Scholarship (2016-2017)  
*University Grenoble-Alpes*
2. INSPIRE Scholarship (2012-2015)  
*Government of India, Ministry of Science and Technology*

### **Conferences and meetings**

1. 23<sup>rd</sup> International C. elegans Conference (2021)  
*Genetics Society of America*
2. European Worm Meeting (2020)  
*European Worm Meeting*
3. The Allied Genetics Conference (2020)  
*Genetics Society of America*
4. Sequence Spotlight on Campus (2018)  
*Ludwig-Maximilians University, Munich*
5. 5<sup>th</sup> Annual Conference of the Society of Mitochondrial Research and Medicine on Mitochondria in Cancer and Neurodegenerative Disorders (2015)  
*Aravind Medical Research Foundation, India*

### **Workshops**

Data Analysis with R, Adobe Illustrator, Scientific Writing, Statistical Literacy, Scientific Image Processing and Analysis, Time Management in Doctoral Research  
*International Max Planck Research School for Molecular Life Sciences, Germany*

## List of publications

---

1. Sethi A, Wei H, Mishra N, Segos I, Lambie EJ, Zanin E, Conradt B (2022). A caspase-RhoGEF axis contributes to the cell size threshold for apoptotic death in developing *Caenorhabditis elegans*. *PLoS Biology*
2. Memar N, Sethi A, Luehr S, Lambie EJ, Conradt B (2022). In vivo labeling of endogenous genomic loci in *C. elegans* using CRISPR/dCas9. *microPublication Biology*